Nonlinear Transport in Two-Dimensional Electron Gas at Large Filling Factors

A DISSERTATION
SUBMITTED TO THE FACULTY OF THE GRADUATE SCHOOL
OF THE UNIVERSITY OF MINNESOTA
BY

Hung-Sheng Chiang

IN PARTIAL FULFILLMENT OF THE REQUIREMENTS
FOR THE DEGREE OF
Doctor Of Philosophy

April, 2011

Acknowledgements

I want to express my deepest gratitudes to those who have helped me throughout the years. Without them, this journey would be far more difficult. First and foremost, I would like to thank my research adviser, Prof. Zudov, for his academic guidance and financial support. Special thanks go to Prof. Crowell for his undeniable influence on me—both in physics knowledge and in the philosophy of doing scientific research. Dr. Pfeiffer and Dr. West (both of them are now with Princeton University) provided high-quality 2DEG samples which were crucial to our experiments. Without them, our discoveries would not have been possible. Dr. Khodas (Brookhaven National Laboratory) and Dr. Vavilov (University of Wisconsin) provided theoretical input to our research. Without them, a coherent understanding to our experimental findings could not have been achieved. I appreciate the friendships from Dr. Adams (Harvard University), Dr. Lou (Seagate Technology), and Dr. Zhang. Their psychological and technical supports were very important to me. Finally, I want to thank Anthony Hatke, a fellow graduate student who has helped me in countless circumstances.

Dedication

To my family.

ABSTRACT

We studied nonlinear electrical transport in high-mobility 2D electron gas (2DEG) forming in modulation-doped GaAs/AlGaAs quantum wells. Transport nonlinearities induced by a pure dc electric field as well as by coexisting dc and microwave fields were studied at very high Landau level filling factors. It was observed that a pure dc electric field could induce transport nonlinearities phenomenologically similar to those previously discovered in microwave-irradiated 2DEG. New phenomena in magnetotransport emerged when a 2DEG was under the simultaneous influences of a dc electric field and a microwave field. The experimental observations were compared to the numerical simulations which were carried out based on a recently proposed theory. Generally speaking, good agreement between the experimental data and the numerical results was obtained. This suggested that the rich transport nonlinearities we have observed so far could all be coherently understood within this theoretical work.

Contents

List of Tables

List of Figures

Chapter 1

Introduction

1.1 Classical diffusive transport

In this section, we will briefly review the classical theories of diffusive transport in the presence of an in-plane electric field $\vec{E}$ and an out-of-plane magnetic field $\vec{B}$ based on the treatment in Ref. [1]. The goal is to derive the longitudinal and transverse components of the conductivity/resistivity tensor. The mathematical equations will be a little dense, but each step should follow naturally and logically from the previous step.

1.1.1 Drude approach

Let us start out by writing down the classical equation of motion for an electron under the influence of Lorentz force:

$$m^*\dot{\vec{v}} = -e(\vec{E} + \vec{v} \times \vec{B}). \tag{1.1}$$

Assuming that $\vec{E} \perp \vec{B}$, a coordinate system can be set up such that $\vec{E} = E\hat{i}$ and $\vec{B} = B\hat{k}$. Electron scatterings in the presence of impurity can be taken into account by incorporating a phenomenological term in Eq. (1.1) to describe momentum-relaxation processes:

$$m^*\dot{\vec{v}} + \frac{m^*\vec{v}}{\tau} = -e(\vec{E} + \vec{v} \times \vec{B}). \tag{1.2}$$

τ is the phenomenological momentum-relaxation time. According to Ohm's law,

$$\vec{j} = \sigma \cdot \vec{E} \tag{1.3}$$

where σ is the conductivity tensor. Using the basic relation $\vec{j} = -en_{\mathrm{e}}\vec{v}$ (where n_{e} is the electron density), one can relate $\vec{E}$ to $\vec{v}$:

$$\vec{v} = -\frac{\sigma}{en_{\mathrm{e}}} \cdot \vec{E}. \tag{1.4}$$

We look for the steady-state solution to Eq. (1.2) in the form of Eq. (1.4). In matrix representation, Eq. (1.2) takes the following form (in 3D) in the steady state:

$$\frac{m^*}{\tau} \begin{pmatrix} v_x \\ v_y \\ v_z \end{pmatrix} + e \begin{pmatrix} E \\ 0 \\ 0 \end{pmatrix} + e \begin{pmatrix} Bv_y \\ -Bv_x \\ 0 \end{pmatrix} = 0, \tag{1.5}$$

or equivalently,

$$\begin{pmatrix} \frac{m^*}{\tau} & eB & 0 \\ -eB & \frac{m^*}{\tau} & 0 \\ 0 & 0 & \frac{m^*}{\tau} \end{pmatrix} \begin{pmatrix} v_x \\ v_y \\ v_z \end{pmatrix} = -e \begin{pmatrix} E \\ 0 \\ 0 \end{pmatrix}. \tag{1.6}$$

Eq. (1.6) is in the form of $A \cdot \vec{v} = -e\vec{E}$ with

$$A \equiv \begin{pmatrix} \frac{m^*}{\tau} & eB & 0 \\ -eB & \frac{m^*}{\tau} & 0 \\ 0 & 0 & \frac{m^*}{\tau} \end{pmatrix}.$$

By comparing such form with Eq. (1.4), one immediately sees the relation between the conductivity tensor σ and the matrix A:

$$\sigma = e^2 n_{\mathrm{e}} A^{-1}. \tag{1.7}$$

Using the formula $A^{-1} = [\mathrm{cof}(A)]^T/|A|$ (where $\mathrm{cof}(A)$ is the cofactor matrix of A), one obtains σ in its matrix form:

$$\sigma = \frac{\sigma_0}{1 + (\omega_{\mathrm{c}}\tau)^2} \begin{pmatrix} 1 & -\omega_{\mathrm{c}}\tau & 0 \\ \omega_{\mathrm{c}}\tau & 1 & 0 \\ 0 & 0 & 1 + (\omega_{\mathrm{c}}\tau)^2 \end{pmatrix} \tag{1.8}$$

where $\sigma_0 = e^2 n_{\mathrm{e}}\tau/m^*$ and $\omega_{\mathrm{c}} = eB/m^*$ (the cyclotron frequency). Since the resistivity tensor ρ is the inverse of the conductivity tensor σ, one can easily derive that

$$\rho = \frac{1}{e^2 n_{\mathrm{e}}} A \tag{1.9}$$

and

$$\rho = \begin{pmatrix} \frac{1}{\sigma_0} & \frac{B}{en_e} & 0 \\ -\frac{B}{en_e} & \frac{1}{\sigma_0} & 0 \\ 0 & 0 & \frac{1}{\sigma_0} \end{pmatrix}. \tag{1.10}$$

The corresponding 2D results (2×2-matrices) can be obtained by crossing out the third row and the third column in Eq. (1.8) and in Eq. (1.10).

From Eq. (1.8), one first notices that $\sigma_{zz} = \sigma_0$. This is expected because the force associated with $\vec{B} = B\hat{k}$ is perpendicular to the z-direction. Second, one notices that the classical Hall effect manifests naturally in σ_{xy} and σ_{yx}. The signs of σ_{xy} and σ_{yx} also correctly account for the polarity of the Hall voltage (or the direction of the Hall electric field). With $\vec{B} = B\hat{k}$, the Hall electric field is directed towards $+x\,(-y)$-direction if the current is passed in the $+y\,(+x)$-direction. Third, one notices an apparent relation between σ_{xx} and σ_{yx}:

$$\begin{array}{c} \sigma_{xx} + \omega_c \tau \sigma_{yx} = \sigma_0 \\ \Rightarrow \sigma_{yx} = en_e/B - \sigma_{xx}/\omega_c\tau \end{array}. \tag{1.11}$$

Supposing that we can adjust electron density such that $n_e = ieB/h$ (here i being a positive integer) for a given magnetic field B, this will make the filling factor $\nu \equiv n_e h/eB = i$, *i.e.*, exactly i Landau levels are filled (Landau levels will be introduced in Section 1.2). In such scenario, $\sigma_{xx} \to 0$ as $T \to 0$ because the Fermi level lies within a band of localized (insulating) states. In the mean time, momentum-relaxation time τ grows with decreasing temperature. As a result, $\sigma_{xy} \to ie^2/h$ as one continuously lowers the temperature. One can also populate exactly i Landau levels by adjusting the magnetic field such that $B = n_e h/ie$ at a given electron density n_e.

1.1.2 Boltzmann approach

In order to describe the average behavior of electrons, a function $f(\vec{k}, \vec{r}, t)$ (so-called "distribution function") was introduced. $(2\pi^2)^{-1} f(\vec{k}, \vec{r}, t)$ has the meaning of electron density in the $(\vec{k}, \vec{r})$-space (assuming two spatial dimensions). For simplicity, let us assume that only the electronic states in the ground subband are occupied and the dispersion relation is parabolic ($\varepsilon = \hbar^2 \vec{k}^2/2m^*$). Areal electron density (in real space) can be calculated as

$$n_e(\vec{r}, t) = \frac{2}{(2\pi)^2} \int f(\vec{k}, \vec{r}, t) d\vec{k}, \tag{1.12}$$

and the local electrical current density can be calculated as

$$\vec{j}(\vec{r},t) = -e\frac{2}{(2\pi)^2}\int \vec{v}(\vec{k}) f(\vec{k},\vec{r},t) d\vec{k}. \tag{1.13}$$

$\vec{v}(\vec{k}) = \hbar^{-1}\nabla_{\vec{k}}\varepsilon = \hbar\vec{k}/m^*$ is the group velocity of electrons in the conduction band. The distribution function has to satisfy the following (Boltzmann) equation:

$$\frac{\partial f}{\partial t} + \vec{v}\cdot\nabla_{\vec{r}} f + \frac{1}{\hbar}\vec{F}\cdot\nabla_{\vec{k}} f = \left(\frac{\partial f}{\partial t}\right)_c \tag{1.14}$$

where $\vec{F} = -e(\vec{E} + \vec{v}\times\vec{B})$ is the Lorentz force, $(\partial f/\partial t)_c$ accounts for the rate of change of f due to all kinds of collision processes (such as, electron-electron, electron-impurity, electron-phonon, etc.), $\nabla_{\vec{r}} = (\partial/\partial x, \partial/\partial y)$ and $\nabla_{\vec{k}} = (\partial/\partial k_x, \partial/\partial k_y)$ in Cartesian coordinates.

To proceed, we introduce the relaxation-time *ansatz*:

$$\left(\frac{\partial f}{\partial t}\right)_c = -\frac{(f - f^{(0)})}{\tau}. \tag{1.15}$$

f^0 is the Fermi-Dirac distribution. The relaxation time τ is assumed to be energy-dependent. To simplify the problem, we further assume that f is homogeneous.

We look for the steady-state solution to Eq. (1.14) in the form: $f(\vec{k}) = f^0(\varepsilon) + g(\vec{k})$ with $g(\vec{k})$ linear in the electric field $\vec{E}$. To first order in $\vec{E}$, Eq. (1.14) becomes:

$$-\frac{e\hbar}{m^*}(\vec{E}\cdot\vec{k})\frac{\partial f^0(\varepsilon)}{\partial\varepsilon} - \frac{e}{m^*}(\vec{k}\times\vec{B})\cdot\nabla_{\vec{k}} g(\vec{k}) = -\frac{g(\vec{k})}{\tau}. \tag{1.16}$$

It can be shown that $\vec{k}\times\vec{B}\cdot\nabla_{\vec{k}} g(\vec{k}) = -\vec{B}\cdot\vec{k}\times\nabla_{\vec{k}} g(\vec{k}) = -B\partial g(\vec{k})/\partial\varphi$ with φ being the angle between $\vec{k}$ and $\vec{E}$. In the absence of a magnetic field $\vec{B}$, a small electric field $\vec{E}$ will cause a small change $\delta\vec{k} = e\tau\vec{E}/\hbar$ in the electron wave vector and $f(\vec{k}) = f^0(\varepsilon + \delta\varepsilon)$ with $\delta\varepsilon$ being the energy change associated with $\delta\vec{k}$. Performing Taylor series expansion on $f^0(\varepsilon + \delta\varepsilon)$ to the first order in $\vec{E}$, we obtains:

$$f^0(\varepsilon + \delta\varepsilon) \approx f^0(\varepsilon) + \frac{\partial f^0(\varepsilon)}{\partial\varepsilon}\hbar k\frac{e\tau}{m^*}|\vec{E}|\cos\varphi \tag{1.17}$$

where φ is the same angle as defined above. It is therefore rational to assume $g(\vec{k})$ to be in the following form in the presence of $\vec{B}$:

$$g(\vec{k}) = \frac{\partial f^0(\varepsilon)}{\partial\varepsilon}\hbar k\frac{e\tau}{m^*}|\vec{E}|\bar{g}(\varphi). \tag{1.18}$$

$\bar{g}(\varphi)$ is a function to be determined.

With Eq. (1.18), Eq. (1.16) can then be transformed into

$$\cos\varphi - \omega_c\tau\frac{\partial\bar{g}(\varphi)}{\partial\varphi} = \bar{g}(\varphi). \tag{1.19}$$

Expanding $\bar{g}(\varphi)$ in Fourier series: $\bar{g}(\varphi) = \sum_l \bar{g}^{(l)}\exp(il\varphi)$, one finds that $\bar{g}^{(\pm1)} = [2(1 \pm i\omega_c\tau)]^{-1}$ and $\bar{g}^{(l)} = 0$ otherwise. With a little algebra, it can be shown that

$$\bar{g}(\varphi) = \frac{\cos(\varphi-\theta)}{\sqrt{1+\omega_c^2\tau^2}} \tag{1.20}$$

where θ is the Hall angle defined by $\tan\theta = \omega_c\tau$. One therefore finds the solution to Eq. (1.14) as

$$f(\vec{k}) = f^0(\varepsilon) + \frac{\partial f^0(\varepsilon)}{\partial\varepsilon}\hbar k\frac{e\tau}{m^*}\frac{\cos(\varphi-\theta)}{\sqrt{1+\omega_c^2\tau^2}}|\vec{E}|. \tag{1.21}$$

With Eq. (1.13) and Eq. (1.21), the steady-state current densities can then be calculated as

$$\begin{aligned} j_\parallel &= -\frac{2e}{\hbar(2\pi)^2}\int kg(\vec{k})\cos\varphi d\varphi d\varepsilon \\ j_\perp &= -\frac{2e}{\hbar(2\pi)^2}\int kg(\vec{k})\sin\varphi d\varphi d\varepsilon. \end{aligned} \tag{1.22}$$

$j_\parallel$ ($j_\perp$) is the component along (perpendicular to) $\vec{E}$. Since f^0 is isotropic, it does not contribute to the current densities. Using the following relations:

$$\begin{aligned} j_\parallel &= \sigma_{xx}|\vec{E}| \\ j_\perp &= \sigma_{yx}|\vec{E}| \end{aligned} \tag{1.23}$$

and

$$\begin{aligned} \sin\theta &= \frac{\omega_c\tau}{\sqrt{1+\omega_c^2\tau^2}} \\ \cos\theta &= \frac{1}{\sqrt{1+\omega_c^2\tau^2}}, \end{aligned} \tag{1.24}$$

one obtains the longitudinal and transverse conductivities:

$$\begin{aligned} \sigma_{xx} &= \int\left(-\frac{\partial f^0(\varepsilon)}{\partial\varepsilon}\right)\frac{n_e(\varepsilon)e^2\tau(\varepsilon)}{m^*}\frac{1}{1+\omega_c^2\tau^2(\varepsilon)}d\varepsilon \\ \sigma_{yx} &= \int\left(-\frac{\partial f^0(\varepsilon)}{\partial\varepsilon}\right)\frac{n_e(\varepsilon)e^2\tau(\varepsilon)}{m^*}\frac{\omega_c\tau(\varepsilon)}{1+\omega_c^2\tau^2(\varepsilon)}d\varepsilon. \end{aligned} \tag{1.25}$$

$n_{\rm e}(\varepsilon) = m^*\varepsilon/\pi\hbar^2$ has the meaning of areal electron density at $T = 0$ supposing $\varepsilon_{\rm F} = \varepsilon$.

In the limit $T \to 0$, Eq. (1.25) is reduced to

$$\begin{aligned}\sigma_{xx} &\to \frac{n_{\rm e}(\varepsilon_{\rm F})e^2\tau(\varepsilon_{\rm F})}{m^*}\frac{1}{1+\omega_{\rm c}^2\tau^2(\varepsilon_{\rm F})}\\ \sigma_{yx} &\to \frac{n_{\rm e}(\varepsilon_{\rm F})e^2\tau(\varepsilon_{\rm F})}{m^*}\frac{\omega_{\rm c}\tau(\varepsilon_{\rm F})}{1+\omega_{\rm c}^2\tau^2(\varepsilon_{\rm F})}.\end{aligned} \tag{1.26}$$

The conductivities thus take exactly the same forms as those obtained from Drude model (cf. Eq. (1.8)). At a finite temperature and in a weak magnetic field (such that $\omega_{\rm c}\tau(\varepsilon) \ll 1$), Eq. (1.25) is reduced to

$$\begin{aligned}\sigma_{xx} &\approx \frac{n_{\rm e}(\varepsilon_{\rm F})e^2\langle\tau\rangle}{m^*}\\ \sigma_{yx} &\approx \frac{n_{\rm e}(\varepsilon_{\rm F})e^2\langle\tau\rangle}{m^*}\cdot\omega_{\rm c}\langle\tau\rangle\cdot\frac{\langle\tau^2\rangle}{\langle\tau\rangle^2}\end{aligned} \tag{1.27}$$

with the "average" of the nth power of τ defined as

$$\langle\tau^n\rangle = \int\left(-\frac{\partial f^0(\varepsilon)}{\partial\varepsilon}\right)\frac{\varepsilon}{\varepsilon_{\rm F}}\tau^n(\varepsilon)d\varepsilon. \tag{1.28}$$

Using the following general relation in 2D:

$$\begin{aligned}\rho_{xx} &= \frac{\sigma_{xx}}{\sigma_{xx}^2+\sigma_{xy}^2}\\ \rho_{xy} &= \frac{\sigma_{yx}}{\sigma_{xx}^2+\sigma_{xy}^2},\end{aligned} \tag{1.29}$$

the longitudinal and transverse components of ρ are obtained:

$$\begin{aligned}\rho_{xx} &\approx \frac{m^*}{n_{\rm e}(\varepsilon_{\rm F})e^2\langle\tau\rangle}\\ \rho_{xy} &\approx \frac{B}{en_{\rm e}(\varepsilon_{\rm F})}\frac{\langle\tau^2\rangle}{\langle\tau\rangle^2}.\end{aligned} \tag{1.30}$$

The ρ_{xy} obtained here thus differs from the Drude result (cf. Eq. (1.10)) by a factor of $\langle\tau^2\rangle/\langle\tau\rangle^2$.

1.2 Landau quantization

The eigenvalue problem we are trying to solve is the following:

$$\left[\frac{(\vec{p}+e\vec{A})^2}{2m^*}+V(z)\right]\Psi(x,y,z) = \varepsilon\Psi(x,y,z). \tag{1.31}$$

$V(z)$ is a confinement potential in the z-direction and $\vec{A}$ is the vector potential which produces an out-of-plane magnetic field $\vec{B} = B\hat{k}$. By choosing $\vec{A} = (-By, 0, 0)$ and assuming $\Psi(x, y, z) = \psi^{(1)}(x, y)\psi^{(2)}(z)$, Eq. (1.31) becomes:

$$\begin{aligned} &\frac{1}{2m^*}\left[(p_x - eBy)^2 + p_y^2\right]\psi^{(1)}(x,y) = \varepsilon^{(1)}\psi^{(1)}(x,y) \\ &\left[\frac{p_z^2}{2m^*} + V(z)\right]\psi^{(2)}(z) = \varepsilon^{(2)}\psi^{(2)}(z) \end{aligned} \tag{1.32}$$

with $\varepsilon^{(1)} + \varepsilon^{(2)} = \varepsilon$. Due to the confinement potential $V(z)$, bound states arise from the z-equation with discrete energy spectrum $\varepsilon^{(2)} = \varepsilon_i$ $(i = 1, 2, 3, \ldots)$. The bound state energy ε_i is usually called the subband energy.

To proceed, we assume that $\psi^{(1)}(x, y) = \exp(ik_x x)\eta(y)$. After a little algebra, the xy-equation can be cast into:

$$\left[\frac{p_y^2}{2m^*} + \frac{1}{2}m^*\omega_c^2(y - \frac{\hbar k_x}{eB})^2\right]\eta(y) = \varepsilon^{(1)}\eta(y). \tag{1.33}$$

Eq. (1.33) is in the form of an 1D quantum harmonic oscillator and thus the solution is obtained:

$$\begin{aligned} &\eta_n(y) = \frac{1}{\sqrt{2^n \cdot n!}}\left(\frac{1}{\pi\lambda_B^2}\right)^{1/4}\exp\left[-\frac{(y - \lambda_B^2 k_x)^2}{2\lambda_B^2}\right]H_n(\frac{y - \lambda_B^2 k_x}{\lambda_B}) \\ &\varepsilon_n^{(1)} = \hbar\omega_c\left(n + \frac{1}{2}\right) \\ &\text{where } n = 0, 1, 2, \ldots \end{aligned} \tag{1.34}$$

$\lambda_B \equiv \sqrt{\hbar/eB}$ is the magnetic length and H_n is the Hermite polynomial of order n. Although $\eta_n(y)$ depends on k_x, $\varepsilon_n^{(1)}$ does not. Thus, these energy levels (so-called Landau levels) are all highly degenerate. It can be shown that each Landau level hosts eB/h states per unit area (in the xy-plane). The number of Landau levels that are populated by electrons is therefore given as $\nu = n_e/(eB/h) = n_e h/eB$.

If the spin degrees of freedom are taken into account, each Landau level will be split into two branches. Due to Zeeman effect, the Landau ladder of one spin species will have an energy shift (which is equal to twice the Zeeman energy) relative to that of the other. The energy spectrum of a 2D electron in an out-of-plane magnetic field is

therefore quantized as

$$\varepsilon_{i,n,s} = \varepsilon_i + \hbar\omega_{\rm c}\left(n+\frac{1}{2}\right) + s\mu_{\rm B}g^*B$$
$$\text{where } i = 1,2,3,\ldots;\ n = 0,1,2,\ldots;\ s = \pm\frac{1}{2} \tag{1.35}$$

s is the spin quantum number, $\mu_{\rm B} \equiv e\hbar/2m_0 \simeq 5.79\times10^{-5}$ eV/T is the Bohr magneton (m_0 being the bare electron mass), and g^* is the effective g-factor in the host material ($g^* \approx -0.44$ in GaAs). Assuming that only the ground subband ε_1 is occupied by electrons, the 2D density of states (DoS) per unit area in the presence of an out-of-plane $\vec{B}$ thus takes the form:

$$\nu(\varepsilon, B) = \frac{eB}{h}\sum_{n,s}\delta(\varepsilon - \varepsilon_{1,n,s}). \tag{1.36}$$

Here δ is the Dirac delta function.

1.3 Quantum $\vec{E}\times\vec{B}$-drift without scattering

If an in-plane electric field $\vec{E} = E\hat{j}$ (associated with an electrostatic potential $V(y) = -Ey$) is present in addition to an out-of-plane magnetic field $\vec{B} = B\hat{k}$, Eq. (1.33) is modified as

$$\left[\frac{p_y^2}{2m^*} + \frac{1}{2}m^*\omega_{\rm c}^2\left(y - \frac{\hbar k_x + m^*v_{\rm D}}{eB}\right) + \right.$$
$$\left. + \left(\frac{\hbar k_x + m^*v_{\rm D}}{eB}\right)eE + \frac{1}{2}m^*v_{\rm D}^2\right]\eta(y) = \varepsilon^{(1)}\eta(y). \tag{1.37}$$

$v_{\rm D}$ is the group velocity of the electron wave packet. It does not take long before one realizes that Eq. (1.37) is still in the form of an 1D quantum harmonic oscillator. Thus, its solution can be readily written as

$$\eta_n(y) = \frac{1}{\sqrt{2^n\cdot n!}}\left(\frac{1}{\pi\lambda_B^2}\right)^{1/4}\exp\left[-\frac{(y-\lambda_B^2k_x - v_{\rm D}/\omega_{\rm c})^2}{2\lambda_B^2}\right]\times$$
$$\times H_n\left(\frac{y-\lambda_B^2k_x - v_{\rm D}/\omega_{\rm c}}{\lambda_B}\right)$$

$$\varepsilon_n^{(1)}(k_x) = \hbar\omega_{\rm c}\left(n+\frac{1}{2}\right) + eE\left(\lambda_B^2 k_x + \frac{v_{\rm D}}{\omega_{\rm c}}\right) + \frac{1}{2}m^* v_{\rm D}^2$$
$$\text{where } n = 0, 1, 2, \ldots \tag{1.38}$$

According to Eq. (1.38), Landau level degeneracy is completely lifted in the presence of an in-plane electric field $\vec{E}$.

Since $\eta_n(y)$ is the eigenstate of 1D quantum harmonic oscillator Hamiltonian, the expectation value of the y-momentum is zero. The electron wave packet propagates in the x-direction with velocity $v_{\rm D} = \hbar^{-1}\partial\varepsilon_n^{(1)}(k_x)/\partial k_x = E/B$ which is exactly equal to the classical drift velocity in an $\vec{E}\times\vec{B}$ field. As a result, the current density along $\vec{E}$ is zero ($j_\parallel = 0$) and that perpendicular to $\vec{E}$ is finite ($j_\perp = en_{\rm e}v_{\rm D}$). According to Eq. (1.23), one can conclude that

$$\begin{aligned}\sigma_{xx} &= 0\\ \sigma_{yx} &= en_{\rm e}\frac{v_{\rm D}}{E} = \frac{en_{\rm e}}{B}.\end{aligned} \tag{1.39}$$

Using Eq. (1.39) and Eq. (1.29), the corresponding result in the resistivity reads:

$$\begin{aligned}\rho_{xx} &= 0\\ \rho_{xy} &= \frac{B}{en_{\rm e}}.\end{aligned} \tag{1.40}$$

However fascinating, such result is not realistic. A very important ingredient, namely, scattering processes, has been left out from the very beginning. To properly understand electrical transport in real physical systems, it is necessary to take electron scatterings into account.

1.4 Landau level broadening by scattering

A perturbation in the Hamiltonian can lift energy level degeneracy. Such perturbation can be caused by spatial potential fluctuations due to, for instance, random positioning of the background impurity. Electrons experience scatterings in such potential and as a result acquire finite transition probability between different quantum states. According to the energy-time uncertainty relation ($\Delta\varepsilon\Delta t \sim \hbar$), a mean scattering time $\tau_{\rm q}$ is associated with an energy broadening $\hbar/\tau_{\rm q}$. The infinitely narrow DoS spikes in Eq. (1.36) are thus broadened into peaks with finite widths.

To model Landau level broadening theoretically, several forms of DoS have been proposed. The semi-elliptic DoS was first derived in Ref. [2]. It takes the following form:

$$\nu(\varepsilon, B) = \frac{eB}{h} \sum_{n,s} \frac{1}{\pi\Gamma} \sqrt{1 - \left(\frac{\varepsilon - \varepsilon_{1,n,s}}{\Gamma}\right)^2}$$
$$\Gamma = \sqrt{\frac{1}{2\pi}\hbar\omega_{\rm c}\frac{\hbar}{\tau_0}}. \tag{1.41}$$

$\varepsilon_{1,n,s}$ is the energy level defined in Eq. (1.35) and τ_0 is the quantum scattering time at $B = 0$. One drawback of such form of DoS is that levels become unphysical in their tails.

The second proposal is to assume Lorentzian-shape broadening [1][3]:

$$\nu(\varepsilon, B) = \frac{eB}{h} \sum_{n,s} \frac{1}{\pi} \frac{\Gamma}{(\varepsilon - \varepsilon_{1,n,s})^2 + \Gamma^2}$$
$$\Gamma = \frac{\hbar}{2\tau_{\rm q}}. \tag{1.42}$$

$\tau_{\rm q}$ is the quantum scattering time in the presence of a magnetic field and $\tau_{\rm q} = \tau_0$ at $B = 0$. Notice that $\hbar/\tau_{\rm q}$ is not solely determined by the scattering potential. It also depends on $\nu(\varepsilon, B)$ and therefore Γ is not a B-independent parameter in Eq. (1.42). Using the first-order perturbation theory, it was derived that

$$\frac{\hbar}{\tau_{\rm q}} = C\nu(\varepsilon, B) \tag{1.43}$$

where C is a quantity determined by the scattering potential and is independent of ε and B [1]. By combining Eq. (1.42) with Eq. (1.43), one can show that the semi-elliptic DoS is actually recovered.

The third proposal is to assume Gaussian-shape broadening [4][5]:

$$\nu(\varepsilon, B) = \frac{eB}{h} \sum_{n,s} \frac{1}{\sqrt{2\pi}\Gamma} \exp\left[-\frac{(\varepsilon - \varepsilon_{1,n,s})^2}{2\Gamma^2}\right]$$
$$\Gamma = \hbar\sqrt{\frac{\omega_{\rm c}}{2\pi\tau_{\rm q}}}. \tag{1.44}$$

The B-dependence of Γ is actually more complicated than that is suggested by Eq. (1.44). Extensive theoretical work on this subject can be found in Ref. [6]. We will not go into any of those details. For the numerical simulations we are going to present in Chapter 3 and Chapter 6, we adopt Gaussian-shape broadening, *i.e.* Eq. (1.44).

1.5 Thermodynamic density of states

The three different forms of the DoS introduced above can be summarized in the following general expression:

$$\nu(\varepsilon, B) = \frac{2eB}{h} \sum_n L\left[\varepsilon - \hbar\omega_c \left(n + \frac{1}{2}\right)\right]. \tag{1.45}$$

Here, we ignore Zeeman splitting and shift the energy origin to the minimum of the occupied subband. L denotes the functional form of a single Landau level. By applying Poisson's summation formula [7][8], Eq. (1.45) can be expanded as

$$\begin{aligned} \nu(\varepsilon, B) &= \frac{m^*}{\pi\hbar^2}\left[1 + 2\sum_{s=1}^{\infty}(-1)^s \tilde{L}\left(\frac{2\pi s}{\hbar\omega_c}\right)\cos\left(\frac{2\pi s\varepsilon}{\hbar\omega_c}\right)\right] \\ \text{with } \tilde{L}\left(\frac{2\pi s}{\hbar\omega_c}\right) &\equiv \int_{-\infty}^{\infty} L(\xi)\cos\left(\frac{2\pi s\xi}{\hbar\omega_c}\right)d\xi. \end{aligned} \tag{1.46}$$

Notice that $\tilde{L}$ is the Fourier cosine transform of L.

The so-called thermodynamic density of states is defined as [1]:

$$\begin{aligned} \frac{\partial n_e}{\partial \varepsilon_F} &= \frac{\partial}{\partial \varepsilon_F}\int_0^{\infty} \nu(\varepsilon, B) f^{(0)}(\varepsilon) d\varepsilon \\ &= \int_0^{\infty} \nu(\varepsilon, B)\frac{\partial f^{(0)}(\varepsilon)}{\partial \varepsilon_F} d\varepsilon \\ &= -\int_0^{\infty} \nu(\varepsilon, B)\frac{\partial f^{(0)}(\varepsilon)}{\partial \varepsilon} d\varepsilon. \end{aligned} \tag{1.47}$$

$f^{(0)}$, as before, denotes the Fermi-Dirac distribution. $\partial n_e/\partial\varepsilon_F$ has the meaning of density of *occupied* states at the Fermi energy ε_F. With the help of the following analytical result [9]

$$\begin{aligned} &\int_{-\infty}^{\infty}\left(-\frac{\partial f^{(0)}(\varepsilon)}{\partial\varepsilon}\right)\cos\left(\frac{2\pi s\varepsilon}{\hbar\omega_c}\right) = \frac{X_s}{\sinh X_s}\cos\left(\frac{2\pi s\varepsilon_F}{\hbar\omega_c}\right) \\ &\text{with } X_s \equiv \frac{2\pi^2 s k_B T}{\hbar\omega_c}, \end{aligned} \tag{1.48}$$

one obtains the thermodynamic density of states associated with the DoS defined in Eq. (1.46):

$$\frac{\partial n_e}{\partial \varepsilon_F} = \frac{m^*}{\pi\hbar^2}\left[1 + 2\sum_{s=1}^{\infty}(-1)^s \tilde{L}\left(\frac{2\pi s}{\hbar\omega_c}\right)\frac{X_s}{\sinh X_s}\cos\left(\frac{2\pi s\varepsilon_F}{\hbar\omega_c}\right)\right]. \tag{1.49}$$

At a given magnetic field, the modulation in $\partial n_{\rm e}/\partial\varepsilon_{\rm F}$ diminishes with increasing temperature due to the damping factor $X_s/\sinh X_s$. At a given temperature, the oscillations in $\partial n_{\rm e}/\partial\varepsilon_{\rm F}$ are dampened by both $\tilde{L}(2\pi s/\hbar\omega_{\rm c})$ and $X_s/\sinh X_s$ as the magnetic field decreases. One can show that $\tilde{L}(2\pi s/\hbar\omega_{\rm c}) = \exp(-\pi s/\omega_{\rm c}\tau_{\rm q})$ for Lorentzian-shape broadening and $\tilde{L}(2\pi s/\hbar\omega_{\rm c}) = \exp(-\pi s^2/\omega_{\rm c}\tau_{\rm q})$ for Gaussian-shape broadening.

1.6 Shubnikov-de Haas oscillations (SdHOs)

It has been known for decades that many thermodynamic and transport properties in solids oscillate periodically with the reciprocal of the applied magnetic field. Such phenomenon was discovered by Shubnikov and de Haas in bulk bismuth samples where the Hall coefficient was measured [10]. Extensive theoretical work on such effect in metals was carried out by Dingle [8][9]. In 2DEG, Shubnikov-de Haas effect was first observed by Fowler *et al.* in Si MOS structures where the longitudinal conductance was measured [11]. The first attempt of developing a theory for the magneto-oscillations in 2DEG was made by Ando *et al.* [12]. Further theoretical investigations were reported in Refs. [13][14][15][16][17]. Fig. 1.1 shows the typical Subnikov-de Haas oscillations (SdHOs) observed in our high-mobility 2DEG samples.

In the case of a long-range scattering potential and in the regime of a weak magnetic field ($\Gamma/\hbar\omega_{\rm c} \gg 1$ or equivalently $\omega_{\rm c}\tau_{\rm q} \ll 1$), the following expressions for the longitudinal and transverse components of the conductivity tensor were derived [17]:

$$\sigma_{xx} = \frac{e^2 n_{\rm e}\tau_{\rm tr}}{m^*}\frac{1}{1+(\omega_{\rm c}\tau_{\rm tr})^2}\left[1+2\cdot\frac{1-(\omega_{\rm c}\tau_{\rm tr})^2}{1+(\omega_{\rm c}\tau_{\rm tr})^2}\exp\left(-\frac{\pi}{\omega_{\rm c}\tau_{\rm q}}\right)\times \right.$$
$$\left. \times\frac{2\pi^2 k_B T/\hbar\omega_{\rm c}}{\sinh(2\pi^2 k_B T/\hbar\omega_{\rm c})}\cos\left(\frac{2\pi\varepsilon_{\rm F}}{\hbar\omega_{\rm c}}\right)\right] \tag{1.50}$$

$$\sigma_{yx} = -\frac{e^2 n_{\rm e}}{m^*}\frac{\omega_{\rm c}\tau_{\rm tr}^2}{1+(\omega_{\rm c}\tau_{\rm tr})^2}\left[1+\frac{4}{1+(\omega_{\rm c}\tau_{\rm tr})^2}\exp\left(-\frac{\pi}{\omega_{\rm c}\tau_{\rm q}}\right)\times \right.$$
$$\left. \times\frac{2\pi^2 k_B T/\hbar\omega_{\rm c}}{\sinh(2\pi^2 k_B T/\hbar\omega_{\rm c})}\cos\left(\frac{2\pi\varepsilon_{\rm F}}{\hbar\omega_{\rm c}}\right)\right]. \tag{1.51}$$

$\tau_{\rm tr}$ is the transport relaxation time (which is associated with momentum relaxation)

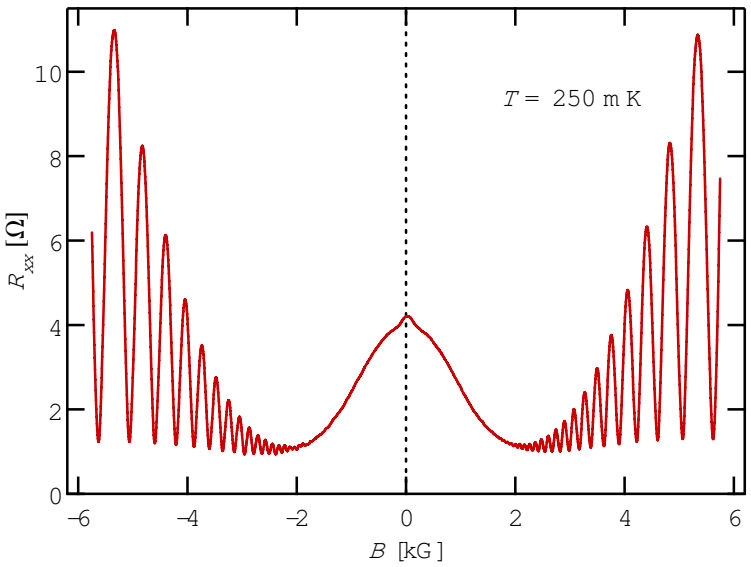

Figure 1.1: Subnikov-de Haas oscillations (SdHOs) in the longitudinal magnetoresistance in a high-mobility GaAs/AlGaAs quantum well sample. The data was taken at $T \simeq 250\,\mathrm{mK}$.

and τ_q is the quantum scattering time (which is related to the lifetime broadening of Landau levels as introduced above).

The longitudinal and transverse components of the resistivity tensor were also obtained [17]:

$$\begin{aligned}\rho_{xx} &= \frac{m^*}{e^2 n_\mathrm{e}\tau_\mathrm{tr}}\left[1-2\exp\left(-\frac{\pi}{\omega_\mathrm{c}\tau_\mathrm{q}}\right)\frac{2\pi^2 k_B T/\hbar\omega_\mathrm{c}}{\sinh(2\pi^2 k_B T/\hbar\omega_\mathrm{c})}\cos\left(\frac{2\pi\varepsilon_\mathrm{F}}{\hbar\omega_\mathrm{c}}\right)\right]\\ \rho_{xy} &= \frac{m^*}{e^2 n_\mathrm{e}\tau_\mathrm{tr}}\omega_\mathrm{c}\tau_\mathrm{tr} = \frac{B}{e n_\mathrm{e}}.\end{aligned} \tag{1.52}$$

The quantum correction to ρ_{xy} on the order of $\exp(-\pi/\omega_\mathrm{c}\tau_\mathrm{q})$ is zero and thus the Hall resistivity is identical to the classical Drude result. Comparing ρ_{xx} with Eq. (1.49) (ignoring terms with $s > 1$), one realizes that they are identical up to a scaling factor independent of the magnetic field. Therefore, SdHOs faithfully reflect how thermodynamic density of states $\partial n_\mathrm{e}/\partial\varepsilon_\mathrm{F}$ varies in responding to a changing magnetic field or a changing Fermi energy.

The periodicity SdHOs exhibiting in $1/B$ has been employed as an alternative way of determining areal electron density n_e (another way being measuring the Hall resistivity at low B). The period of SdHOs $\Delta(1/B)$ is related to the areal electron density by

$\Delta(1/B) = 2e/hn_e$. The quantum scattering time τ_q can be extracted by examining the B-dependence of the SdHO amplitudes at a given temperature [16][18]. The electron effective mass m^* can be determined from the T-dependence of the SdHO amplitudes at a given magnetic field [19].

1.7 Integer Quantum Hall Effect (IQHE)

1.7.1 Phenomenology

Integer quantum Hall effect (IQHE) was discovered by von Klitzing *et al.* in a metal-oxide-semiconductor field-effect transistor (MOSFET) [20]. They observed plateaus in the Hall voltage accompanied by zeros in the longitudinal voltage at high magnetic fields and low temperatures. The Hall resistivity was found to be quantized according to $\rho_{xy} = h/ie^2$ (here i being a positive integer) with stunning accuracy. Their original data is shown in Fig. 1.2. In terms of the components of the conductivity tensor, such results imply a quantized $\sigma_{xy} = ie^2/h$ which is accompanied by a vanishing σ_{xx}. Subsequent studies confirmed the accuracy of such quantization and established the fact that IQHE is universal regardless of the details of the devices in which it is observed. The value $R_K \equiv h/e^2 \approx 25813\,\Omega$ (called the von Klitzing constant) has been adopted as the international standard for electrical resistance. Since the fine structure constant is related to the von Klitzing constant by $\alpha = \mu_0 c/2R_K$, the ability to measure R_K with high accuracy provides a way to determine α with high accuracy. Activated transport in IQHE was observed over a wide temperature range [21][22]. Both the widths of the ρ_{xy} plateaus and the widths of the ρ_{xx} zeros shrink in elevated temperatures [22].

1.7.2 Theoretical explanation

Soon after the discovery of IQHE, Laughlin gave an elegant argument showing that σ_{xy} is quantized exactly as integral multiples of e^2/h under appropriate conditions [23]. At roughly the same time, Thouless came to the same conclusion from a quite different theoretical approach [24]. The important role the edge states play in IQHE was first recognized and advocated by Halperin [25]. A theory combining the edge-state pictures with the Landauer-Büttiker formalism was proposed by Büttiker [26]. In this section,

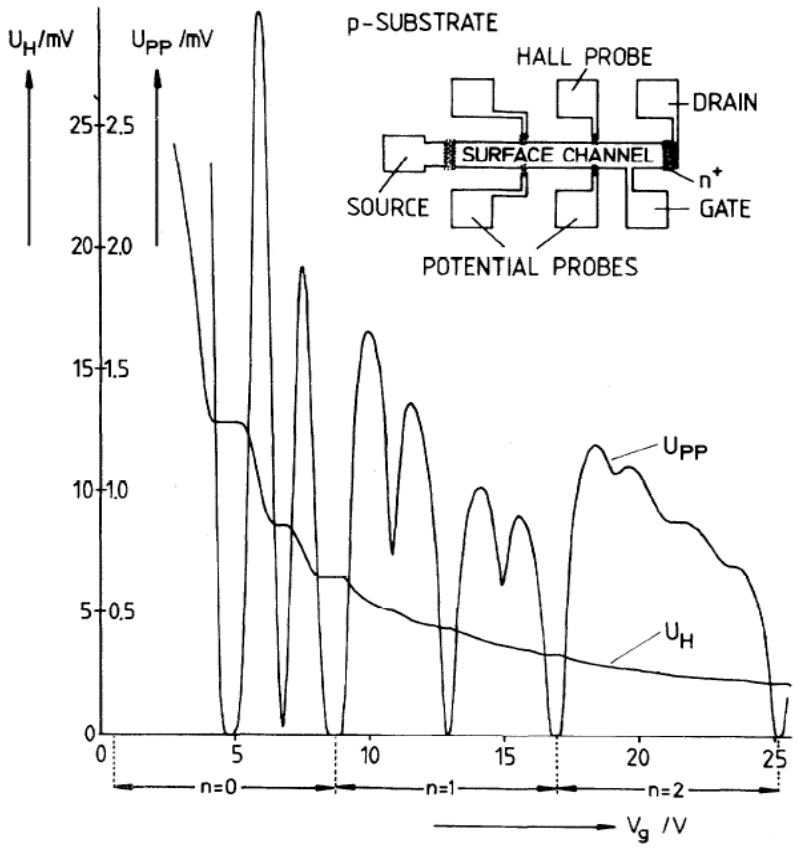

Figure 1.2: The original data showing integer quantum Hall effect (IQHE). The Hall voltage U_H and the longitudinal voltage U_{pp} were measured as a function of gate voltage V_g. The measurement was performed at $B = 18\,\mathrm{T}$ and at $T = 1.5\,\mathrm{K}$. The inset shows the top view of the device. The length and width of the device were $400\,\mu\mathrm{m}$ and $50\,\mu\mathrm{m}$ respectively. The distance between the potential probes was $130\,\mu\mathrm{m}$. The figure was taken from Ref. [20].

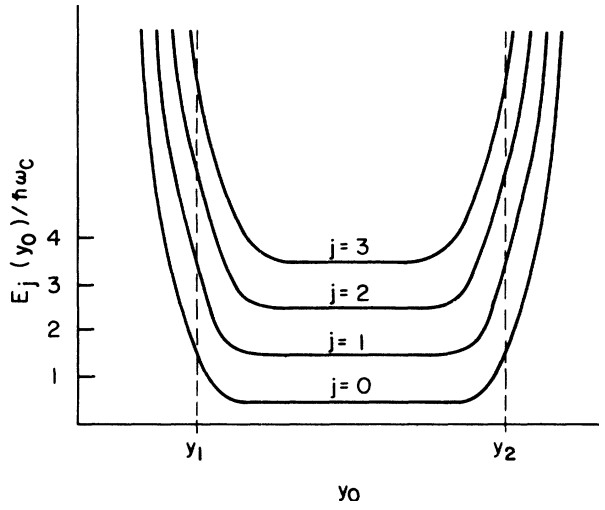

Figure 1.3: The eigenenergies obtained from solving Eq. (1.53) plotted as a function of $y_0 \equiv \lambda_B^2 k_x$. y_0 can be interpreted as the "y-position" of the wavefunction. The boundaries of the 2DEG are located at y_1 and y_2. The figure was taken from Ref. [26].

we will briefly discuss the physics behind IQHE based on this theory.

Let us again consider the eigenvalue problem in Eq. (1.33), but with a little twist:

$$\left[\frac{p_y^2}{2m^*} + \frac{1}{2}m^*\omega_c^2(y - \frac{\hbar k_x}{eB})^2 + U(y)\right]\eta(y) = \varepsilon^{(1)}\eta(y). \tag{1.53}$$

$U(y)$ is a confinement potential in the y-direction. For simplicity, we assume that $U(y)$ is zero in the interior of the 2DEG and it rises steeply when the boundaries are approached. In the interior region, Eq. (1.53) represents nothing but an 1D quantum harmonic oscillator and the solution is given by Eq. (1.34). When the boundaries are approached, Landau level degeneracy is lifted and the eigenenergies increase monotonically [25]. The resulting eigenenergies as a function of the "y-positions" ($y_0 \equiv \lambda_B^2 k_x$) of the wavefunctions are shown in Fig. 1.3. Such dispersion relation suggests that the edge states have larger group velocities than the interior states do. At integer filling factors, there will be no extended states in the interior region and the electrical conduction will be completely carried out by the edge states.

To proceed, let us consider the Hall bar geometry depicted in Fig. 1.4. Here, we assume that the filling factor is equal to an integer i. Terminal 1,2 serve as the current source and drain respectively. Terminal 2,3,5,6 serve as the potential probes. Let us

further assume that the transmission between the adjacent terminals in the clockwise sense by edge-state channels is perfect and the transmission is zero otherwise. According to the Landauer-Büttiker formalism,

$$\begin{pmatrix} I_1 \\ I_2 \\ I_3 \\ I_4 \\ I_5 \\ I_6 \end{pmatrix} = \frac{e^2}{h} \begin{pmatrix} i & 0 & 0 & 0 & 0 & -i \\ -i & i & 0 & 0 & 0 & 0 \\ 0 & -i & i & 0 & 0 & 0 \\ 0 & 0 & -i & i & 0 & 0 \\ 0 & 0 & 0 & -i & i & 0 \\ 0 & 0 & 0 & 0 & -i & i \end{pmatrix} \begin{pmatrix} V_1 \\ V_2 \\ V_3 \\ V_4 \\ V_5 \\ V_6 \end{pmatrix} \tag{1.54}$$

where I_j (V_j) denotes the net current into (the potential at) terminal j (with $j = 1 \sim 6$). Based on the function we assigned to each terminal, the net current into each terminal should be: $I_1 = I$, $I_4 = -I$, and $I_2 = I_3 = I_5 = I_6 = 0$.

From Eq. (1.54), one can then derive that

$$\begin{aligned} V_1 &= V_2 = V_3 \\ V_4 &= V_5 = V_6 \end{aligned} \tag{1.55}$$

and

$$I = \frac{ie^2}{h}(V_1 - V_6). \tag{1.56}$$

The longitudinal and the Hall resistances are then determined as

$$\begin{aligned} R_{xx} &= \frac{V_2 - V_3}{I} = 0 \\ R_{xy} &= \frac{V_2 - V_6}{I} = \frac{V_1 - V_6}{I} = \frac{h}{ie^2}. \end{aligned} \tag{1.57}$$

Eq. (1.57) are consistent with the experimental observations.

In a weakly disordered 2DEG at low temperatures and under strong magnetic fields, scattering processes will not affect Eq. (1.57) because the edge states reside on the opposite edges of the Hall bar have negligible overlap [26]. When the Fermi level lies at a maximum of the DoS, the extended states in the interior region will also contribute to the electrical conduction. Electrons will then have finite probabilities to percolate from one edge to the other and thus reverse their propagation directions. The consequence of this is a modification of the transmission matrix in Eq. (1.54). As a result, R_{xx} becomes

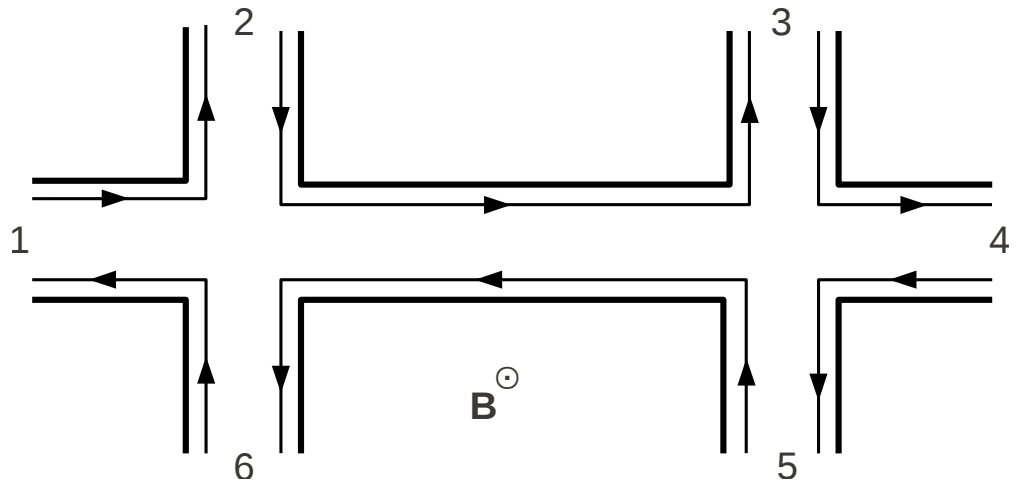

Figure 1.4: Edge-state transport in a typical Hall bar geometry. A magnetic field is applied perpendicular to the 2DEG. A current I is driven from terminal 1 to terminal 4. Edge states are depicted as the arrows that go around the corners. Here, we assume that the filling factor is equal to an integer and so all the interior states are localized.

finite and R_{xy} deviates from its quantized values. Recently, Hashimoto *et al.* probed the local DoS in a 2DEG using scanning tunneling microscopy and provided very strong evidence to this physics picture [27].

1.8 Fractional Quantum Hall Effect (FQHE)

1.8.1 Phenomenology

Quantum Hall plateaus occurring at non-integer values of the Landau level filling factors were first observed by Tsui *et al.* in GaAs/AlGaAs heterostructures at $\nu = 1/3$ and $2/3$ [28]. The accompanying ρ_{xx} minima exhibited activated behaviors [29]. As the crystal growth techniques were continuously improved, more and more quantum Hall plateaus and the concomitant longitudinal resistivity valleys were revealed. Earlier experiments showed only fractional quantum Hall effect (FQHE) at odd-denominator filling factors. Willet *et al.* discovered a FQH state at $\nu = 5/2$ [30] which remains the only even-denominator FQH state ever known in single-layer 2D electron systems [31].

Willet *et al.* also observed that the features appearing (both in ρ_{xx} and ρ_{xy}) at around $\nu = 1/2$ looked strikingly similar to those appearing at around zero field (cf.

Fig. 1.5). Pan *et al.* verified the genuineness of this even-denominator FQH state by showing that ρ_{xy} at $\nu = 5/2$ was quantized to $h/(5/2)e^2$ with extremely high accuracy (to within 2 ppm) which was accompanied by a vanishing ρ_{xx} [32]. Eisenstein *et al.* observed that the $\nu = 5/2$ FQH state collapsed rapidly as the magnetic field was tilted away from the normal to the 2D electron plane [33]. In conjunction with the activation energy data in tilted magnetic fields, the evidence seemed to suggest that $\nu = 5/2$ FQH state is not spin-polarized [34].

1.8.2 Theoretical explanation

The experimental discovery of FQHE spurred a huge amount of theoretical work. It was first pointed out by Laughlin that FQHE signifies a strongly correlated state of interacting electrons underneath [35]. Laughlin identified incompressibility (a gap in the excitation spectrum) as the origin of FQHE, recognized the importance of Jastrow-type correlations, constructed trial wavefunctions for the fundamental $\nu = 1/(2m+1)$ (m being a positive integer) FQH states, and showed that the quasi-particle excitations carry fractional charge [35]. By generalizing Laughlin's concept, Haldane [36] and Halperin [37] showed that the entire sequence of FQH states at $\nu = p/(2mp \pm 1)$ (where m and p are both positive integers) can be generated according to quasi-particle hierarchy schemes.

Jain proposed that the FQHE of electrons can be viewed as the IQHE of a new type of particles called the composite fermions (CFs) [38]. A CF is a bound state formed between an electron and an even number of vortices of the many-body quantum-mechanical wavefunction [31]. In the FQH regime, Coulomb interaction becomes the dominant effect driving the dynamics of electrons. It was found that electrons can avoid each other most efficiently by capturing an even number of vortices of the wavefunction. The strongly correlated liquid of interacting electrons can thus be mapped onto a gas of noninteracting (or weakly interacting) CFs. An important property of these CFs is that they experience a reduced magnetic field rather than the true external field. This is because the phases generated by the vortices while the CFs are winding around one another would partially cancel the Aharonov-Bohm phases originating from the external magnetic field.

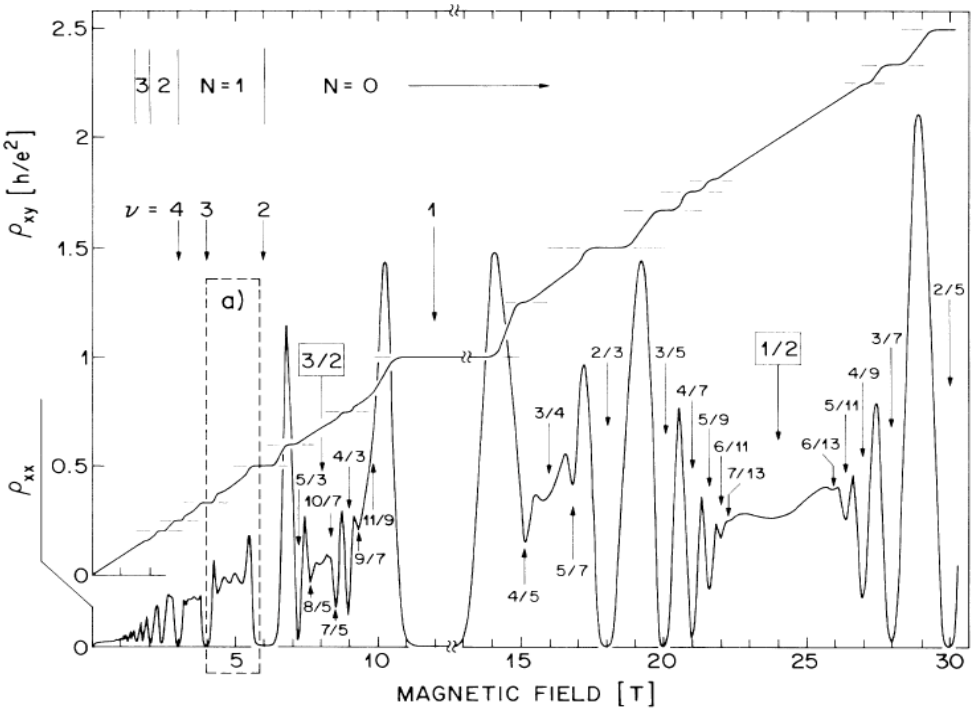

Figure 1.5: Experimental data showing fractional quantum Hall effect (FQHE). The measurements were made in a GaAs/AlGaAs heterostructure with $\mu \simeq 1.3 \times 10^6\,\mathrm{cm}^2/\mathrm{Vs}$ and $n_\mathrm{e} \simeq 3 \times 10^{11}\,\mathrm{cm}^{-2}$. The figure was composed of four different traces with the break at $B \approx 12\,\mathrm{T}$. The temperatures were $\approx 150\,\mathrm{mK}$ except for the high-B ρ_{xy} data which was taken at $T \approx 85\,\mathrm{mK}$. The high-$B$ ρ_{xx} data was scaled down by a factor of 2.5 for clarity. Here, N denotes the Landau level index and ν denotes the filling factor. The even-denominator FQH state at $\nu = 5/2$ cannot be clearly seen without blowing up the region enclosed by the dashed box. The figure was taken from Ref. [30].

A CF can also be viewed as an electron carrying an even number of *fictitious* magnetic flux quanta (arising from the Chern-Simons gauge transformation) [31]. Due to partial cancellation between the Chern-Simons flux and the external flux, CFs experience an effective magnetic field $B^* = B - 2mn_e\phi_0$ (where $\phi_0 \equiv h/e$ is the magnetic flux quantum and m is an positive integer). The CF filling factor $\nu^* \equiv n_e h/e|B^*|$ is then related to the electron filling factor $\nu = n_e h/eB$ by

$$\frac{\nu^*}{\nu} = \pm\frac{B}{B^*} = \pm\frac{B}{(B - 2mn_e\phi_0)} = \pm\frac{1}{(1 - 2m\nu)} \tag{1.58}$$

where the $+$ $(-)$ sign corresponds to the case where B^* is in the same (opposite) direction of B. From Eq. (1.58), one can easily show that

$$\nu = \frac{\nu^*}{2m\nu^* \pm 1}. \tag{1.59}$$

Thus, the CF IQH states at $\nu^* = p$ (with $p = 1, 2, 3, \ldots$) generate the entire sequence of electron FQH states at $\nu = p/(2mp \pm 1)$.

Jain's CF theory explains the odd-denominator FQH states beautifully (but the "outcasts" have also been found [39]). To explain the even-denominator FQH states seems to be more difficult. After Willett *et al.*'s discovery of the $\nu = 5/2$ FQH state [30], Haldane *et al.* proposed a specific spin-singlet trial wavefunction which they thought may be responsible for the observed effect at $\nu = 5/2$ [40]. Not encouragingly, the exact diagonalization studies in finite systems in the limit of no Landau level mixing showed that this trial wavefunction is only a poor representation of the spin-singlet ground states [41]. Within the fermion Chern-Simons theory, it was postulated that an energy gap in the spin-singlet ground state occurs due to BCS (Bardeen-Cooper-Schrieffer) pairing of CFs of opposite spins which could result in the observed $\nu = 5/2$ FQH state [42][43]. The genuineness of such scenario has yet to be proved.

1.9 Microwave-induced resistance oscillations (MIROs)

1.9.1 Discovery of MIROs and ZRS

Earlier work on microwave-irradiated 2DEG revealed a single positive photoresponse peak near cyclotron resonance (CR) condition: $\omega = \omega_c$ (where $\omega = 2\pi f$ is the angular

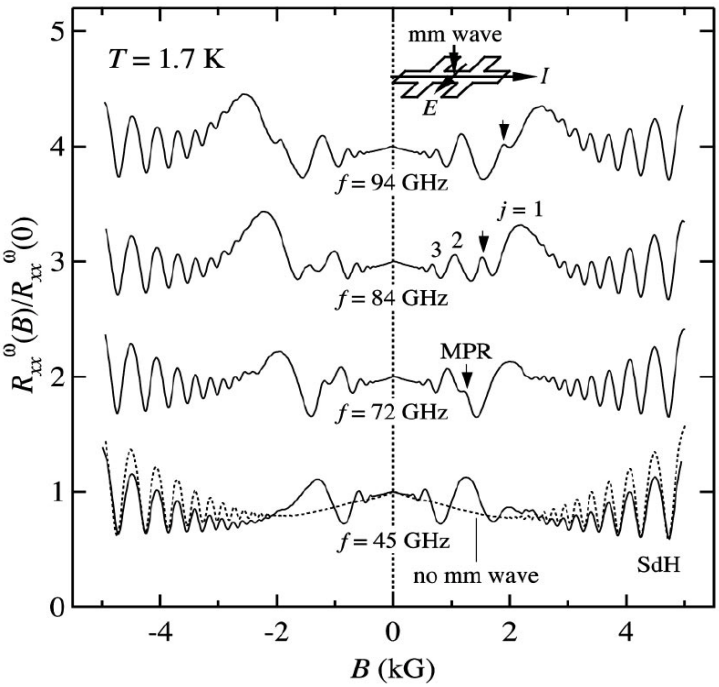

Figure 1.6: Microwave-induced resistance oscillations (MIROs) observed in a GaAs/Al_xGa_{1-x}As heterostructure with $\mu > 3 \times 10^6\,\mathrm{cm}^2/\mathrm{Vs}$. The traces were vertically offset for clarity. The figure was taken from Ref. [46].

frequency of the microwave radiation) [44]. Later, similar experiments performed in GaAs-Al_xGa_{1-x}As heterostructures with mobility $\mu > 3 \times 10^6\,\mathrm{cm}^2/\mathrm{Vs}$ (about 3 times that in the earlier samples) showed pronounced oscillatory photoresponse with both positive and negative values [45][46] (cf. Fig. 1.6). It was observed that the magnitude of photoresponse grew with increasing MW power and it was diminished by raising temperature. The temperature effect on photoresponse, however, was less severe than the thermal damping in Subnikov-de Hass oscillations. These oscillations in photoresponse are periodic in $1/B$ with a period $e/2\pi fm^*$ depending on the MW frequency f. Pairs of photoresponse peak and trough appear near harmonics of CR: $\epsilon_{\mathrm{ac}} \equiv \omega/\omega_{\mathrm{c}} = j$ with $j = 1, 2, 3, \ldots$, etc. The positions of peaks$^+$ and troughs$^-$ (in terms of dimensionless parameter ϵ_{ac}) are roughly described by $\epsilon_{\mathrm{ac}}^{\pm} = j \mp 1/4$ [47]. An analysis showed that this 1/4-cycle phase shift is reduced at lower-order ($j \lesssim 4$) peaks and troughs [3].

Not long after the observations of microwave-induced resistance oscillations (MIROs),

two separate groups reported discovery of MW-induced dissipationless/zero-resistance states (ZRS) in ultra-clean 2DEG with $\mu > 1.5 \times 10^7\,\mathrm{cm}^2/\mathrm{Vs}$ [48][49] (cf. Fig. 1.7). Temperature dependence of these ZRS showed activated behavior with activation energy roughly an order of magnitude larger than the Landau-level spacing $\hbar\omega_\mathrm{c}$ as well as MW quantum energy $\hbar\omega$ [49]. Further investigations on ZRS revealed that the longitudinal voltages were not necessarily all zeros around the 2DEG perimeter and they could even have negative values [50]. Substantial voltage drops between the internal contacts and the contacts on the sample periphery were also detected when the 2DEG was irradiated by microwave but without any applied driving current [50]. These observations seem to be consistent with the theoretical work which postulates that ZRS are formed due to the instability of local absolute negative resistivity/conductivity [51].

The appearance of MIROs/ZRS looks strikingly similar to the longitudinal resistivity in the quantum-Hall regime. The resemblance between the two, nevertheless, is perhaps only cosmetic. Despite the drastic features observed in longitudinal resistivity, Hall resistivity was only weakly affected by MW irradiation and it essentially followed the classical Drude model in this weak magnetic field regime (cf. Fig. 1.7). It was shown that MW photoresponse could also appear in Hall resistivity with a magnitude comparable to that in the longitudinal resistivity (at least under certain conditions) [52]. This effect was usually masked by the large value of dark (w/o MW irradiation) Hall resistivity. Soon after the observations of ZRS in Hall-bar samples, MW-induced zero-conductance states (ZCS) were observed in Corbino samples [53]. By comparing the conductivity measured in Corbino samples with that converted from the measured resistivity in Hall-bar samples, it was shown that the generic relation $\sigma_{xx} \approx \rho_{xx}/\rho_{xy}^2$ holds in MW-irradiated 2DEG [53].

1.9.2 Effect of in-plane magnetic fields

Two different settings have been employed in studying the effect of magnetic fields lying in the 2DEG plane. In the first setting, in-plane magnetic fields ($B_\parallel$) are created by rotating the normal of a 2DEG away from the magnet axis. Since MW radiation propagates down the waveguide along the cryostat axis, its incident angle changes as the 2DEG plane is tilted. In the second setting, the 2DEG plane is fixed. In-plane and out-of-plane magnetic fields are independently provided by a two-axis magnet. MW

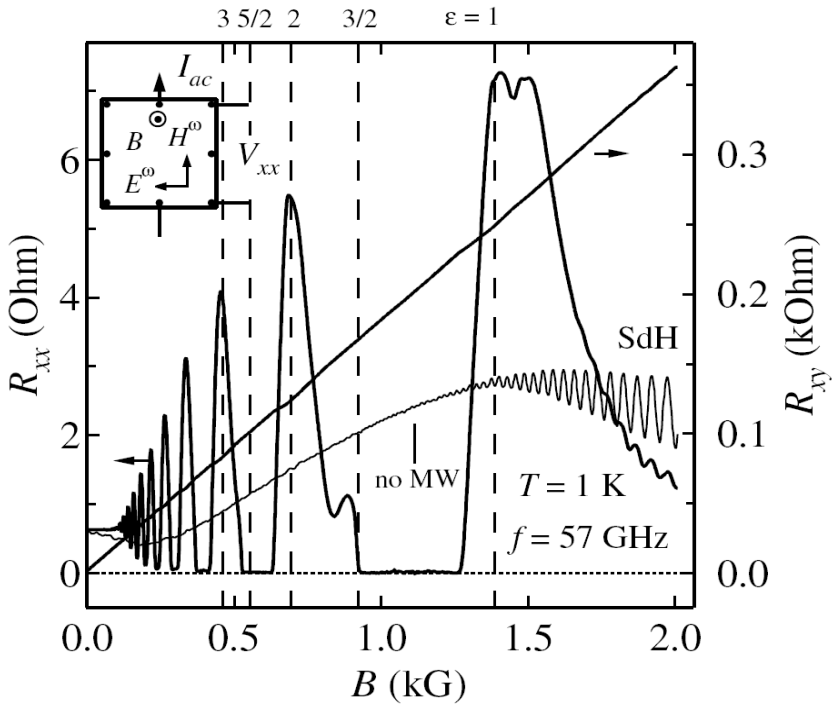

Figure 1.7: Microwave-induced zero-resistance states (ZRS) observed in a GaAs/Al_xGa_{1-x}As quantum well with $\mu \approx 2.5 \times 10^7\,\mathrm{cm}^2/\mathrm{Vs}$. Hall resistivity was only weakly affected by MW irradiation. The figure was taken from Ref. [49].

radiation always impinges on the sample normally in this setting.

So far, the experiments performed in these two different settings did not reveal consistent results. In the first setting, it was observed that MIROs and ZRS were only weakly affected by a tilted magnetic field up to a tilt angle of $\theta = 80°$ with $0.6\,\mathrm{T} < B_{\|} < 1.2\,\mathrm{T}$ [54]. In the second setting, it was reported that MIROs and ZRS were strongly suppressed at $B_{\|} \approx 1\,\mathrm{T}$ [55]. It is not totally clear whether the observations made in the first setting were related to the increase of $B_{\|}$ or the decrease of MW flux (as postulated by Mani in Ref. [54]) or both. The observations made in the second setting did not have such complication. Yang *et al.* suspected that the observed suppression and quenching of MIROs/ZRS in the presence of $B_{\|}$ could be related to the spin degrees of freedom through Zeeman and/or spin-orbit interactions [55]. Later theoretical analysis by Joas showed that spin-splitting due to in-plane magnetic fields does not account for these observations [56].

1.9.3 Polarization dependence

It has been demonstrated experimentally that MIROs are completely insensitive to the polarization state of the incident microwave except at magnetic fields near CR [57]. The polarization dependence near CR is attributed to resonant heating in which active cyclotron resonance absorption (CRA) only occurs in one sense of circular polarization with respect to the magnetic field. These experimental results are particularly important because they immediately rule out those theories which cannot be reconciled with the observed polarization dependence. For instance, the model proposed in Ref. [58] based on the consideration of a non-parabolic dispersion relation of conduction-band electrons can only produce oscillatory photoconductivity in the situation where microwave is linearly polarized. This is apparently in discord with the experimental observations.

Even the most widely accepted theories such as the one based on modification of impurity scattering rates in the presence of MW radiation [59] and the one based on formation of MW-induced non-equilibrium electron energy distribution [60] cannot escape the critical test. They both predict that the correction to the dark dc conductivity in the presence of MW radiation is polarization dependent. In the case where MW power is not too high, the correction to the dark dc conductivity induced by the CRA polarization sense is expected to be larger than that induced by the CRI (cyclotron resonance mode inactive) polarization sense by a factor of $(\omega + \omega_c)^2/(\omega - \omega_c)^2$. This factor is 9 at $\omega/\omega_c = 2$ and it's 4 at $\omega/\omega_c = 3$. Nevertheless, such dramatic difference in MW photoconductivity between the two circular polarization states was not observed in experiments.

1.9.4 Bichromatic photoresistance

Transport measurements in 2DEG under simultaneous MW irradiation of two different frequencies (ω_1, ω_2) provide indirect evidence of absolute negative resistivity. It has been observed that bichromatic MW photoresistance is related to its individual monochromatic components through a linear combination except at magnetic fields where one component shows ZRS but the other doesn't or at magnetic fields where one component shows a resonance peak due to multi-photon processes [61]. In terms of total resistance (*i.e.* the sum of dark resistance and photoresistance), the experimental observations

were summarized as:

$$R_{\rm exp}^{\omega_1\omega_2} = \max\{\alpha R^{\omega_1} + (1-\alpha)R^{\omega_2}, 0\} \tag{1.60}$$

The weighting, α, is determined by the power (or more precisely, the intensity) ratio of the two frequency components. In the case where the two individual monochromatic components saturate at roughly the same intensity of MW irradiation, $\alpha \approx 1/2$.

Experimental data showed that $R_{\rm exp}^{\omega_1\omega_2}$ was significantly smaller than the average of the observed R^{ω_1} and R^{ω_2} when one of them turned out to be zero (*i.e.* at ZRS). This suggests that a negative contribution to total resistance could come from one of the frequency components at certain magnetic fields when a 2DEG is subjected to bichromatic MW irradiation. It is natural to postulate that this negative contribution comes from the frequency component which exhibits ZRS when the 2DEG is under its irradiation alone. Assuming equal contribution from the two frequency components (*i.e.* $\alpha = 1/2$), it was suggested that a quantitative estimation of negative resistance can be obtained from Eq. (1.60):

$$R^{\omega_1(\omega_2)} = 2R_{\rm exp}^{\omega_1\omega_2} - R^{\omega_2(\omega_1)} \tag{1.61}$$

The quantities appear on the right-hand side of Eq. (1.61) are measured (positive) values. The quantity appears on the left-hand side is the hypothetical negative resistance.

1.9.5 Theoretical explanations of MIROs/ZRS

Experimental observations of MIROs/ZRS in high-mobility 2DEG have triggered a vast amount of theoretical work surrounding this subject. Currently, two microscopic mechanisms are most widely accepted as being responsible for these transport phenomena. The first mechanism involves indirect inter-Landau-level scatterings in which electrons absorb/emit MW quanta and are elastically scattered by impurity. The second mechanism stems from MW-induced non-equilibrium electron energy distribution in which inverted occupation of electronic states can occur under appropriate conditions. In this section, we will only focus on these two mechanisms. Other less popular (or less relevant) mechanisms, such as photo-assisted quantum tunneling [62] and non-parabolicity effects [58] etc, will not be discussed here.

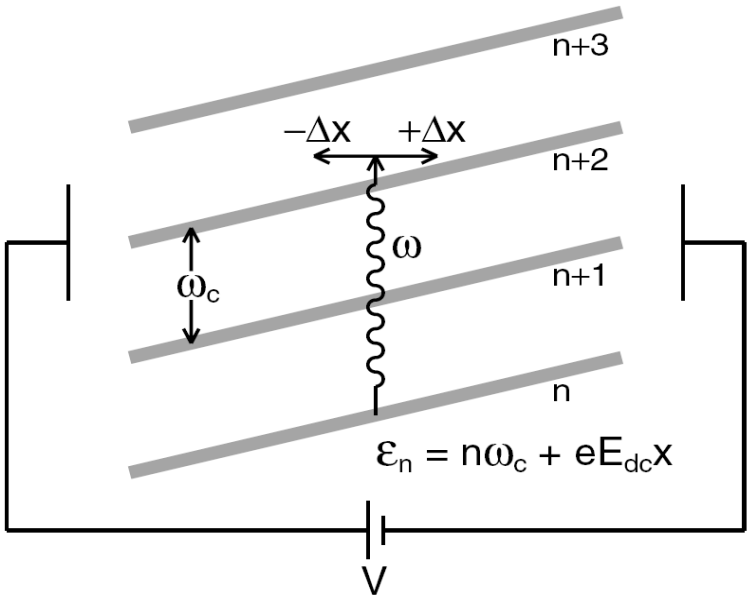

Figure 1.8: Illustration of indirect inter-Landau-level scattering. In this diagram, $\hbar$ is set to equal unity and the constant energy shift $\hbar\omega_c/2$ in the Landau ladder is omitted. The figure was taken from Ref. [65].

1.9.5.1 Indirect inter-Landau-level scattering

The theoretical considerations along this line can be traced all the way back to Ryzhii *et al.* [63][64]. The first attempt to develop a theory for MIROs/ZRS based on such a picture was made in Ref. [65]. This work was followed by a series of similar theoretical efforts (see, for instance, Refs. [66][67][68][69][70]). The most comprehensive theory was presented in Ref. [59].

This mechanism can be intuitively understood as follows (cf. Fig. 1.8). A dc electric field E_{dc} creates a spatial gradient in the energy spectrum: $\varepsilon_n = (n + 1/2)\hbar\omega_c + eE_{dc}x$. Energy levels are depicted as thick slanted lines in Fig. 1.8. Supposing that a microwave quantum with energy $\hbar\omega$ slightly larger than $2\hbar\omega_c$ is absorbed by an electron in the nth Landau level. This electron would not be able to make a transition to the $(n + 2)$th Landau level unless it is spatially displaced by a distance Δx. Since the DoS to the right of this excited electron is larger than that to its left, its preferential displacement is to the right. Notice that the displacement here is referred to the spatial shift of electron guiding center (*i.e.*, the center of the electron cyclotron orbit). This action results in a

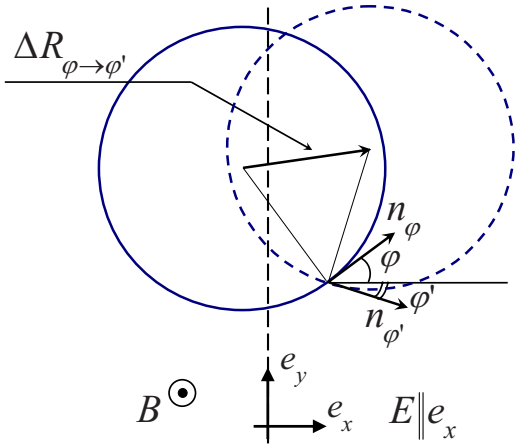

Figure 1.9: Illustration of the displacement of electron guiding center. The circles depict cyclotron orbits. The direction of initial (final) momentum is denoted by n_φ ($n_{\varphi'}$). $\Delta R_{\varphi\to\varphi'}$ denotes the guiding center displacement. The figure was taken from Ref. [71].

photocurrent flowing against the dark dc current.

The decrease of total current through the sample reflects on the decrease of sample conductivity. If instead, $\hbar\omega$ is slightly smaller than an integral multiple of $\hbar\omega_c$, the displacement of guiding center will result in a photocurrent flowing with the dark dc current and therefore the detected conductivity of the sample will increase. The displacement of electron guiding center is achieved by momentum transfer between the electron and impurity through elastic scattering process (cf. Fig. 1.9).

MW photoconductivity originating from this mechanism was given as [72]:

$$\frac{\sigma^{(\mathrm{ph})}}{\sigma_D} = -4\delta^2 \left[\sin^2 \pi\epsilon_{\mathrm{ac}} + \pi\epsilon_{\mathrm{ac}} \sin 2\pi\epsilon_{\mathrm{ac}}\right] \frac{\tau_{\mathrm{tr}}}{2\tau^*} \sum_{\pm} \mathcal{E}_{\pm}^2 \tag{1.62}$$

$\sigma_D = e^2\nu_0 v_{\mathrm{F}}^2/2\omega_c^2\tau_{\mathrm{tr}}$ is the Drude conductivity, ν_0 is the DoS at $B = 0$, v_{F} is the Fermi velocity, τ_{tr} is the transport relaxation time, $\delta = \exp(-\pi/\omega_c\tau_q)$ is the Dingle factor and $1/\tau^* = 3/\tau_0 - 4/\tau_1 + 1/\tau_2$ where τ_n is the nth harmonic of elastic scattering rate $\tau(\theta)^{-1}$ (with θ being the scattering angle):

$$\frac{1}{\tau(\theta)} = \sum_{n=-\infty}^{+\infty} \frac{e^{in\theta}}{\tau_n}. \tag{1.63}$$

Dimensionless parameter $\mathcal{E}_\pm$ is proportional to microwave electric field E_ω:

$$\mathcal{E}_\pm = s_\pm \frac{e v_\mathrm{F} E_\omega}{\hbar\omega(\omega \pm \omega_\mathrm{c})} \tag{1.64}$$

$s_\pm = \pm 1$ parametrizes the polarization state of the incident microwave.

1.9.5.2 MW-induced non-equilibrium energy distribution

This mechanism was first proposed in Ref. [73]. The theory was further developed in Refs. [74][75][60]. It was shown, by solving a kinetic equation, that in the presence of MW radiation the modulation in the DoS (due to Landau quantization) can induce a modulation in the electron energy distribution. A small modulation in the electron energy distribution could result in a dramatic change in the dc conductivity: $\sigma = \int d\varepsilon \left(-\frac{\partial f(\varepsilon)}{\partial \varepsilon}\right) \sigma(\varepsilon)$ (where $f(\varepsilon)$ is the electron energy distribution and $\sigma(\varepsilon)$ is the contribution of electrons with energy ε to dissipative transport) [60].

In the energy interval(s) where population inversion occurs, $\partial f(\varepsilon)/\partial\varepsilon$ becomes positive and therefore these electrons (with ε within such interval(s)) give a negative contribution to the dc conductivity. As illustrated in Fig. 1.10, the inverted occupation of electronic states occurs when the incident MW quantum has energy $\hbar\omega$ larger than the cyclotron energy $\hbar\omega_\mathrm{c}$. Redistribution of electron energy will still take place when $\hbar\omega < \hbar\omega_\mathrm{c}$, but there will be no population inversion in this case and all the electrons will give positive contribution to the dc conductivity. MW photoconductivity stems from this mechanism was given as [72]:

$$\frac{\sigma^{(\mathrm{ph})}}{\sigma_D} = -4\delta^2 \left[\pi\epsilon_\mathrm{ac} \sin 2\pi\epsilon_\mathrm{ac}\right] \frac{2\tau_\mathrm{in}}{\tau_\mathrm{tr}} \sum_\pm \mathcal{E}_\pm^2 \tag{1.65}$$

where τ_in is the inelastic relaxation time. At low temperatures, it is mainly determined by electron-electron collisions.

1.9.5.3 Current domains

Both mechanisms predict that MW photoconductivity $\sigma^{(\mathrm{ph})}$ grows with increasing MW intensity (cf. Eq. (1.62) and Eq. (1.65)). The magnitude of $\sigma^{(\mathrm{ph})}$ can exceed the dark dc conductivity at sufficiently high MW intensity and thus the minima of the dc conductivity could become negative. The instability associated with absolute negative conductivity has been acknowledged since the work in Ref. [76]. It was shown by Andreev *et*

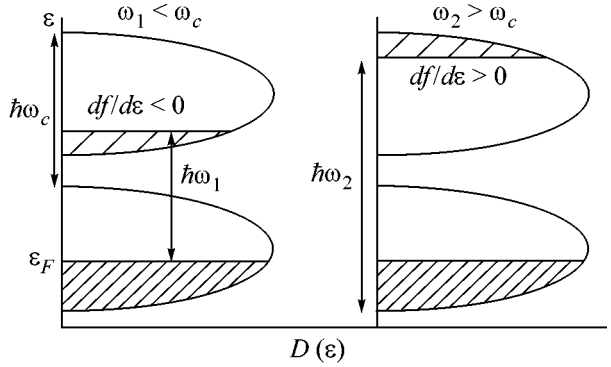

Figure 1.10: Illustration of electron energy redistribution induced by MW radiation. Vertical axis is the energy (ε). Horizontal axis is the DoS ($D(\varepsilon)$). Population inversion occurs when the incident MW quantum has energy greater than the cyclotron energy ($\hbar\omega_2 > \hbar\omega_c$). In the case where MW quantum has energy smaller than the cyclotron energy ($\hbar\omega_1 < \hbar\omega_c$), redistribution of electron energy will still take place but there will be no population inversion. The figure was taken from Ref. [73].

al. that the existence of a local negative dc conductivity (regardless of the underlying microscopic mechanism) is sufficient to explain the observed ZRS [51]. Their analysis led to the following conclusions: 1.) a homogeneous time-independent current carrying state with absolute negative conductivity is unstable under perturbation (e.g. inhomogeneous current fluctuation); 2.) the only possible stationary state is one in which the magnitude of local current density is equal to certain finite value j_0 everywhere except for isolated points (vortex cores) or lines (domain walls). The dissipative component of the local electric field (E_x) is zero at j_0 under the assumption that MW-irradiated 2DEG exhibits a generic N-shape field-current (E_x-j_x) characteristic (in which dissipative resistivity $\rho_d = E_x/j_x < 0$ when $|j_x| < j_0$). A homogeneous current state with $|j_x| < j_0$ will break into current domains and as a result electrical transport becomes dissipationless. Similar analyses were also carried out in Refs [62][77][78][79][59].

1.9.6 Effect of MW radiation on SdHOs

The presence of MW radiation could strongly suppress SdHOs [73][80][81]. It was reported that SdHOs in MW-irradiated 2DEG were pinched at around CR [82]. Since MW photoresponse is null at CR ($\omega/\omega_c = 1$), such a node suggests that the resistivity/conductivity at CR is not simply the algebraic sum of MW-induced change and the

dark value. Based on this fact, it was inferred that electron scatterings in 2DEG must have been modified by the presence of MW fields [82]. Although MIROs/ZRS were usually studied at magnetic fields below the onset of SdHOs, it has been experimentally shown that they could also occur when the 2DEG exhibited SdHOs [80]. It was observed that SdHOs were dampened significantly at MIRO minima and they completely disappeared (at the MIRO minima) once ZRS have developed [80].

At radiation frequencies (ω) below a certain characteristic frequency ($\omega_0 = 2\Gamma/\hbar$ with Γ being the half width of a broadened Landau level), it was reported that MW radiation not only suppressed SdHOs but also reduced the average magnetoresistivity over a substantial range of magnetic field [54][81]. When $\omega > \omega_0$, the experimental data showed that there existed a narrow range of magnetic field (around $\omega_c = 2 \cdot \omega$ and $\omega_c = 2/3 \cdot \omega$) within which SdHOs were essentially unaffected by MW radiation [81]. It has been shown numerically that the observations made at $\omega < \omega_0$ could be attributed to formation of non-equilibrium electron energy distribution [81]. Population inversion occurs in the highest occupied Landau level due to MW-induced intra-Landau-level scatterings. The inverted population results in a negative contribution to magnetoresistivity. The existence of a window of magnetic field within which SdHOs were very much immune to MW radiation was also reproduced in numerical simulations [81]. Such window signifies a regime where inter-Landau-level scatterings (occurring at lower B) have subsided and intra-Landau-level scatterings (occurring at higher B) have not set in. Thus, MW quanta could only be weakly absorbed within such window.

1.10 This Thesis

In this thesis, we present our studies on nonlinear electrical transport in high-mobility 2DEG. Experimental data and numerical results will be presented following the discussion of experimental details in Chapter 2. The transport nonlinearity under our investigation here arises from a pure dc-current bias as well as from simultaneous MW irradiation and a dc-current bias. The basic motivation behind a series of research along this line is to search for a critical current density predicted by a current-domain model regarding the formation of ZRS in MW-irradiated 2DEG [51].

First, we will focus on the transport nonlinearity purely induced by a dc-current bias.

In Chapter 3, we discuss Hall-field induced resistance oscillations (HIROs). Phenomenologically, HIROs in dc-current biased 2DEG are similar to MIROs in MW-irradiated 2DEG. A dc-current bias not only can induce periodic oscillations in differential resistivity, but it also has the ability to induce zero differential resistance state (ZdRS) which is analogous to ZRS forming in 2DEG under MW irradiation. We discuss ZdRS in Chapter 4.

The rest of the thesis will be devoted to the transport nonlinearity occurring in 2DEG under simultaneous MW irradiation and a dc-current bias. In Chapter 5, we discuss oscillations in differential resistivity with the applied dc-current bias at various values of $\epsilon_{\rm ac}$. The oscillations show non-monotonic dependence on parameter $\epsilon_{\rm ac}$. MIRO-like feature not only occurs near CR and its harmonics, but it also appears near subharmonics of CR. In Chapter 6, we discuss a peculiar "synchronization" behavior between the MIRO-like features near CR and its second subharmonic as the dc-current bias is varied.

As MW intensity increases, additional resonance peaks and troughs appear near CR and its harmonics. The positions (in terms of parameter $\epsilon_{\rm ac}$) of these peaks and troughs are strongly dependent on the power of the microwave that irradiates the 2DEG. We discuss these observations in Chapter 7. Finally, a conclusion will be given in Chapter 8. In order to get better understanding on the observed transport nonlinearity, we compare experimental data with the existing theories throughout the thesis. Most of the numerical results are obtained using the theoretical work put forth by Khodas *et al.* [71].

Chapter 2

Experimental details

2.1 High mobility 2DEG samples

Our samples were cleaved from symmetrically doped GaAs/$Al_{0.24}Ga_{0.76}As$ quantum wells grown by Loren Pfeiffer and Ken West at Bell Labs, Alcatel Lucent. Fig. 2.1 shows the sample structure. The quantum well was 30 nm wide. The spacer separating the Silicon δ-doping layer from the well is 80 nm thick. Electron density (n_e) was determined from the periodicity of Shubnikov-de Haas oscillations and/or low-field Hall resistivity. Electron mobility (μ) was determined from zero-field sheet resistance as well as n_e using the simple Drude model. The post-sample processing n_e and μ were $3.7 \sim 3.8 \times 10^{11}\,\mathrm{cm}^{-2}$ and $1.0 \sim 1.3 \times 10^{7}\,\mathrm{cm}^2/\mathrm{Vs}$, respectively. These values were obtained at $T \simeq 1.5\,\mathrm{K}$ after briefly illuminating the samples with visible light.

To understand how 2DEG was formed in such structures and why these structures were engineered in this way, let us start out by considering two pieces of semiconductor materials: one of them is a piece of n-doped AlGaAs and the other is a piece of undoped GaAs. The band-edge diagram immediately after these two pieces of materials are brought together (before charge redistribution takes place) is shown in Fig. 2.2. The valence electrons originally bound to the donors can be thermally excited into the conduction band of AlGaAs. These electrons will then flow into the conduction band of GaAs because there they have access to lower energy states. Due to the spatial separation of these electrons from their ionized donors, an electric field will build up in the transition region and the Coulomb attraction will ensure that electrons can only move

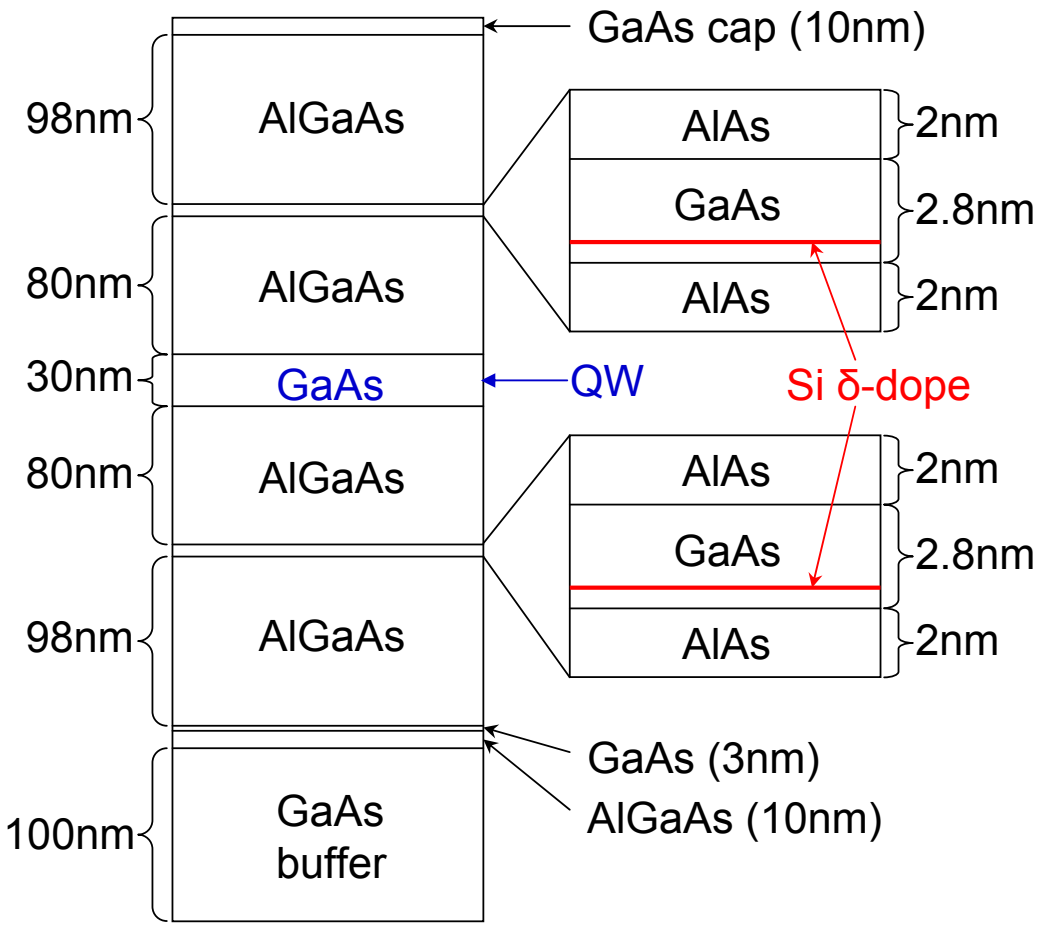

Figure 2.1: Sample structure.

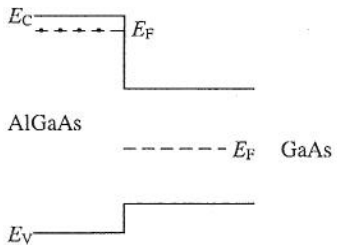

Figure 2.2: Band-edge diagram of a GaAs-AlGaAs heterojunction before new equilibrium is established. AlGaAs is n-doped and GaAs is undoped. E_c and E_v denote conduction and valence band-edge energy, respectively. Valence electrons originally bound to the donors can be thermally excited to the conduction band of AlGaAs. They will then be swept into the conduction band of GaAs. Ultimately, the chemical potentials of these two materials have to be at the same level. The diagram was taken from Ref. [83].

near the heterojunction interface. Since these electrons are now at lower energy level, they won't be able to overcome the barrier and recombine with their donors. Thus, a thin sheet of electrons is formed. Fig. 2.3 shows the band-edge diagram after charge redistribution has taken place and a new equilibrium is reached. The band-bending near the heterojunction interface is due to charge accumulation on both sides of the interface. Chemical potential is equilibrated in the entire structure.

It was discovered that two main factors affect electron mobility in the 2DEG: interface roughness and scattering by ionized donors in the barrier material. Interface roughness can be minimized by employing epitaxial techniques (MBE or MOCVD) in crystal growth. The perfection of GaAs-AlGaAs interface makes it an excellent material system when very high electron mobility is demanded. Scattering due to ionized donors can be reduced by inserting a "spacer" between the doped region and the heterojunction interface. If δ-doping is implemented, the scattering due to ionized donors can be further reduced. This is because all the free charge in the barrier material would now be tightly bound to the donor sheet. The Coulomb potential due to random positioning of ionized donors will then be screened out and a more uniform charge distribution will be seen by the 2DEG [83]. Implementing δ-doping also maximizes the number of carriers that could actually go into the 2DEG and reduces the risk of inducing parasitic conduction channels in the doped region.

If a back barrier does not exist, electrons might travel along undesired paths within

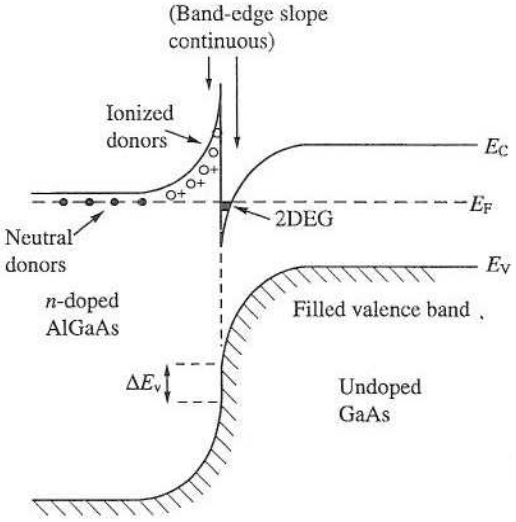

Figure 2.3: Band-edge diagram of a GaAs-AlGaAs heterojunction after charge redistribution has taken place and new equilibrium is reached. The diagram was taken from Ref. [83].

the substrate (cf. I_{par} in Fig. 2.4(a)). This problem can be solved in two different ways: introducing a p-type layer or a wider bandgap layer into the substrate. The resulting band-edge diagrams after introducing these two types of buffer layers are shown in Fig. 2.4(c)(d). The reason a p-type layer can provide a back barrier is because a negative space-charge region will be formed adjacent to the 2DEG when this p-type layer is fully depleted. Practically, using a wider bandgap layer to avoid the back barrier to substrate injection is the preferred design for GaAs-based structures. Finally, it is known that carrier freeze-out occurs at low temperatures in doped semiconductors. This issue is avoided in modulation-doped heterostructures. This is because the 2D electrons in these structures are at lower energy level than that of the donors'. The superior low temperature performance ensures that devices fabricated from these structures can function properly at low temperatures.

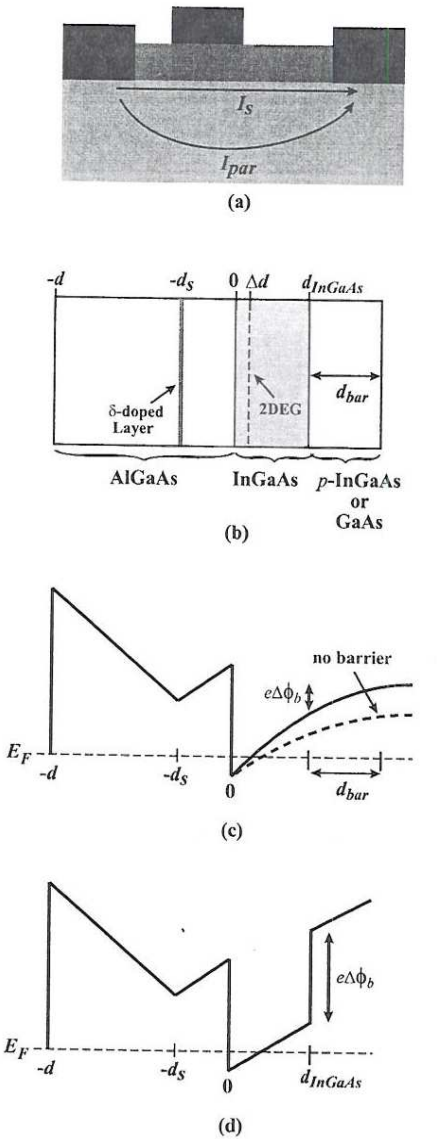

Figure 2.4: A MODFET (modulation-doped field-effect transistor) structure. (a) Without a back barrier, a parasitic leakage current I_{par} might flow within the substrate. (b) A MODFET structure which incorporates a back barrier. (c) Conduction band-edge profile for the structure depicted in (b) if the back barrier is provided by a p-type material. (d) Same as (c) except that the back barrier is provided by a wider bandgap material. The diagrams were taken from Ref. [84].

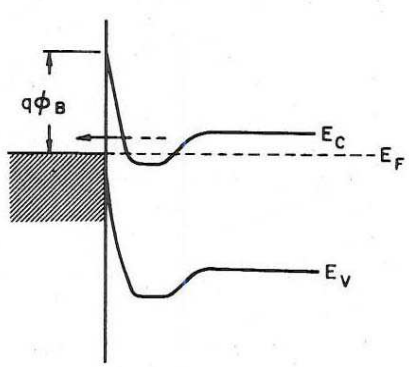

Figure 2.5: Band-edge profile of an Ohmic contact. The semiconductor region right next to the metal is heavily doped. Farther away from the metal-semiconductor interface, the doping concentration is lower. The diagram was taken from Ref. [85].

2.2 Sample processing

2.2.1 Hall bar structures

Samples were shaped into Hall bar bridges by photolithography and chemical etching. The whole procedure could be divided into two major steps: 1.) Transferring mesa pattern onto 2DEG; 2.) Making Ohmic contacts. Ordinarily, a top gate will also be incorporated into the Hall bar bridge to allow control over the 2D electron density. In our case, however, the top gate was not fabricated because our experiments required 2DEG to be exposed to MW radiation.

2.2.2 Ohmic contacts

In principle, Ohmic contacts can be realized in two different ways: 1.) lowering the Schottky barrier height; 2.) creating a heavily doped region in the semiconductor right next to the metal. In III-V compound semiconductors, however, the Schottky barrier height cannot easily be reduced by choosing the metal that is used in contact with them due to Fermi level pinning at the semiconductor surface [84]. Because of such constraint, making Ohmic contacts to III-V compound semiconductors are usually achieved through the second approach. Fig. 2.5 shows the band-edge profile of an Ohmic contact that is realized in this way.

Many different techniques have been developed to fabricate Ohmic contacts on III-V

compound semiconductors. Here we only discuss the alloy regrowth technique which is the technique we were actually using. We chose Au-Ge eutectic mixture (*i.e.* 88wt% Au and 12wt% Ge) as contact material [85]. Our recipe is given below:

- The multi-component contact material was deposited onto the semiconductor surfaces under reduced atmospheric pressure according to the following order and thickness:
  Ni/Au/Ge/Au/Ni/Au=5 nm/100 nm/100 nm/100 nm/70 nm/20 nm
- Annealing was carried out according to the following temperature profile:
  1. Flowing of forming gas (a mixture of hydrogen and nitrogen gas with 1-5.7 mol% of hydrogen) with heat off to purge the chamber (4 minutes)
  2. Heating at 370°C (120 seconds)
  3. Heating at 440°C (50 seconds)
  4. Ramping down temperature with forming gas on to cool the chamber below 100°C (at least 2 minutes)

The bottom Ni thin layer was deposited for increasing the wetting of the eutectic Au-Ge film. The top Au layer mainly served the purposes of bonding and interconnection. The rapid heating procedure was to reduce the irregular penetration of Ni-As-Ge grains into the GaAs layer.

The metallurgical behavior of alloying Au-Ge/Ni with GaAs has been studied extensively (see, for instance, Ref. [86][87][88]). The role each component plays in the alloying process is summarized below:

- Ge occupies Ga sites in GaAs and is used as an n^+ dopant.
- Au acts as a selective getter for Ga.
- Ni serves as a catalyst for the chemical reactions between Au and GaAs. It also provides the driving force for Ge diffusion.

The proportion of the components in the contact material is important. Excess Au can create too much Ga vacancies which cannot be completely filled by available Ge. Such non-stoichiometric condition can result in a high resistivity region at the surface layer of GaAs. It has been observed that excess Ni can also degrade the Ohmic contacts.

2.3 Mounting samples

The processed samples were mounted onto 8-pin or 16-pin headers. The connections between the contact pads and the header pins were established through gold bonding wires. Wire bonding was achieved by soldering using pure indium solder. Pure indium was chosen because of its low melting point (156.6°C) and high ductility. Indium and gold form intermetallic compounds which provide mechanically strong bonds with low resistivity. The robustness of the bonding is very important because it can minimize the risk of bonding wires detaching from contact pads during cooled-down process.

Another important reason for choosing soldering as bonding technique was that it did not impose mechanical stresses on the contacts during wire bonding. It is known that mechanical stresses on heterostructures can easily induce electrically active structural defects. These structural defects act as acceptors. Once they are induced in the regions directly beneath the contacts, they will capture electrons and thus increase contact resistance. At low temperatures, contacts could even cease to carry currents due to the underlying structural defects [89].

Samples were secured to the headers by tying them down using strands of PTFE (polytetrafluoroethylene, alias Teflon) tape. This simple technique has an added advantage. Since no adhesive substances were used, removing a sample from its header is very straightforward if there is any need to do so. A homemade socket (16 pins) was made to host the header and connect it to the circuitry of the cryostat top loading probe.

2.4 Transport measurements

2.4.1 Checking Ohmic contacts

The quality of Ohmic contacts could potentially affect experimental outcomes. Thus, it is necessary to check them before making any measurement. Usually, we checked pairs of Ohmic contacts both at room temperature and at liquid helium temperature. The typical room-temperature 2-terminal resistance was between 10 kΩ and 100kΩ in our samples. The corresponding value at liquid helium temperature was between 100 Ω and 1 kΩ. Comparing the 2-terminal resistance to the 4-terminal resistance (typically, several tens of ohms at $\sim$ 4.2 K), we estimated that the resistance due to the Ohmic

contacts and the rest of the circuitry was several hundreds of ohms.

2.4.2 Precision electronic measurement

4-terminal resistance was measured by standard phase-sensitive detection. The setup is schematically shown in Fig. 2.6. A sine wave with a known frequency (typically a few Hz) and a known amplitude (typically 1 V) was generated by the internal oscillator of a lock-in amplifier (SRS Model SR830 DSP or SIGNAL RECOVERY Model 7265 DSP). This low-frequency oscillating voltage was applied across a 1 MΩ or 10 MΩ resistor and as a result a small ac current (with an amplitude typically 1 μA) was produced. This ac current was sent down to the sample and the response (a small ac voltage) of the 2DEG was detected by a lock-in amplifier. The ratio of the measured voltage to the input current gave the absolute resistance in the linear response regime. Sheet resistance was computed by the data acquisition software in real time.

To explore the territory beyond the linear response regime, a dc bias was generated by a current source (Keithley Model 2400 SourceMeter) and was added to the small ac current. In such setup, the small ac current served as a "fast modulation" to the dc (current) bias and therefore the output of the phase-sensitive detection was proportional to the slope of the $I-V$ characteristic (*i.e.* the differential resistance). dV/dI profile was obtained by continuously varying the dc bias and at the same time measuring the small signal response of the 2DEG. The $I-V$ characteristic and the absolute resistance could be reconstructed by numerical integration during post-data processing. During experiments, the sample was sitting at the bottom of a cryostat at low temperatures. An out-of-plane magnetic field could be applied to the sample which allowed the studies of magnetotransport. Microwave radiation could be sent down to the sample through a rectangular waveguide which allowed observations of MW photoresponse.

2.5 Microwave system

2.5.1 Microwave sources

Gunn oscillators were chosen as our MW sources. One of our Gunn oscillators covers frequency range 27–38 GHz (Ka band) with power output 60–100 mW. The other Gunn

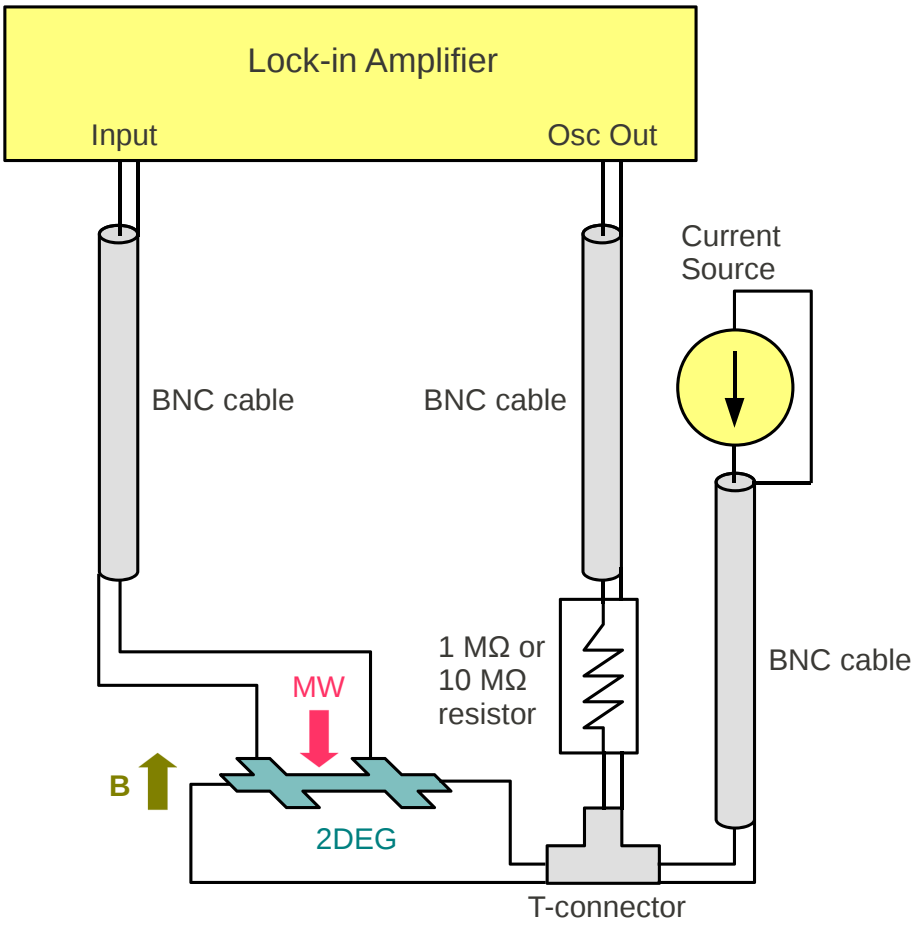

Figure 2.6: Transport measurement setup. We measured linear response resistance and dV/dI profile using this setup.

oscillator covers frequency range 80–110 GHz (W band) with power output 2–8 mW. With a passive frequency doubler on, the low-frequency Gunn oscillator can cover V band (54–76 GHz) with power output 1–3 mW. Frequency tunning is accomplished mechanically by using a micrometer pre-installed on the Gunn resonator. The bias voltage is 5.5 V for the low-frequency Gunn diode and 4.3 V for the high-frequency Gunn diode.

Basically, a Gunn oscillator consists of two components—a Gunn diode and a resonator. An appropriately biased Gunn diode will radiate out electromagnetic wave in the microwave band due to the Gunn effect. The Gunn diode is coupled to a cavity (resonator). The resonant frequency is then determined by the frequency of the microwave generated by the Gunn diode as well as the cavity geometry. Practically, a dielectric or metal screw is inserted into the cavity to allow tuning of one of its dimension. The amount of insertion is usually adjusted by a micrometer.

2.5.2 Microwave transmission

Microwaves are transmitted through rectangular waveguides. To gain control over the microwave power, the output of the Gunn oscillator is fitted into a microwave attenuator. The attenuation can be tuned between 0 and 60 dB with 0.1 dB resolution. Selection of TE_{10} propagation mode is accomplished by employing appropriate waveguide transition between the Gunn oscillator and the attenuator. To connect the high-frequency Gunn oscillator to the attenuator, a WR-10 ($0.100'' \times 0.050''$) to WR-28 ($0.280'' \times 0.140''$) waveguide transition has to be used. To connect the low-frequency Gunn oscillator to the attenuator, only a short WR-28 waveguide is needed. A waveguide transition from WR-15 ($0.148'' \times 0.074''$) to WR-28 is necessary when the frequency doubler is on.

When the cryostat top loading probe is at position, the attenuated microwave can be guided into the probe waveguide through a bend. If two Gunn oscillators are to be used at the same time, a magic tee can be employed to achieve this goal. One of the ports of the magic tee is connected to the top of the probe waveguide and the other two ports are connected to the two attenuators through two short waveguides. In this thesis, however, we will only present the results obtained in 2DEG under monochromatic MW irradiation and will not touch the subject of bichromatic experiments.

Fig. 2.7 schematically shows the waveguide section embedded in the cryostat top loading probe with a magic tee attached to the top. The composite construction of

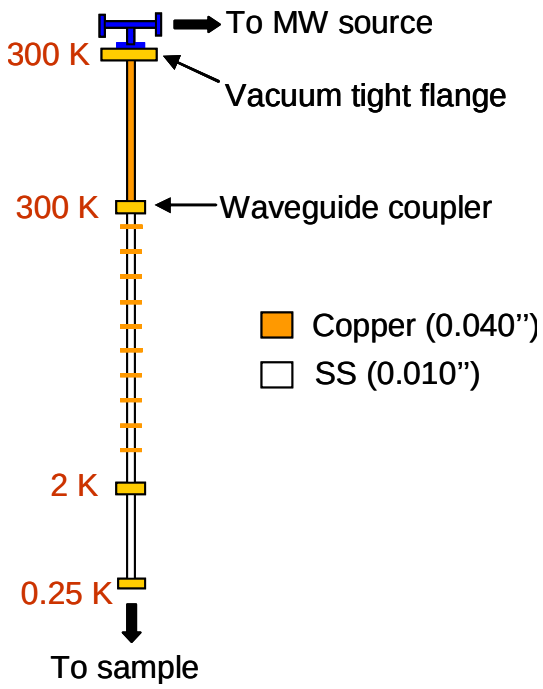

Figure 2.7: Schematic drawing of the waveguide section incorporated in our cryostat top loading probe. The blue piece on the top is a magic tee. It can be replaced by a bend if only one microwave source is to be used. The thickness of the waveguide wall is 0.040″ in the copper section and is 0.010″ in the stainless steel section. The composite construction was designed to minimize heat load and microwave transmission loss. Radiation baffles are to block out thermal radiation from above. The drawing was taken from Ref. [90].

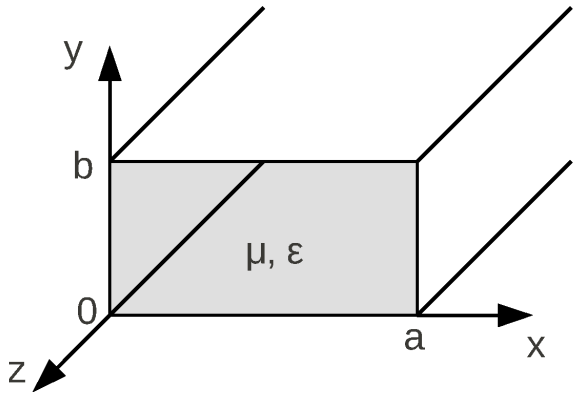

Figure 2.8: A rectangular waveguide with coordinate system setup. z is the propagation direction. The long edge of the cross section is along x-direction and the short edge is along y-direction. If no dielectric material fills the waveguide, $\mu = \mu_0$ and $\epsilon = \epsilon_0$.

the waveguide was designed to minimize the heat load and microwave transmission loss [90][91]. The top $2'$ of the waveguide is made of copper. This part remains at room temperature while the system is running. The rest of the waveguide ($5'$ long) is made of stainless steel (SS). This part is inside the cryostat when the top loading probe is at position. The microwave transmission loss in such a waveguide is estimated as follows. In a rectangular waveguide (cf. Fig. 2.8), the attenuation of TE_{10} mode due to the non-ideal waveguide walls is given as [92]:

$$\begin{aligned}
\alpha_c &= \frac{2R_s}{b\eta'\sqrt{1-(f_{c10}/f)^2}}\left[\frac{1}{2}+\frac{b}{a}\left(\frac{f_{c10}}{f}\right)^2\right] \\
R_s &= \sqrt{\frac{\pi f \mu}{\sigma}} \\
\eta' &= \sqrt{\frac{\mu}{\epsilon}} \\
f_{c10} &= \frac{1}{2a\sqrt{\mu\epsilon}}
\end{aligned} \tag{2.1}$$

a (b) is the long (short) dimension in the waveguide cross section, f_{c10} is the cutoff frequency of the TE_{10} mode, f is the microwave frequency, R_s and σ are the surface resistivity and electrical conductivity of the waveguide walls respectively, η' is the intrinsic impedance of the dielectric material (if there is any) that fills the waveguide.

Our waveguide is hollow, so $\mu = \mu_0$ and $\epsilon = \epsilon_0$. We thus have $\eta' \approx 376.7\,\Omega$ and

$f_{c10} \approx 21.077\,\text{GHz}$ for a WR-28 waveguide (with $a = 0.280''$ and $b = 0.140''$). We looked up the values of σ for copper and stainless steel from Ref. [93]:

- At $T = 293\,\text{K}$
  - Cu: $\sigma \approx 5.8 \times 10^7\,\text{S/m}$
  - SS: $\sigma \approx 1.1 \times 10^6\,\text{S/m}$
- At $T = 4\,\text{K}$
  - Cu: $\sigma \approx 5.0 \times 10^{10}\,\text{S/m}$
  - SS: $\sigma \approx 3.1 \times 10^6\,\text{S/m}$

Here, σ of stainless steel at $4\,\text{K}$ was estimated using Wiedemann-Franz law ($\kappa \approx 0.3\,\text{W/m}\cdot\text{K}$ at $4\,\text{K}$). Fig. 2.9 shows the attenuation coefficients (α_c) of copper and stainless-steel waveguides at both $293\,\text{K}$ and $4\,\text{K}$ as a function of microwave frequency. As the cutoff frequency is approached, the attenuation increases rapidly.

To proceed, let us pick a microwave frequency, say, $f = 60\,\text{GHz}$. The attenuation coefficients at this frequency are

- At $T = 293\,\text{K}$
  - Cu: $\alpha_c \approx 0.5\,\text{dB/m}$
  - SS: $\alpha_c \approx 3.61\,\text{dB/m}$
- At $T = 4\,\text{K}$
  - Cu: $\alpha_c \approx 0.017\,\text{dB/m}$
  - SS: $\alpha_c \approx 2.16\,\text{dB/m}$

During system operation, there is a temperature gradient in the stainless-steel section. The largest temperature gradient occurs in the upper part of the stainless-steel section [91]. Since we only intend to make a rough estimation here, let us assume that the whole stainless-steel section is at $4\,\text{K}$. Given the attenuation coefficients, we estimated that the power loss is roughly $3\,\%$ in the $2'$-long copper section (at room temperature) and is close to $38\,\%$ in the $5'$-long stainless-steel section (at $4\,\text{K}$). Microwave propagating

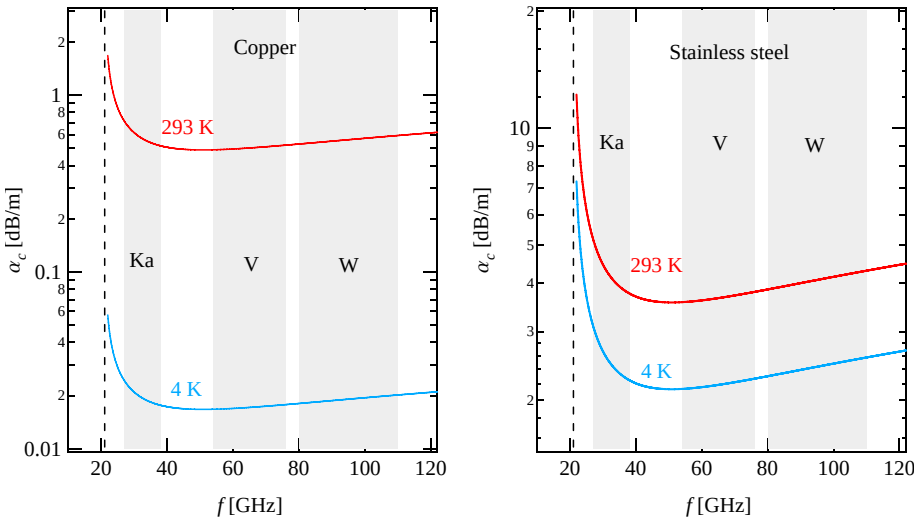

Figure 2.9: Attenuation coefficients calculated using Eq. (2.1) for the frequency range covered by our Gunn oscillators. The transmission loss in a stainless-steel waveguide is significantly higher than that in a copper waveguide. Transmission loss becomes infinite at the waveguide cutoff frequency.

from the top of the copper section all the way down to the bottom of the stainless-steel section thus suffers about 40 % of power loss.

For the rectangular waveguide depicted in Fig. 2.8, the nonzero field components for TE_{10} mode over the waveguide cross section are given as [92]:

$$\begin{aligned} E_y &\propto -i \sin \frac{\pi x}{a} \\ H_x &\propto i \sin \frac{\pi x}{a} \\ H_z &\propto \cos \frac{\pi x}{a} \end{aligned} \tag{2.2}$$

The field strength (E_y and H_x only) over the wave guide cross section is shown in Fig. 2.10. The sample is positioned in such a way that the Hall bar bridge lies completely in the region confined by the box (2 mm × 2 mm in dimensions) (cf. Fig. 2.10). The field strength at the left and right boundaries of the box is roughly 90 % of its maximum value.

The fields impinging on the sample will partially get transmitted and partially get reflected due to the transition in dielectric constant. We estimated the relative strength

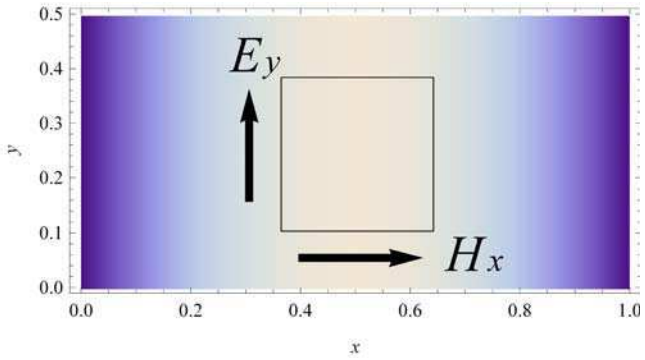

Figure 2.10: The distribution of fields over a cross section of a rectangular waveguide calculated using Eq. (2.2). Only E_y and H_x are shown. They are both strongest in the middle and decay to zero toward left and right edges. The box (2 mm × 2 mm) near the center defined the region where the Hall bar bridge was situated. The electric field drops to about 90 % of its maximum value at the left and right edges of the box.

of the electric field transmitted into the GaAs layer as [94]:

$$\frac{E_0'}{E_0} = \frac{2}{\sqrt{\frac{\mu\epsilon'}{\mu'\epsilon}} + 1} \tag{2.3}$$

E_0 is the impinging field and E_0' is the transmitted field. μ and ϵ are the vacuum values in our case. μ' and ϵ' are the values in GaAs. Using the dielectric constant of GaAs at 4 K ($\epsilon_r \approx 12.9$), we estimated that $E_0'/E_0 \approx 0.44$.

2.6 Cryogenic system

Our cryogenic system is an Oxford HelioxTL top-loading ^{3}He refrigerator. Samples are mounted onto the top-loading probe and are inserted into liquid ^{3}He during experiments. Operation temperatures at ≈ 1.5 K are readily maintained by pumping on 1 K pot (which contains liquid ^{4}He drawn from the main ^{4}He bath) above the ^{3}He pot (where the samples are immersed in). By reducing the ^{3}He vapor pressure in the ^{3}He pot, samples can be cooled to temperatures below 1 K. With the help of a sorption pump (which is integrated in the cryostat insert), temperatures down to 250 mK can be achieved when experimental heat load is sufficiently low. By using a pre-installed heater in proximity to the samples, experiments can be performed at temperatures higher than 4.2 K. The

temperature at the sorption pump is monitored by a carbon (Allen-Bradley) resistor. RuO_2 sensors are fitted on the 1 K pot and the ^{3}He pot for sensing temperatures below 7 K. For higher temperatures (up to 300 K), the temperatures at the ^{3}He pot is monitored using a Cernox sensor instead. Magnetic field along the cryostat axis is provided by a superconducting magnet. The maximum central magnetic field produced by its main coil is about 10 T at 4.2 K and is about 12 T at 2.2 K. Magnetic field-dependent thermometry errors $|\Delta T|/T\,(\%)$ at 2.5 T are given below [95][96]:

Table 2.1: Thermometry errors at 2.5 T

sensor type	T (K)	$\lvert\Delta T\rvert/T\,(\%)$
Allen-Bradley	20	< 1
RuO_2	2	1.4
Cernox	2	1.3

Chapter 3

2DEG under dc excitation

3.1 Introduction

The dc-current induced nonlinearity in the longitudinal resistivity was first observed by Yang *et al.* in a high-mobility 2DEG [97]. Fig. 3.1 shows their original data. To increase sensitivity, differential resistance (r) was measured instead of absolute resistance (R). The analysis by Yang *et al.* showed that $\partial r/\partial B$ exhibited $1/B$ periodicity. This new oscillation in magnetoresistivity persisted to $\approx 4\,\mathrm{K}$ without being smeared out by elevated temperatures. Yang *et al.* proposed that Zener tunneling between Hall-field tilted Landau levels could be the mechanism behind this new phenomenon. An attempt to develop a rigorous theory along this line was made by Lei [98]. Further experimental investigation on this subject was carried out a few years later by A. A. Bykov *et al.* [99]. They confirmed Yang *et al.*'s assertion that $\partial r/\partial B$ was periodic in $1/B$. In addition to the $1/B$-periodic oscillations in magnetoresistivity, dc-current induced suppression of longitudinal resistivity was observed [100][101]. This phenomenon was linked to the dc-current induced non-equilibrium electron energy distribution [100]. A theory which encompasses both phenomenons was developed by Vavilov *et al.* within the framework of standard Boltzmann equation [102]. In this chapter, we present our experimental data as well as numerical simulations on this subject.

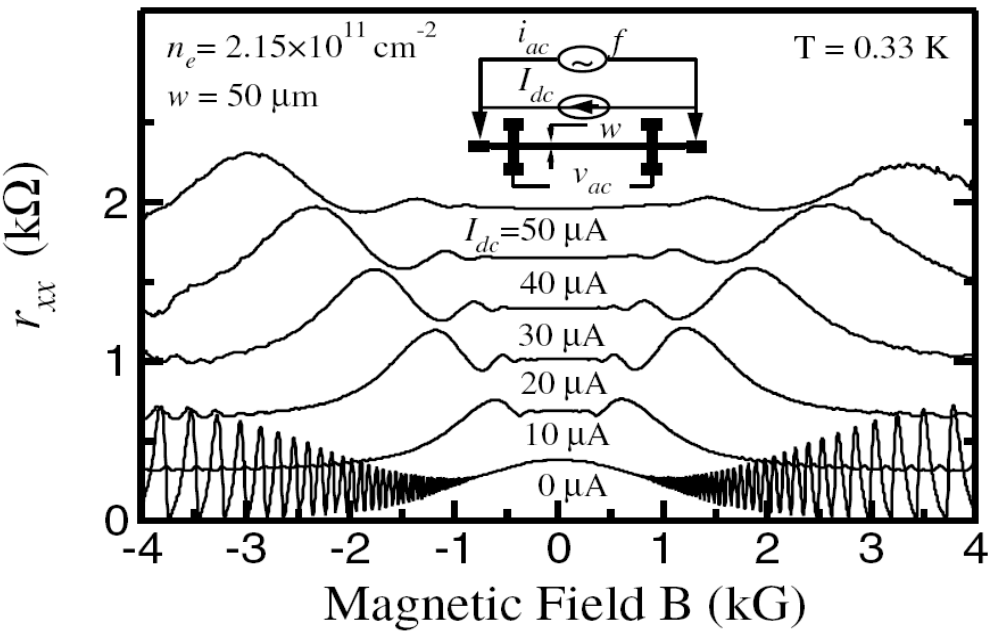

Figure 3.1: First observation of HIRO in a high-mobility 2DEG. From Ref. [97].

3.2 Experimental results

The experiments were performed at constant coolant temperature $T \simeq 1.5\,\mathrm{K}$. Before taking measurements, the sample was briefly illuminated with visible light. Differential resistivity r was measured while sweeping B (the out-of-plane magnetic field) at a constant I (the applied dc-current) as well as while sweeping I at a constant B. Fig. 3.2(a) plots r vs B at $I = 80\,\mu\mathrm{A}$. The numbers (1, 2, 3, 4) in the graph label the HIRO peaks. Up to the fifth-order of HIRO peaks was resolved in this sample. It was previously discovered that the peaks of these oscillations occur whenever the following condition is satisfied: $l\Delta Y = \gamma R_\mathrm{c}$ (here $\Delta Y = \hbar\omega_\mathrm{c}/eE_H$ with E_H being the Hall electric field, $l = 1, 2, 3, \ldots$, and $\gamma \simeq 2$) [97]. This condition states that a geometrical resonance occurs whenever the cyclotron diameter matches an integral multiple of the spatial separation between adjacent Landau levels. This spatial separation (ΔY) is the direct consequence of the spatial gradient of energy levels created by Hall electric field (E_H). We took this concept one step further and mapped the two length scales (ΔY and γR_c) onto two associated energy scales: $\hbar\omega_\mathrm{H}\,(\equiv \gamma e E_H R_\mathrm{c})$ and $\hbar\omega_\mathrm{c}$. The energy scale $\hbar\omega_\mathrm{H}$ is the work

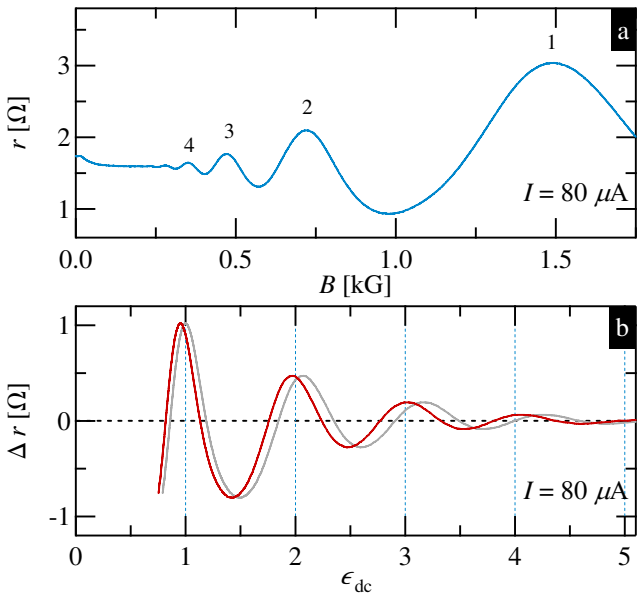

Figure 3.2: (a) r vs B at $I = 80\,\mu$A. (b) Δr extracted from (a) plotted against $\epsilon_{\rm dc}$. Red (gray) curves are plotted using $\gamma = 1.9$ (2.0).

associated with the Hall electric field across the cyclotron diameter. For a given sample (with a certain carrier density n_e and a certain Hall-bar width w), $\hbar\omega_{\rm H}$ is simply tuned by the applied dc-current: $\hbar\omega_{\rm H} = \gamma\hbar(2\pi/n_e)^{1/2}I/ew$ with γ being a fitting parameter. We defined $\epsilon_{\rm dc} \equiv \omega_{\rm H}/\omega_{\rm c}$ which serves as a natural parameter for a dc-driven 2DEG. Phenomenologically, we consider dc-current induced correction to differential resistivity as: $\Delta r \equiv r(I \neq 0) - r(I = 0)$. Fig. 3.2(b) plots Δr vs $\epsilon_{\rm dc}$ for the data shown in Fig. 3.2(a). The red and gray curves were plotted using different values of γ ($\gamma = 1.9$ for the red curves and $\gamma = 2.0$ for the gray curves). With $\gamma = 1.9$, the peaks (troughs) of Δr hit the integer (half-integer) $\epsilon_{\rm dc}$ fairly nicely. With $\gamma = 2.0$, however, the peaks (troughs) gradually drift away from the integer (half-integer) values as $\epsilon_{\rm dc}$ increases. In contrast to previous observations, our data shows $1/B$-periodicity in r itself instead of in $\partial r/\partial B$.

In Fig. 3.2(a)(b), the amplitudes of oscillations diminish rapidly with decreasing B. The decay is governed by the Dingle factor $\delta = \exp(-\pi/\omega_{\rm c}\tau_{\rm q})$. Therefore, it is difficult to resolve higher order resonances by sweeping B at a fixed I. Since the parameter relevant to the dc-driven 2DEG is $\epsilon_{\rm dc}$, which is proportional to I/B, a very simple solution to

this problem is simply performing I-sweep at a fixed B instead of performing B-sweep at a fixed I. The only concern regarding I-sweep being that Joule heating might be an issue when I is sufficiently large. Practically, we only stayed at low B and so increasing I up to a few hundreds micro-Amp is sufficient to resolve enough higher order resonances for our analysis purposes. Generally speaking, Joule heating in our samples at this level of dc-currents did not cause drift of lattice temperature.

Fig. 3.3 presents I-sweep data at two different B: (a) 416 G; (b) 732 G. As we did in Fig. 3.2(b), Δr was plotted against $\epsilon_{\rm dc}$ using both $\gamma = 1.9$ (the red curves) and $\gamma = 2.0$ (the gray curves). The positions of the resonant peaks drift with increasing $\epsilon_{\rm dc}$ when we assumed $\gamma = 2.0$ just like what is demonstrated in Fig. 3.2(b). The amplitudes of the oscillations decay slower than the data obtained from B-sweeps (cf. Fig. 3.2(b)). Nevertheless, the decay is still evident. So far, no theoretical investigation regarding HIROs has taken such behavior into account. We constructed the Dingle plot using the I-sweep data at eight different B values (cf. Fig. 3.3(c)). The solid red (open blue) circles correspond to the first four maxima (minima) of Δr. The slope of the lines give us $\tau_{\rm q} \simeq 20\,{\rm ps}$ which is consistent with the decay shown in Fig. 3.2.

We now focus our attention on the regime of small dc-current. Fig. 3.4(a) compares differential magnetoresistivity at zero dc-current to that at a finite dc-current $I = 20\,\mu{\rm A}$. The vertical downward arrow in the graph indicates the position of the HIRO peak at $\epsilon_{\rm dc} = 1$. On the right side of this first order peak (where $\epsilon_{\rm dc} < 1$), r is significantly reduced compared to the linear response resistivity (*i.e.* at zero dc-current). Fig. 3.4(b) presents Δr extracted from I-sweep data at different fixed B values ($0.75 \sim 1.75\,{\rm kG}$ in steps of $0.25\,{\rm kG}$). The first minimum gets deeper and also moves to lower $\epsilon_{\rm dc}$ values as B increases. The physics behind this observation is more transparent when one looks at absolute resistivity. Fig. 3.4(c) is the normalized absolute resistivity numerically reconstructed using the data in Fig. 3.4(b). At $B = 1.75\,{\rm kG}$, the absolute resistivity is reduced by a factor of 5 at the first minimum. The width of the zero-bias peak decreases with increasing B and it appears to saturate at sufficiently high B. These observations can be qualitatively understood by comparing the Landau-level width in real space (ΔY) to the cyclotron diameter ($2R_{\rm c}$). Theoretically, it has been shown that electrical transport in a dc-driven 2DEG is governed by electron backscattering from impurity. Whenever an electron undergoes backscattering, its guiding center (the center

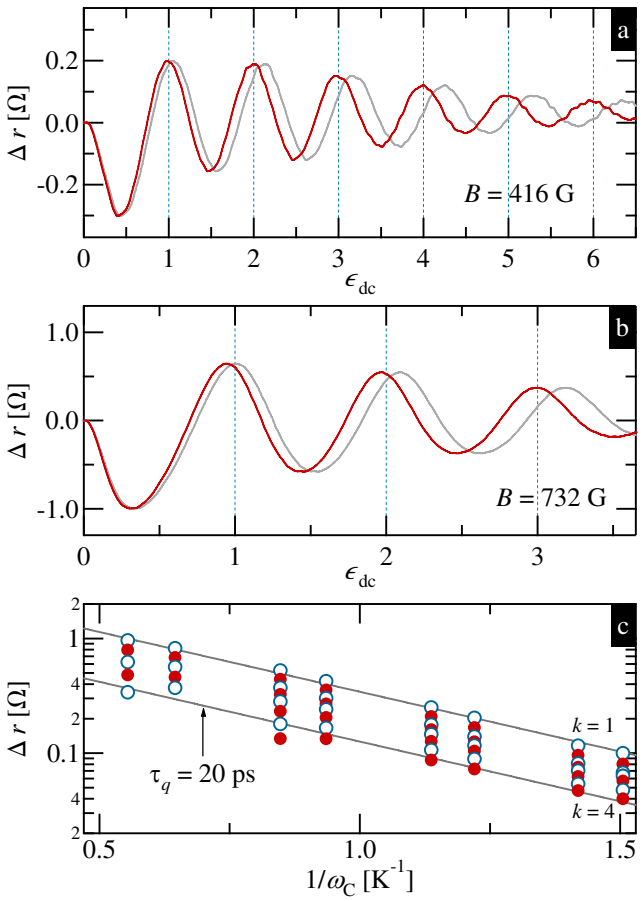

Figure 3.3: I-sweep data taken at (a) $B = 416\,\mathrm{G}$ and (b) $B = 732\,\mathrm{G}$. The red (gray) curves were plotted using $\gamma = 1.9\,(2.0)$. (c)The Dingle plot constructed using the first four maxima (solid red) and the first four minima (open blue) of Δr. The gray lines correspond to $\tau_{\mathrm{q}} \simeq 20\,\mathrm{ps}$.

of its cyclotron orbit) shifts (or hops) by $2R_c$. At a fixed B, the "hopping distance" is fixed. Increasing dc-current increases Hall electric field and that in turn reduces ΔY. As ΔY decreases, the chance for an electron to undergo $2R_c$-hopping within a Landau-level also decreases. The decrease of available scattering channels results in the dramatic reduction of resistivity at small dc-current. The vertical dashed line in Fig. 3.4(c) marks the crossover point where $2R_c = 2\Gamma/eE_H$ (here $2\Gamma = \hbar/\tau_q$ being the full width of a Landau level and $2\Gamma/eE_H$ being its spatial width). This scenario is pictorially shown in Fig. 3.5(a). The position of this vertical line roughly corresponds to the half-width of the zero-bias peak. Looking at Fig. 3.4(d), we see that the first minimum gets deeper and wider as B gets stronger. The minimum gets wider because Landau-level spacing increases as B increases. The middle point of the troughs remain roughly centered at $\epsilon_{dc} \simeq 1/2$ regardless of B. This is a region where $2\Gamma/eE_H \lesssim 2R_c \lesssim \Delta Y - 2\Gamma/eE_H$, *i.e.*, the chances that an electron can undergo either $2R_c$-hopping within a Landau level or between adjacent Landau levels are both restricted. Fig. 3.5(b) depicts such situations. When Hall electric field is further increased, electrons would ultimately be able to hop to the next higher Landau level and the resistivity starts to rise again due to the open-up of the scattering channels.

3.3 Numerical results

According to the theory developed by Vavilov *et al.* [102], the nonlinearity in electrical transport in a dc-driven 2DEG originates from two sources: 1.) formation of non-equilibrium electron energy distribution; 2.) modulation of electron scattering rates by the Hall electric field (E_H). At small E_H, the first mechanism dominates. It results in the sharp drop of resistivity at low dc-current. As E_H increases, electron energy distribution gets smoothed out and the second mechanism takes over. This reflects on the oscillation in differential resistivity with the dc-current.

The curves generated using Vavilov *et al.*'s theory are plotted in Fig. 3.6 for three different B (416 G, 732 G, and 1.75 kG) and two different χ (0.04 and 0.01). The physical parameters that are required to generate these curves include τ_q, τ_{tr}, τ_{in}, χ, B and T. $\tau_q \simeq 20$ ps and $\tau_{tr} \simeq 435$ ps are extracted from experimental data. τ_{in} is the energy

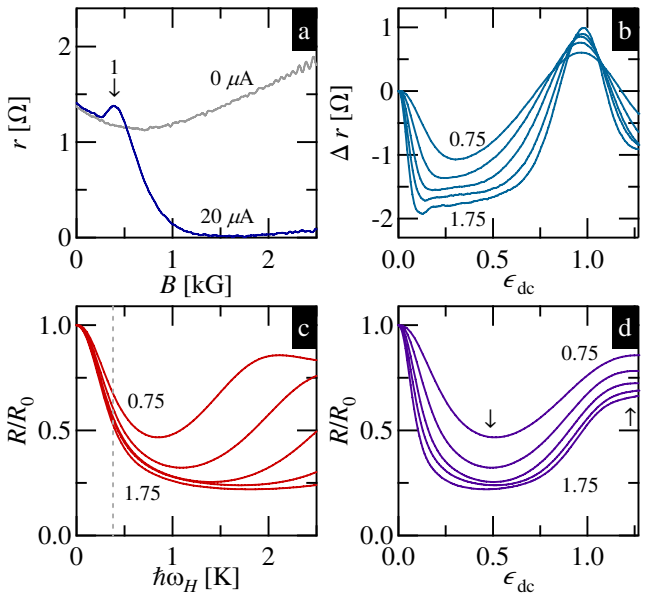

Figure 3.4: (a) Dramatic suppression of differential magnetoresistivity due to a finite dc-current $I = 20\,\mu$A. (b) Δr extracted from I-sweeps at different B (from 0.75 to 1.75 kG in steps of 0.25 kG). (c) Normalized absolute resistivity reconstructed from the data in (b). The vertical dashed line corresponds to a Landau-level width $2\Gamma = \hbar/\tau_{\rm q} = 380$ mK. (d) The vertical downward arrow marks the first minimum at $\epsilon_{\rm dc} \simeq 1/2$ and the vertical upward arrow marks the first maximum at $\epsilon_{\rm dc} \simeq 5/4$.

relaxation time and it is estimated as [60]:

$$\tau_{\rm in} \simeq 0.822\tau_{\rm ee}(0,T)$$
$$\frac{\hbar}{\tau_{\rm ee}(\varepsilon,T)} = \frac{\varepsilon^2+\pi^2k_B^2T^2}{4\pi\varepsilon_{\rm F}}\ln\frac{\kappa v_{\rm F}}{\max\left[k_BT/\hbar,\omega_{\rm c}\sqrt{\omega_{\rm c}\tau_{\rm tr}}\right]} \tag{3.1}$$

$\tau_{\rm ee}^{-1}$ is the electron-electron scattering rate and $\kappa = 4\pi k_{\rm e}e^2\nu_0$ ($\simeq 2.4\times10^9\,{\rm m}^{-1}$) is the inverse screening length ($k_{\rm e}$ being the Coulomb constant and $\nu_0 = m^*/2\pi\hbar^2$ being the DoS at $B = 0$ per spin degree of freedom). Using Eq. (3.1), we estimate that (at $T = 1.5$ K) $\tau_{\rm in} \simeq 86$ ps at $B = 416$ G; 98 ps at 732 G; 126 ps at 1.75 kG. χ is a dimensionless parameter determined by the ratio of Fermi wavelength $\lambda_{\rm F}$ to the correlation length of the disorder potential. It can be estimated in two different ways: 1.) $\chi = (\lambda_{\rm F}/2\pi d)^2$

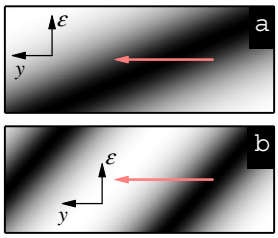

Figure 3.5: An electrons undergoes $2R_c$-hopping in a dc-driven 2DEG. The left-pointed arrows denote the $2R_c$-hopping. Laudau levels (dark stripes) are tilted by the Hall electric field. (a) $2R_c = 2\Gamma/eE_H$ (b) $2R_c \simeq \Delta Y/2$

(where d is the spacer width) [72]; 2.) using the following relations [71]:

$$\begin{aligned}
\frac{1}{\tau_q} &= \frac{1}{\tau_{sh}} + \frac{1}{\tau_{sm}} \\
\frac{1}{\tau_{tr}} &= \frac{1}{\tau_{sh}} + \frac{1}{\tau_{sm}} \frac{\chi}{1+\chi} \\
\frac{1}{\tau_\pi} &= \frac{1}{\tau_{sh}} + \frac{1}{\tau_{sm}} \frac{2\pi}{\sqrt{\chi}} \exp\left(-\frac{\pi}{\sqrt{\chi}}\right)
\end{aligned} \tag{3.2}$$

τ_{sh}^{-1} (τ_{sm}^{-1}) is the scattering rate associated with the short (long) -range disorder and τ_π^{-1} is electron backscattering rate. τ_π can be extracted from the amplitudes of Hall-field induced resistivity oscillations based on the following expression [71]:

$$\frac{\Delta r}{r_0} = \frac{16\delta^2 \tau_{tr}}{\pi \tau_\pi} \cos(2\pi\epsilon_{dc}), \quad \pi\epsilon_{dc} \gg 1 \tag{3.3}$$

By constructing the Dingle plot, it was found that $\tau_{tr}/\tau_\pi \simeq 0.18$ [103]. With all the information in our hands, Eq. (3.2) can then be solved numerically. The χ value we obtain from the first approach is ≈ 0.01 and that from the second approach is ≈ 0.04.

Comparing the theoretical curves with the experimental data (cf. Fig. 3.3(a)(b)), it's clear that the set of curves generated using $\chi = 0.01$ more closely resembles the actual data. With $\chi = 0.04$, the $\epsilon_{dc} \simeq 1$ peak is depressed substantially compared to higher other peaks. This apparently is not what the experimental data shows. The red curve ($B = 416\,\mathrm{G}$) and the blue curve ($B = 732\,\mathrm{G}$) in Fig. (3.6)(b) ($\chi = 0.01$), on the other hand, do reasonably capture most of the features of the actual data including the amplitude and the phase of the oscillations. The main difference being that the

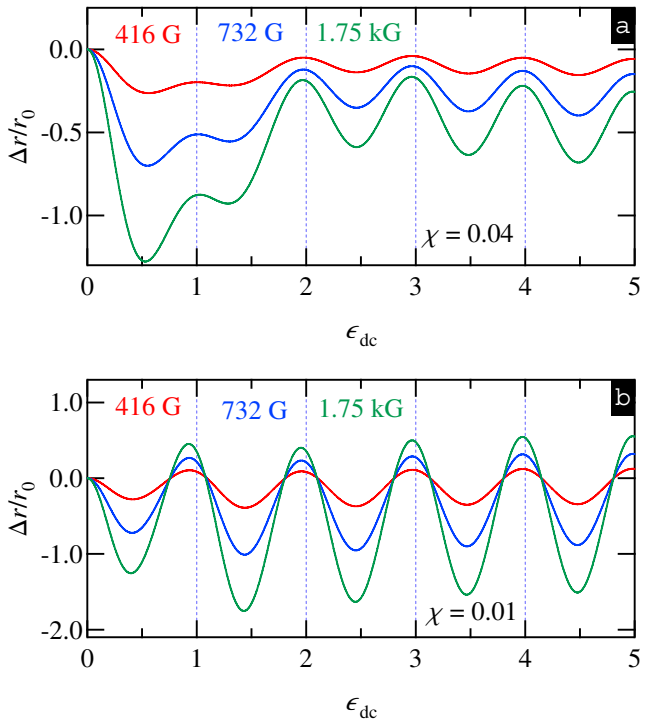

Figure 3.6: Theoretical curves generated using the theory developed by Vavilov *et al.*. Physical parameters corresponding to the experiments are used. (a) $\chi = 0.04$ (b) $\chi = 0.01$

theoretical curves do not show decay of oscillations with increasing $\epsilon_{\rm dc}$ (or the dc-current). It was hypothesized by Vavilov *et al.* that the decay might come from heating which results in $\tau_{\rm q}$ (which enters the Dingle factor δ) drifting with the dc-current. This is still an open question.

Since Vavilov *et al.*'s theory assumes that Landau levels are overlapped, it is expected that more significant deviations between the theory and the experiments would emerge at higher B when Landau levels are well-separated. This can be seen by comparing the green curve in Fig. 3.6(b) with the bottom trace in Fig. 3.4(b) ($B = 1.75\,$kG). In addition to a narrower zero-bias peak, the actual data develops a basin-shape trough at $\epsilon_{\rm dc} < 1$ which does not reproduce by the theory. To see how separation of Landau levels affects the theoretical results, we performed numerical computation following the formalisms in Ref. [102]. The dissipative current density (which is parallel to E_H) can

be calculated as:

$$\begin{aligned} j_d &= 2ev_{\mathrm{F}} \int_0^{\infty} d\varepsilon \nu(\varepsilon) \int_0^{2\pi} \cos\varphi f(\varepsilon,\varphi) \frac{d\varphi}{2\pi} \\ &= 2ev_{\mathrm{F}} \int_0^{\infty} d\varepsilon \nu(\varepsilon) \int_0^{2\pi} \sin\varphi \left(-\frac{\partial f(\varepsilon,\varphi)}{\partial \varphi} \right) \frac{d\varphi}{2\pi} \end{aligned} \tag{3.4}$$

$\nu(\varepsilon)$ is the DoS. φ is the angle the electron momentum makes with E_H before scattering. $f(\varepsilon,\varphi)$ is the electron energy distribution. Ignoring energy relaxation, $f(\varepsilon,\varphi)$ needs to satisfies the following equation:

$$\begin{aligned} -\frac{\partial f(\varepsilon,\varphi)}{\partial \varphi} &= \frac{1}{\omega_{\mathrm{c}}} \int_0^{2\pi} \frac{\nu(\varepsilon + W_{\varphi\varphi'})}{\nu_0} \frac{f(\varepsilon + W_{\varphi\varphi'}, \varphi') - f(\varepsilon,\varphi)}{\tau(\varphi - \varphi')} \frac{d\varphi'}{2\pi} \\ W_{\varphi\varphi'} &= eE_H R_{\mathrm{c}} (\sin\varphi' - \sin\varphi) \end{aligned} \tag{3.5}$$

$W_{\varphi\varphi'}$ is the work associated with E_H in the course of guiding center displacement. φ' is the angle the electron momentum makes with E_H after scattering. $\tau(\varphi - \varphi')^{-1}$ is the elastic scattering rate in the absence of electric and magnetic fields. It can be expanded in harmonics τ_n^{-1} and is modeled for mixed disorder as

$$\begin{aligned} \frac{1}{\tau(\varphi - \varphi')} &= \sum_{n=-\infty}^{+\infty} \frac{e^{in(\varphi - \varphi')}}{\tau_n}, \quad \tau_n = \tau_{-n} \\ \frac{1}{\tau_n} &= \frac{1}{\tau_{\mathrm{sm}}} \frac{1}{1 + \chi n^2} + \frac{\delta_{n,0}}{\tau_{\mathrm{sh}}}, \quad \chi \ll 1 \end{aligned} \tag{3.6}$$

$\delta_{n,0}$ is the Kronecker delta. Differential resistivity is calculated as

$$\begin{aligned} r &= \frac{\partial[\rho_{\mathrm{H}} j_d(j)]}{\partial j} = \rho_{\mathrm{H}}^2 \frac{\partial j_d(E_H)}{\partial E_H} \\ \rho_{\mathrm{H}} &= \frac{B}{e n_{\mathrm{e}}} \\ E_H &= \rho_{\mathrm{H}} j \end{aligned} \tag{3.7}$$

ρ_{H} is the Hall resistivity and j is the applied dc-current density.

Within the lowest-order approximation, Eq. (3.5) can be solved by replacing the $f(\varepsilon,\varphi)$ that appears under the integral sign by the Fermi-Dirac distribution function. An expression which allows us to compute j_d is obtained by combining Eq. (3.4) and

Eq. (3.5). The DoS is modeled as

$$\begin{aligned}
\nu(\varepsilon) &= \frac{2eB}{h}\sum_{n=0}^{+\infty}\frac{1}{\sqrt{2\pi}\Gamma}\exp\left[-\frac{(\varepsilon-\varepsilon_n)}{2\Gamma^2}\right] \\
\varepsilon_n &= \left(n+\frac{1}{2}\right)\hbar\omega_{\mathrm{c}}, \quad n=0,1,2,3,\ldots \\
\Gamma &= \hbar\sqrt{\frac{eB}{2\pi m^*\tau_{\mathrm{q}}}}
\end{aligned} \tag{3.8}$$

The pre-factor $2eB/h$ is the Landau-level degeneracy (ignoring Zeeman splitting). 2Γ is the full width of a Landau level at the -2.17 dB point (*i.e.* at $\approx 60.6\,\%$ the peak value). It turns out that the integrand in this form is highly oscillatory and so it's difficult to get any convergent numerical results out of it. The problem was overcome by replacing the $\sin\varphi$ (cf. the second line in Eq. (3.4)) with $(\sin\varphi - \sin\varphi')/2$. It can be shown analytically that this substitution gives exactly the same result. The benefit for doing so being that the integrand becomes more well-behaved and the convergent numerical results can be obtained. Monte Carlo strategy was employed to speed up numerical integration. The noise introduced in the process was subsequently reduced by a Savitzky-Golay smoothing filter. The numerical results are presented in Fig. 3.7 for both $\chi = 0.01$ (a) and $\chi = 0.04$ (b). The numerical results for $\chi = 0.04$ bear little similarity to Fig. (3.4)(b). The set of curves for $\chi = 0.01$, however, qualitatively resemble the actual data. The basin-shape valley indeed is developed at higher B (cf. the 1.75 kG trace). The zero-bias peak gets narrower and appears to saturate at sufficiently high B which are also consistent with the experimental data. The widths of the zero-bias peaks are not quantitatively captured by these numerical results. This suggests that the separation of Landau levels (which is not considered in Vavilov *et al.*'s theory) itself is not sufficient to produce the sharp drop in longitudinal resistivity at small dc-current. To numerically reproduce the observed width of the zero-bias peak in the regime of separated Landau levels, the energy relaxation term will also need to be taken into account.

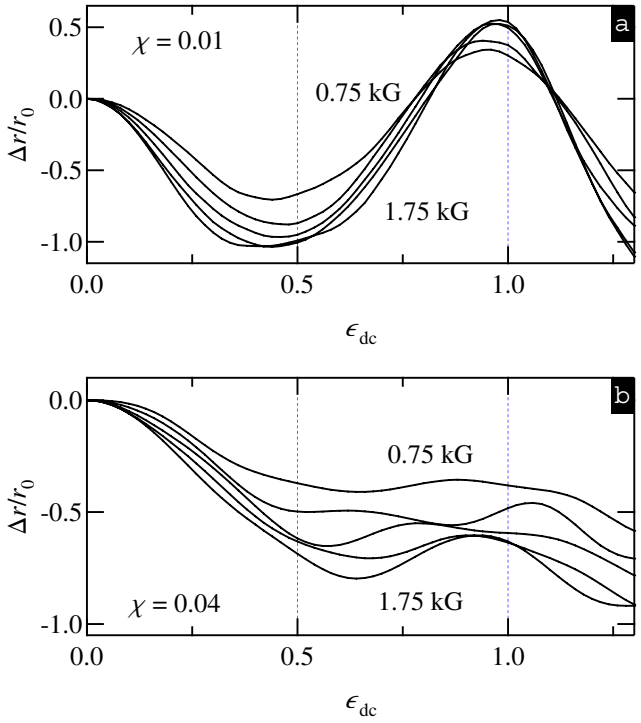

Figure 3.7: Numerical simulation of the nonlinearity in electrical transport induced by a small dc-current. B increases from 0.75 kG to 1.75 kG in steps of 0.25 kG. Landau levels are modeled by a series of Gaussian functions. (a) $\chi = 0.01$ (b) $\chi = 0.04$

3.4 Summary

Under a weak out-of-plane magnetic field, a high-mobility 2DEG driven by a dc-current exhibits nonlinearity in its electrical transport. Oscillations in the longitudinal differential resistivity were observed as the dc-current was continuously varied. At very low dc-current, longitudinal resistivity was dramatic suppressed. Vavilov *et al.* developed a theory within the framework of the standard Boltzmann equation. The low ϵ_{dc} nonlinearity is attributed to the formation of non-equilibrium electron energy distribution. The oscillations in differential resistivity, on the other hand, originates from Hall-field modulated electron scattering rate. The mechanism behind the decay of HIRO with increasing dc-current is still unknown.

Chapter 4

Zero-differential resistance state in a dc-driven 2DEG

4.1 Introduction

Zero-differential resistance state (ZdRS) in a dc-driven 2DEG has been previously observed in the regime where Shubnikov-de Haas oscillations (SdHOs) occur [104][5][105] as well as in the regime where microwave-induced resistance oscillations (MIROs) emerge [106]. In the first case, it was observed that the harmonic content of SdHOs changes with the applied dc-current. The small-signal response measured at a magnetic field corresponding to a SdHO peak was suppressed by the dc-current and was reduced to zero above some threshold current $I_{\rm th}$. In the second case, similar phenomenon occurred in a MW-irradiated 2DEG. When a dc-current was applied, it was observed that a MIRO peak can evolve into a ZdRS. In this chapter, we present our observation of a ZdRS which emerges from a minimum of Hall-field induced resistance oscillations (HIROs) [107][108]. The physical mechanism behind the experimental observation will be explained based on the model of current domains [51].

4.2 Experimental results

Fig. 4.1 presents differential magnetoresistivty measured at $T = 1.5\,\mathrm{K}$ for two different dc-currents: (a) $I = 10\,\mu\mathrm{A}$ and (b) $I = 20\,\mu\mathrm{A}$. For comparison, the linear response

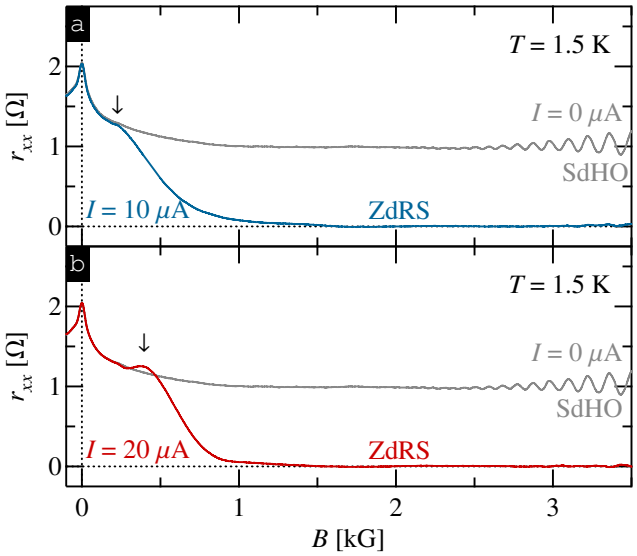

Figure 4.1: Differential magnetoresistivity measured at (a) $I = 10\,\mu$A and (b) $I = 20\mu$A. Together plotted is the linear response magnetoresistivity (*i.e.* at $I = 0$).

resistivity (*i.e.* at $I = 0$) is also plotted. The linear response resistivity shows a fairly pronounced negative magnetoresistivity at very low B followed by a flat portion before the onset of SdHOs at $B \simeq 2.5\,$kG. The data with a finite dc-current also shows the same negative magnetoresistivity at very low B. It has been suggested that the observed negative magnetoresistivity could arise from classical localization (see, for instance, Ref. [109]). Since it is beyond the scope of this chapter, we will not further discuss it here. At B higher than this classical localization regime, the nonlinearity induced by the applied dc-current starts to emerge. The shoulder/peak indicated by the downward arrows in Fig. 4.1(a)(b) mark the $\epsilon_{\rm dc} \simeq 1$ HIRO peaks. On the right side of this peak (where $\epsilon_{\rm dc} < 1$), differential resistivity is strongly suppressed by the dc-current. The mechanism behind this phenomenon is linked to the formation of non-equilibrium electron energy distribution which has been discussed in Chapter 3. Remarkably, as B continues to increase, the differential resistivity can be depressed all the way to zero. This ZdRS even penetrates into the regime where SdHOs starts to be observed when there is no dc-current.

In contrast to the ZdRS reported previously, this "new" ZdRS does not rely on MW irradiation; nor is it related to SdHOs. The ZdRS emerges from the maxima of

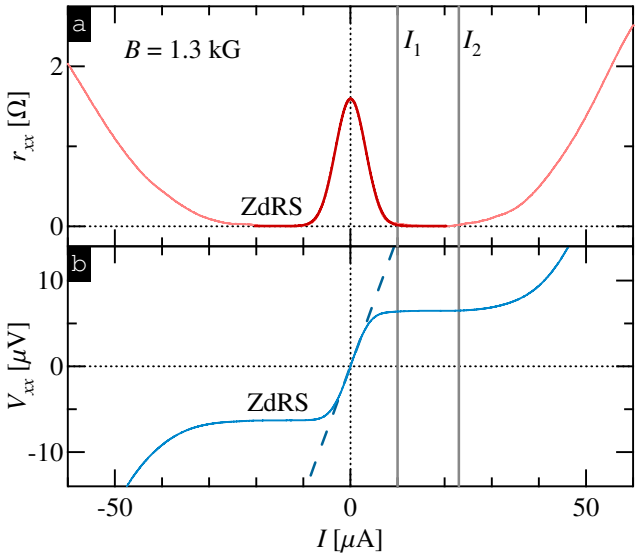

Figure 4.2: (a) Differential resistivity measured at $B = 1.3\,\mathrm{kG}$ and $T = 1.5\,\mathrm{K}$. The two vertical lines bound the I range where the ZdRS appears. The dark red curve is the Gaussian fit described in the text. (b) The I-V curve numerically reconstructed using the data in (a). Ohm's law is plotted as the dashed line.

SdHOs only occurs within small and discontinuous intervals of B. The "new" ZdRS sets in at a magnetic field much lower than the onset of SdHOs and it extends over a substantial and continuous range of B. Moreover, the formation of this "new" ZdRS is not accompanied by a precursor negative spike or any temporal resistivity oscillations previously reported in Ref. [104].

To investigate the range of dc-current within which the ZdRS can be sustained, we turn to I-sweeps at fixed B. Fig. 4.2(a) presents such data measured at $B = 1.3\,\mathrm{kG}$ and $T = 1.5\,\mathrm{K}$. A ZdRS develops after a initial sharp drop of differential resistivity. Differential resistivity stays at zero over a finite range (between $I_1 \simeq 10\,\mu\mathrm{A}$ and $I_2 \simeq 23\,\mu\mathrm{A}$) and rises again when $I > I_2$. The zero-bias peak can be nicely fitted with a Gaussian function: $r_{xx}(I) = r_{xx}(0)\exp(-I^2/\Delta_1^2)$. $r_{xx}(0)$ is the linear response resistivity and Δ_1 characterizes the width of the zero-bias peak. We estimate the ZdRS onset dc-current as $I_1 \simeq 2\Delta_1$. Such a fit is also shown in Fig. 4.2(a) (between $-20\,\mu\mathrm{A}$ and $+20\,\mu\mathrm{A}$, the dark red curve). We obtain $\Delta_1 \simeq 4.5\,\mu\mathrm{A}$ from this fit.

Fig. 4.2(b) is the I-V characteristic obtained by numerical integration using the

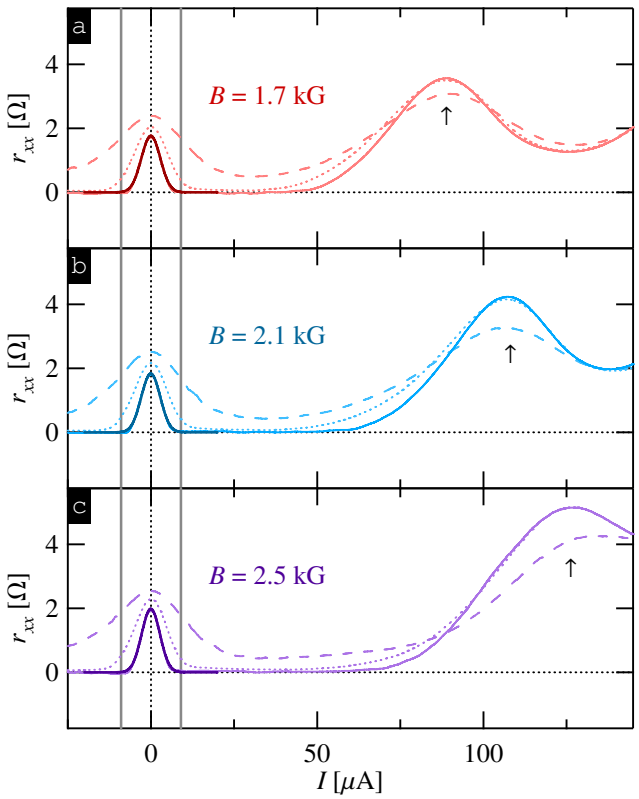

Figure 4.3: Differential resistivity measured at three different B: (a) 1.7 kG; (b) 2.1 kG; (c) 2.5 kG and three different T: 1.5 K (solid curves); 2.0 K (dotted curves); 3.0 K (dashed curves). The two vertical lines bound the zero-bias peaks. $\epsilon_{\rm dc} \simeq 1$ peaks are indicated by the upward arrows.

data in Fig. 4.2(a). A plateau in longitudinal voltage V_{xx} develops following an initial rising phase. V_{xx} stays at a constant value within the B interval in which ZdRS shows. Together plotted is the I-V relation dictated by Ohm's law (the dashed line). At very low dc-current, the I-V characteristic follows Ohm's law fairly closely. As I increases, nonlinearity emerges. When $I > I_2$, V_{xx} starts to increase again due to the enhancement of inter-Landau level scattering.

Elevated temperature could destroy ZdRS. This is shown in Fig. 4.3 for three different B: (a) 1.7 kG; (b) 2.1 kG; (c) 2.5 kG. At $T = 1.5$ K (the solid lines), ZdRS are well-developed for all three B. At $T = 2.0$ K (the dotted lines), the range of dc-current which is able to sustain a ZdRS shrinks significantly. At $T = 3.0$ K (the dashed lines),

ZdRS are completely gone. The temperature broadening of the zero-bias peak and the destruction of ZdRS by elevated temperature might be related to the enhancement of energy relaxation through electron-electron collisions. Stronger energy relaxation could result in a smoother electron energy distribution and therefore reduces the nonlinearity. So far, temperature dependence has not been considered in any theoretical work dealing with dc-driven 2DEG [102][98].

Examining Fig. 4.3, we see that both $r_{xx}(0)$ and the onset current (I_1) of ZdRS are insensitive to B. Since the longitudinal voltage V_{xx} at ZdRS is equal to half the area below the zero-bias peak, it too is only weakly dependent on B. For the data taken at $T = 1.5\,\mathrm{K}$, we fit the zero-bias peaks with Gaussian functions. These fits are shown as the dark curves in Fig. 4.3. We obtained $\Delta_1 \simeq 4.0\,\mu\mathrm{A}$ from these fits. This value is slightly lower than what we get from fitting the $B = 1.3\,\mathrm{kG}$ data. At $B \lesssim 1\,\mathrm{kG}$, ZdRS does not develop in our sample. This might be attributed to the fact that the modulation in the DoS decreases as B gets weaker and as a result reduces the modulation in electron energy distribution.

The range of I which can sustain ZdRS increases with increasing B. ZdRS is destroyed when inter-Landau level scattering starts to set in. The maximum dc-current I_2 for ZdRS to exist at a certain B is therefore closely related to the position of the $\epsilon_{\mathrm{dc}} \simeq 1$ HIRO peak (indicated by the upward arrows in Fig 4.3). The $\epsilon_{\mathrm{dc}} \simeq 1$ peak occurs at $I_H = j_H w \simeq e n_{\mathrm{e}}(\omega_{\mathrm{c}}/2k_{\mathrm{F}}) \propto B$ (where $k_{\mathrm{F}} = \sqrt{2\pi n_{\mathrm{e}}}$). Thus, I_2 increases as B gets stronger. We find that the $\epsilon_{\mathrm{dc}} \simeq 1$ peaks can also be fitted reasonably well with Gaussian functions: $r_{xx}(I) = r_{xx}(I_H)\exp[-(I-I_H)^2/\Delta_2^2]$. The fitting result shows that $\Delta_2 \simeq 18 \sim 22\,\mu\mathrm{A}$ which is only weakly dependent on B. We estimate the upper critical current of ZdRS as $I_2 \simeq I_H - 2\Delta_2$.

Our experimental observations are summarized in Fig. 4.4. The Δ_1 and $I_H - \Delta_2$ obtained from fitting experimental data are plotted as red solid squares and blue solid circles, respectively. Together plotted are the positions ($I_H(B)$) of the $\epsilon_{\mathrm{dc}} \simeq 1$ peaks. The shaded area roughly bounded by the solid squares and the solid circles indicates the region (in the I-B space) where ZdRS appears.

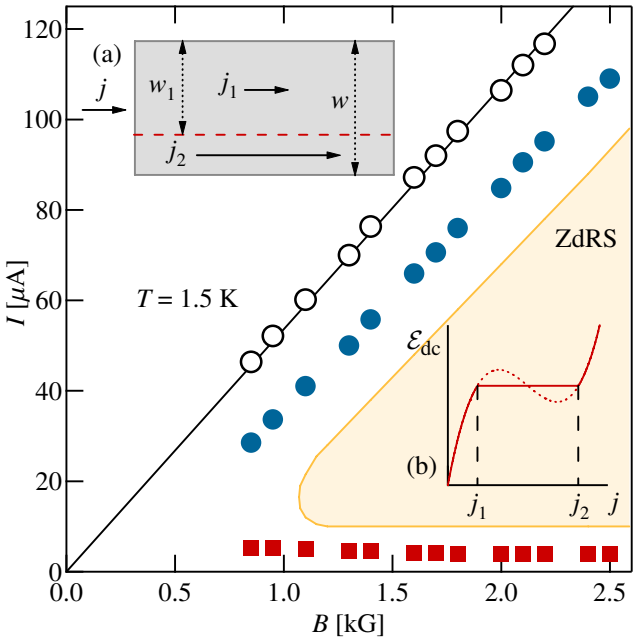

Figure 4.4: Summary of our experimental observations. ZdRS is formed in the shaded region roughly bounded by the red solid squares (Δ_1) and blue solid circles ($I_H - \Delta_2$). Open black circles are the positions ($I_H(B)$) of the $\epsilon_{\rm dc} \simeq 1$ peaks.

4.3 Phenomenological explanation of ZdRS

It was suggested by Bykov *et al.* that the ZdRS observed in a dc-driven 2DEG could be understood phenomenologically in terms of the formation of current domains [104]. This idea, however, is by no means new. It is actually borrowed from a current-domain model originally proposed by Andreev *et al.* for explaining the MW-induced zero-resistance states (ZRS) [51][110][111]. Bykov *et al.* postulate a generic N-shaped local E_x-j_x characteristic as depicted in inset (b) of Fig. 4.4. It can be shown that the system is unstable unless the following conditions hold:

$$\begin{aligned} \rho_{xx}(\vec{j_x}^2) &= \frac{E_x}{j_x} \geq 0 \\ r_{xx}(\vec{j_x}^2) &= \frac{\partial E_x}{\partial j_x} \geq 0 \end{aligned} \tag{4.1}$$

ρ_{xx} (r_{xx}) is the absolute (differential) resistivity. The first condition is apparently always true for the postulated E_x-j_x characteristic. The second condition immediately tells us

that the local current density cannot assume any values between the two critical points (where the slope becomes negative). Since E_x has to be continuous across the domain wall (cf. inset (a) of Fig. 4.4), the local current density within each domain cannot be arbitrary. They can only assume the values corresponding to the same longitudinal electric field. The clamped field is determined by an "equal-area rule" which dictates that the areas bounded by the E_x-j_x characteristic above and below the clamped field (represented by a horizontal line segment in inset (b) of Fig. 4.4) have to equal to each other [104]. The lower and upper critical current density (j_1 and j_2) for ZdRS are simply the two current densities corresponding to the clamped field.

Inset (a) of Fig. 4.4 depicts the simplest pattern in which only two current domains exist in the 2DEG. By adjusting the position of the domain wall, any applied current density j between j_1 and j_2 can be accommodated:

$$\begin{aligned} jw &= j_1 w_1 + j_2(w - w_1) \\ \Rightarrow \frac{w_1}{w} &= \frac{j_2 - j}{j_1 - j_2} \end{aligned} \tag{4.2}$$

For our sample at $B = 1.5\,\mathrm{kG}$, we estimate that $I_1 \simeq 10\,\mu\mathrm{A}$ and $I_2 \simeq 43\,\mu\mathrm{A}$. With an input dc-current $I = 20\,\mu\mathrm{A}$, the domain wall would be adjusted such that $w_1/w \simeq 0.7$.

Since the Hall electric field is discontinuous across the domain wall (because $j_1 \neq j_2$), space charge must accumulate around the domain wall. Due to the $\vec{E} \times \vec{B}$ drift, the domain wall would not be stationary and will propagate across the Hall bar. It has been suggested that the periodic creation and annihilation of domain wall should result in current pulses with repetition rate roughly equal to inverse the transit time of the domain wall [104]. Experimentally, it's not been verified yet.

4.4 Summary

We observed a new ZdRS in a dc-driven 2DEG. It emerges from a minimum of HIROs. This ZdRS extends over a substantial and continuous range of magnetic field. We identify the lower and upper critical currents for the formation of this ZdRS. According to the simplest current-domain model, these two critical currents are associated with the two allowed local current densities corresponding to the clamped longitudinal field.

Chapter 5

2DEG under simultaneous ac and dc excitations

5.1 Introduction

The study of electrical transport in 2DEG under simultaneous MW irradiation and a dc-current bias is motivated by a current-domain model put forth by Andreev *et al.* [51]. So far, direct detection of current domains has not been achieved. According to the model, Microwave-induced zero-resistance state (ZRS) cannot exist above certain critical current density. If this critical current density could be identified in experiments, it will provide stronger evidence to the formation of current domains while ZRS is formed. In this chapter, we present our experimental effort along this line [112].

5.2 Experimental results

Previously, Zhang *et al.* have discovered that the resonance peaks in the small-signal response of a high-mobility 2DEG under simultaneous MW irradiation and a dc-current bias could roughly be described by the following empirical rule [106]:

$$\epsilon_{\rm dc} + \epsilon_{\rm ac} \simeq n, \quad n = 1, 2, 3, \ldots \tag{5.1}$$

As we will show in a moment, Eq. (5.1) is not complete. A closer examination of the data revealed another resonance condition. We will discuss what these resonance conditions

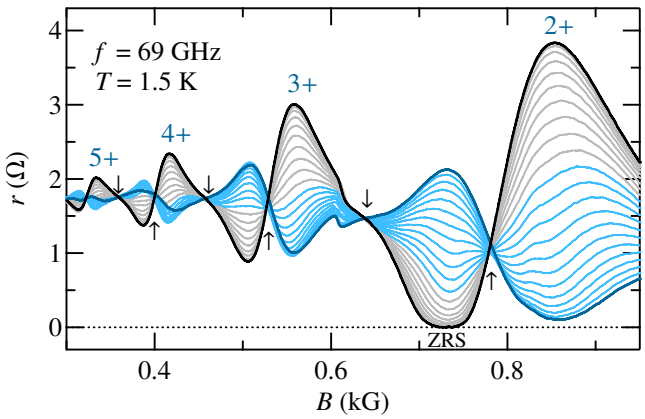

Figure 5.1: Differential magnetoresistivity measured at different dc-current bias from $I = 0$ (black curve) to $I = 22\,\mu$A (dark blue curve) in steps of $2\,\mu$A. The numbers (2+, 3+, 4+, 5+) label MIRO peaks and the arrows mark nodes which were only weakly affected by I.

mean.

The experiments were performed at constant coolant temperature $T \simeq 1.5\,$K under continuous MW irradiation. The data we are going to present was taken at MW frequency $f = 69\,$GHz at maximum available power. All the other frequencies showed similar results. Fig. 5.1 presents differential magnetoresistivity at different dc-current bias (from $I = 0$ to $I = 22\,\mu$A in $2\,\mu$A steps). Several MIRO peaks and a well-developed ZRS were observed at $I = 0$ (cf. the thick black curve). As I increased, MIRO peaks evolved into troughs and vice versa. A series of nodes which were only weakly affected by I were also observed.

To have a closer look at the data, we plotted it in a different way. Fig. 5.2(a) presents r vs $\epsilon_{\rm dc}$ at different $\epsilon_{\rm ac}$ (from $\epsilon_{\rm ac} = 2$ to $\epsilon_{\rm ac} = 3.5$ in steps of 0.05). Since MW frequency was fixed, each curve corresponds to a certain magnetic field. B decreases from bottom (smaller $\epsilon_{\rm ac}$) to top (larger $\epsilon_{\rm ac}$). I increases from left to right (because $\epsilon_{\rm dc} \propto I/B$). The first thing we immediately notice is that the amplitude of r depends on $\epsilon_{\rm ac}$ in a non-monotonic way. At $\epsilon_{\rm ac} \simeq n \pm 1/4$, it has the largest amplitude. r appears to be featureless at $\epsilon_{\rm ac} \simeq n + 1/2$. The amplitudes for different $\epsilon_{\rm ac}$ at $\epsilon_{\rm dc} \lesssim 1$ were extracted. The result is shown in Fig. 5.2(b). It confirms the observation we made in Fig. 5.2(a).

At integer $\epsilon_{\rm ac}$, r essentially takes the form of HIROs (cf. $\epsilon_{\rm ac} = 2,\ 3$). At $\epsilon_{\rm ac} \simeq n \pm 1/4$,

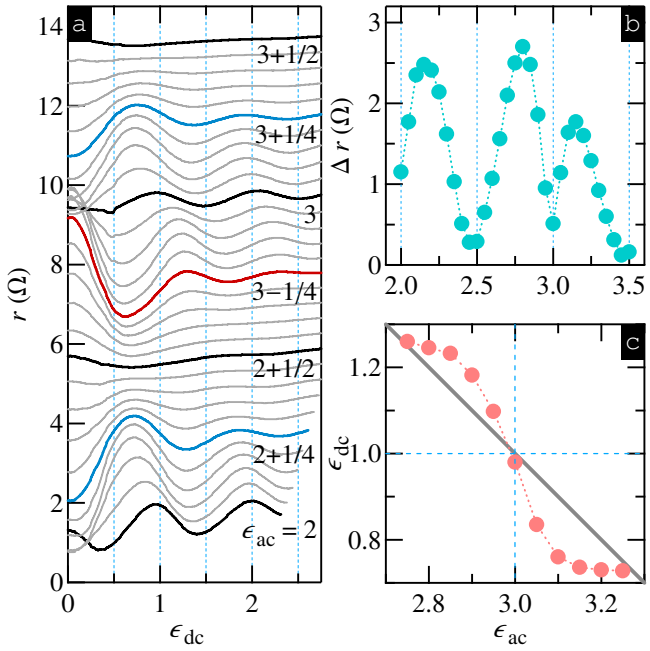

Figure 5.2: (a) r vs ϵ_{dc} at different ϵ_{ac} (from $\epsilon_{ac} = 2$ to $\epsilon_{ac} = 3.5$ in steps of 0.05). For clarity, the traces are vertically offset in increments of $0.4\,\Omega$. (b) The amplitudes at $\epsilon_{dc} \lesssim 1$ extracted from (a) for different ϵ_{ac}. (c) Positions of the resonance peaks at around $(\epsilon_{ac}, \epsilon_{dc}) = (3, 1)$. The straight line is predicted by Eq. (5.1).

r shifted in opposite directions along ϵ_{dc}-axis by about 1/4 of the period relative to HIROs (cf. $\epsilon_{ac} = 3 - 1/4$ and $\epsilon_{ac} = 3 + 1/4$). This observation is consistent with Eq. (5.1). Systematic deviation from Eq. (5.1) occurs at the intermediate values of ϵ_{ac} (e.g. $3 \lesssim \epsilon_{ac} \lesssim 3 + 1/4$). To demonstrate this point, we traced the position of the resonance peak at $(\epsilon_{ac}, \epsilon_{dc}) \simeq (3, 1)$ as ϵ_{ac} is varied. The result is plotted in Fig 5.2(c). The solid circles are the experimental data and the slope line is predicted by Eq. (5.1). They only agree with each other at the end points ($\epsilon_{ac} = 3 - 1/4,\ 3 + 1/4$) and the middle point ($\epsilon_{ac} = 3$).

To facilitate visualizing our data, we created gray-scale maps. Fig. 5.3(a) presents r at around $(\epsilon_{ac}, \epsilon_{dc}) = (3, 1)$. Light patches correspond to the resonance peaks and the dark ones correspond to the troughs. Their positions (peaks $(\epsilon_{ac}, \epsilon_{dc})^+$; troughs

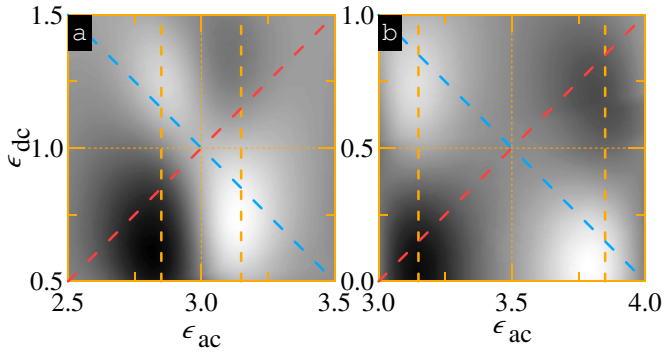

Figure 5.3: (a) r map at around $(\epsilon_{ac}, \epsilon_{dc}) = (3, 1)$. (b) r map at around $(\epsilon_{ac}, \epsilon_{dc}) = (7/2, 1/2)$. The blue$^+$ (red$^-$) dashed lines correspond to $\epsilon_{ac} \pm \epsilon_{dc} = n$. The yellow vertical dashed lines pass through resonance peaks and troughs.

$(\epsilon_{ac}, \epsilon_{dc})^-$) could be roughly described by

$$\begin{aligned} (\epsilon_{ac}, \epsilon_{dc})^+ &\simeq (n \pm 1/4, m \mp 1/4) \\ (\epsilon_{ac}, \epsilon_{dc})^- &\simeq (n \pm 1/4, m \pm 1/4) \end{aligned} \tag{5.2}$$

From the first line of Eq. (5.2), we obtain the complete set of resonance conditions:

$$\begin{aligned} \epsilon_{ac} + \epsilon_{dc} &\simeq n \\ \epsilon_{ac} - \epsilon_{dc} &\simeq m - 1/2 \end{aligned} \tag{5.3}$$

Fig. 5.3(b) presents the gray-scale map of r at around $(\epsilon_{ac}, \epsilon_{dc}) = (7/2, 1/2)$. The overall landscape looks similar to that at around $(\epsilon_{ac}, \epsilon_{dc}) = (3, 1)$. The main difference being that both the light and dark patches are closer to the image center in Fig. 5.3(a) than in Fig. 5.3(b). This is because the MIRO phase in this case ($\simeq 0.15$) is smaller than the theoretical prediction ($\simeq 1/4$).

The physical significance of Eq. (5.3) will become more transparent in a moment. Very briefly, the first (second) condition is associated with absorption (emission) of MW quanta by current carrying electrons. The pictorial illustrations of these two processes are presented in Fig. 5.4 for $(\epsilon_{ac}, \epsilon_{dc}) = (3 - 1/4, 1 + 1/4)$. The scenario depicted in (a) would result in increasing of resistivity (due to the vast amount of available states existing at the center of a Landau band which electrons can be scattered into). The scenario depicted in (b), on the other hand, would result in decreasing of resistivity

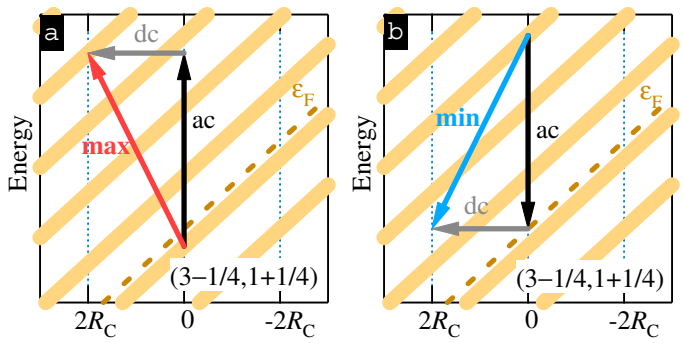

Figure 5.4: Illustrations of characteristic electron transitions at $(\epsilon_{\rm ac}, \epsilon_{\rm dc}) = (3-1/4, 1+1/4)$. Thick slope lines (yellow) represent Hall-field tilted Landau bands. Vertical arrows (black) represent absorption/emission of a MW quantum. Horizontal arrows (gray) represent electron backscattering ($2R_{\rm c}$-hopping). The combined result is depicted as the slanted arrows (red or blue). (a) An electron absorbing a MW quantum. (b) An electron emitting a MW quantum.

(due to limited available states in the gaps). As we will see in a moment, the observed differential resistivity is (roughly speaking) the difference between these two contributions. For the example depicted in Fig. 5.4, it's a positive contribution minus a negative contribution. This results in a peak in r.

5.3 Theoretical predictions

Extensive theoretical work about nonlinear transport in 2DEG under simultaneous ac and dc excitations has been carried out by Khodas *et al.* [71]. They derived that

$$\frac{r-r_{\rm D}}{r_{\rm D}} = \frac{(4\delta)^2\tau_{\rm tr}}{\pi\tau_\pi}\left[\cos 2\pi\epsilon_{\rm dc} J_0(4\sqrt{\mathcal{P}_\omega}\sin\pi\epsilon_{\rm ac}) - \frac{2\epsilon_{\rm ac}}{\epsilon_{\rm dc}}\sin 2\pi\epsilon_{\rm dc}\cos\pi\epsilon_{\rm ac}\sqrt{\mathcal{P}_\omega}J_1(4\sqrt{\mathcal{P}_\omega}\sin\pi\epsilon_{\rm ac})\right] \tag{5.4}$$

$r_{\rm D} = (e^2\nu_0 v_{\rm F}^2\tau_{\rm tr})^{-1}$ is the Drude resistivity and $\mathcal{P}_\omega$ is a dimensionless parameter proportional to MW power. Strictly speaking, Eq. (5.4) is only valid when $\epsilon_{\rm dc}$ is sufficiently large. It leaves out the contribution from MW-induced non-equilibrium electron energy distribution which is believed to be important when $\epsilon_{\rm dc}$ is small. Nevertheless, we found that Eq. (5.4) generally provides fairly reasonable (at least) qualitative predictions

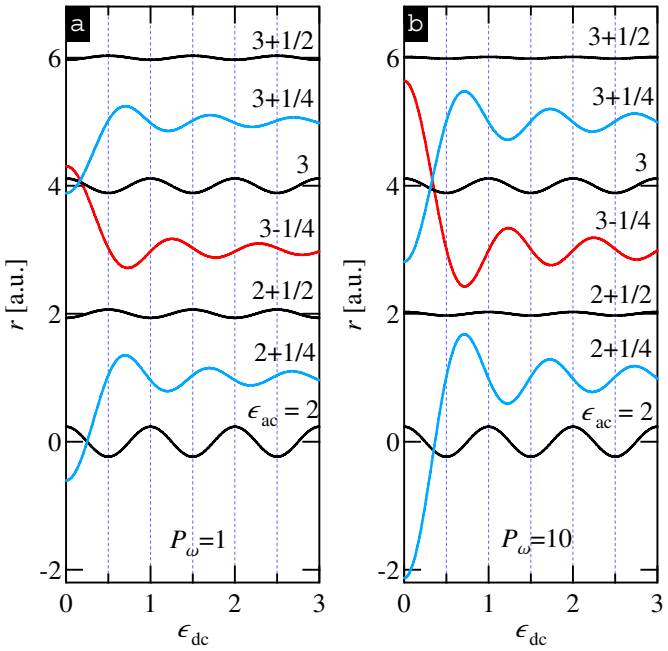

Figure 5.5: Theoretical r vs $\epsilon_{\rm dc}$ generated using Eq. (5.4) for different $\epsilon_{\rm ac}$ at $\mathcal{P}_\omega = 1$ (a) and $\mathcal{P}_\omega = 10$ (b).

to what we have observed in experiments. The theoretical predictions are plotted in Fig. 5.5 for $\mathcal{P}_\omega = 1$ (a) and $\mathcal{P}_\omega = 10$ (b). Comparing theoretical curves to experimental data (cf. Fig. 5.2(a)), we notice the striking resemblance between the two.

The theoretical curves show that the oscillations in r at $\epsilon_{\rm ac} = n + 1/2$ and $\epsilon_{\rm ac} = n$ are out-of-phase (in-phase) when $\mathcal{P}_\omega = 1$ ($\mathcal{P}_\omega = 10$). Since the experimental data is almost completely featureless at $\epsilon_{\rm ac} = n + 1/2$, it's relatively hard to tell which case (out-of-phase or in-phase) reflects the reality. Despite its surprising success, Eq. (5.4) is not particularly transparent in physics. Let us look at its asymptotic form in the limit of low MW power ($\mathcal{P}_\omega \ll 1$):

$$\frac{r - r_{\rm D}}{r_{\rm D}} \simeq \frac{(4\delta)^2 \tau_{\rm tr}}{\pi \tau_\pi} \Bigg[(1 - 2\mathcal{P}_\omega) \cos 2\pi\epsilon_{\rm dc} + 2\mathcal{P}_\omega \left(\cos 2\pi\epsilon_{\rm dc} \cos 2\pi\epsilon_{\rm ac} - \frac{\epsilon_{\rm ac}}{\epsilon_{\rm dc}} \sin 2\pi\epsilon_{\rm dc} \sin 2\pi\epsilon_{\rm ac} \right) \Bigg] \tag{5.5}$$

It's straightforward to show that Eq. (5.5) can be cast into the following form:

$$\begin{aligned}\frac{r-r_{\rm D}}{r_{\rm D}} \simeq \frac{(4\delta)^2\tau_{\rm tr}}{\pi\tau_\pi}\Bigg[&(1-2\mathcal{P}_\omega)\cos 2\pi\epsilon_{\rm dc}\\ &+\frac{\mathcal{P}_\omega}{\epsilon_{\rm dc}}(\epsilon_{\rm ac}+\epsilon_{\rm dc})\cos 2\pi(\epsilon_{\rm ac}+\epsilon_{\rm dc})\\ &-\frac{\mathcal{P}_\omega}{\epsilon_{\rm dc}}(\epsilon_{\rm ac}-\epsilon_{\rm dc})\cos 2\pi(\epsilon_{\rm ac}-\epsilon_{\rm dc})\Bigg]\end{aligned} \tag{5.6}$$

The first term in Eq. (5.6) comes from "virtual" processes involving electrons interacting with MW fields. These processes are not accompanied by actually absorbing/emitting MW quanta. The second (third) term comes from "real" processes in which electrons actually absorb (emit) MW quanta.

At this point, it becomes clear that the empirical rule (cf. Eq. (5.3)) we obtained earlier is directly related to electrons absorbing/emitting MW quanta. If only "real" processes are taken into account, it can be shown that

$$\begin{aligned}&(\epsilon_{\rm ac},\epsilon_{\rm dc})^+ \simeq (m/2, m/2) \text{ or } (m\pm 1/4, n\mp 1/4)\\ &(\epsilon_{\rm ac},\epsilon_{\rm dc})^- \simeq (m\pm 1/4, n\pm 1/4)\\ &(\epsilon_{\rm ac},\epsilon_{\rm dc})^s \simeq (m/2, n/2) \text{ with } m\neq n\end{aligned} \tag{5.7}$$

$(\epsilon_{\rm ac},\epsilon_{\rm dc})^s$ denotes the saddle point. m, n are positive integers. The first line of Eq. (5.7) reproduces the empirical resonance conditions (cf. Eq. (5.3)). The second and third lines reasonably predict the troughs and saddle points in Fig. 5.3. The effect of "virtual" processes on Eq. (5.7) is to move resonance peaks (troughs) slightly toward (away from) integer $\epsilon_{\rm dc}$.

The non-monotonic evolution in r with changing $\epsilon_{\rm ac}$ is the consequence of different degrees of cancellation/enhancement between "virtual" and "real" processes. The miraculous partial cancellation between them at integer $\epsilon_{\rm ac}$ completely nullifies the effect of MW irradiation and results in pure HIROs. The suppression of oscillations at half-integer $\epsilon_{\rm ac}$ can be understood from Eq. (5.4). At half-integer $\epsilon_{\rm ac}$, it is reduced to the following form:

$$\frac{r-r_{\rm D}}{r_{\rm D}} = \frac{(4\delta)^2\tau_{\rm tr}}{\pi\tau_\pi} J_0(4\sqrt{\mathcal{P}_\omega})\cos 2\pi\epsilon_{\rm dc} \tag{5.8}$$

This is a HIRO-like oscillation with its amplitude modulated by a MW-power dependent factor. Since $J_0(4\sqrt{\mathcal{P}_\omega})$ decays away as $\mathcal{P}_\omega$ increases, r becomes practically featureless.

Depending on the actual MW power, the oscillation could be either in-phase or out-of-phase with HIROs.

5.4 Summary

We studied the nonlinear transport in a high-mobility 2DEG under simultaneous ac and dc excitations. We found a complete set of resonance conditions in differential resistivity. Theoretical work by Khodas *et al.* suggests that the non-monotonic behavior in r is the manifestation of cancellation/enhancement between processes involving "virtual" and "real" processes.

Chapter 6

Nonlinear transport at the second subharmonic of CR

6.1 Introduction

In addition to the MIROs occurring at around integral multiples of cyclotron resonance (CR), similar phenomenon has also been observed near fractional values of $\hbar\omega_c$. MIRO-like features at around $\epsilon_{ac} = 1/2,\ 3/2,\ 5/2,\ 1/3,\ 2/3$ have be reported [3][50][113][114]. These "fractional MIROs" were originally explained by a multi-photon displacement mechanism [115]. Later, it was argued that in the regime of separated Landau levels, an inelastic multi-photon mechanism dominates [116]. At the crossover from separated to overlapped Landau levels, two single-photon inelastic mechanisms become important. The first mechanism arises from a resonant series of consecutive single-photon transitions [117]. The second mechanism is linked to the MW-induced sidebands in the DoS [116]. In this chapter, we present our experimental observation on the electrical transport at $\epsilon_{ac} = 1/2$. [118]. We observed that the differential resistivity at $\epsilon_{ac} = 1/2$ oscillates with twice the frequency (in terms of ϵ_{dc}) compared to that at $\epsilon_{ac} = 1$. By performing numerical simulations, we found that this "frequency-doubling" phenomenon could be understood within the theoretical work put forth by Khodas *et al.* [71].

6.2 Experimental results

Our experiments were performed at constant coolant temperature $T \simeq 1.5\,\mathrm{K}$. The 2DEG was under continuous MW irradiation at $f = 27\,\mathrm{GHz}$. Differential magnetoresistivity was measured at various dc-current bias. Fig. 6.1 presents the experimental data. The $I = 0$ trace clearly shows pairs of resonance peak and trough occurring at around B corresponding to integer $(1, 2, 3)$ and fractional $(1/2, 1/3)$ values of ϵ_{ac}. The signal is the strongest at CR. The strength of the signal diminishes very quickly as we move towards the higher order harmonics of CR. Similar situation also occurs at the subharmonics of CR, but the signal strength appears to decay much slower.

As we have discussed in Chapter 5, a dc-current can turn a MIRO peak into a trough and vice versa. Such evolution goes on with the applied dc-current in a periodic fashion. For instance, the MIRO peak (at $I = 0$) just below the CR evolved into a trough at $I \simeq 20\,\mu\mathrm{A}$. As we increased I, this trough became a peak again at $I \simeq 40\,\mu\mathrm{A}$. Similar peak-to-trough/trough-to-peak evolutions were also observed near harmonics and subharmonics of CR.

Based on the resonance conditions Eq. (5.3), the influence of a dc-current on a MW-irradiated 2DEG is through the dimensionless parameter ϵ_{dc}. Since $\epsilon_{\mathrm{dc}} \propto I/B$, signals appearing at different harmonics of CR are not expected to evolve in a synchronous way as I is varied. This is evident for CR and its harmonics. For instance, the dc-current required to flip the MIRO peak at $\epsilon_{\mathrm{ac}} \simeq 2$ is only roughly half the corresponding value required to flip the peak at $\epsilon_{\mathrm{ac}} \simeq 1$.

This naive argument, however, does not seem to apply to the subharmonics of CR. The data clearly shows that the signal at $\epsilon_{\mathrm{ac}} \simeq 1/2$ is roughly synchronized with the signal at CR as I is tuned. This observation is more clearly shown in Fig. 6.2 in which we plot differential resistivity against ϵ_{dc} at $\epsilon_{\mathrm{ac}} = 1$ (a) and $\epsilon_{\mathrm{ac}} = 1/2$ (b). Since $B \simeq 0.6\,\mathrm{kG}$ at CR and $B \simeq 1.2\,\mathrm{kG}$ at $\epsilon_{\mathrm{ac}} = 1/2$, the synchronization behavior results in the observed doubling (halving) of oscillation frequency (period) at $\epsilon_{\mathrm{ac}} = 1/2$. This is not expected because the data at $\epsilon_{\mathrm{ac}} \geq 1$ all seems to suggest that the period (in terms of ϵ_{dc}) of oscillations in r_{xx} is not strongly dependent on ϵ_{ac}.

Using experimental data, we constructed gray-scale maps of differential resistivity in the $(\epsilon_{\mathrm{ac}}, \epsilon_{\mathrm{dc}})$-plane. Fig. 6.3 shows the map at around $(\epsilon_{\mathrm{ac}}, \epsilon_{\mathrm{dc}}) = (1, 1)$ (a) and

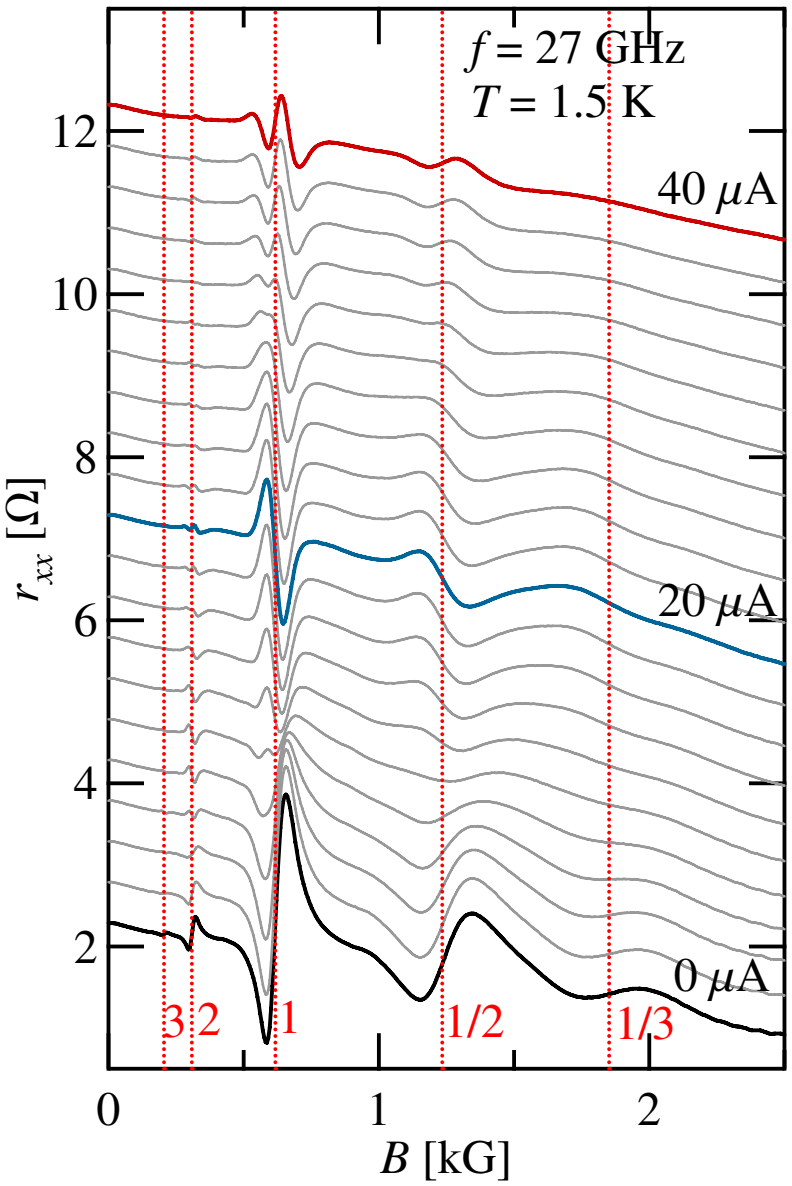

Figure 6.1: Differential magnetoresistivity measured at various dc-current bias (from $I = 0$ to $I = 40\,\mu$A in steps of $2\,\mu$A). The traces are vertically offset by $0.5\,\Omega$ for clarity. The vertical dashed lines mark the B values corresponding to integer and fractional $\epsilon_{\rm ac}$.

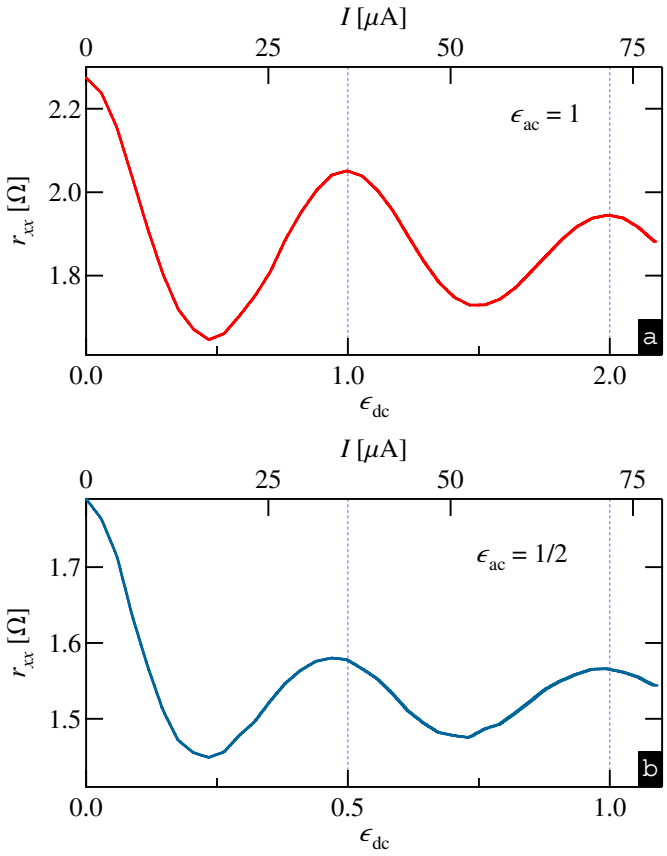

Figure 6.2: r_{xx} vs $\epsilon_{\rm dc}$ at $\epsilon_{\rm ac} = 1$ (a) and $\epsilon_{\rm ac} = 1/2$ (b). The period of oscillation at $\epsilon_{\rm ac} = 1/2$ is only half the corresponding value at $\epsilon_{\rm ac} = 1$. Top axes show the applied dc-current in μA.

$(1/2, 1/2)$ (b). Despite a difference by a factor of 2 in both axes, the landscapes in both images resemble each other at a fairly high degree. For instance, they both show two peaks along the diagonal, two troughs along the anti-diagonal, 3 saddle points along the central vertical line (the middle point and the two quarter-points). The positions of peaks, troughs, and saddle points at around $(\epsilon_{\rm ac}, \epsilon_{\rm dc}) = (1/2, 1/2)$ can all be reasonably predicted simply by scaling down the coordinates of the corresponding features at around $(\epsilon_{\rm ac}, \epsilon_{\rm dc}) = (1, 1)$.

6.3 Numerical results

To see how the observed "frequency doubling" at $\epsilon_{\rm ac} = 1/2$ came about, we first turned to Eq. (5.4). With $\epsilon_{\rm ac} = 1/2$, it is immediately reduced to Eq. (5.8). Thus, Eq. (5.4) does not predict the observed phenomenon. However, Eq. (5.4) was derived under the assumption that Landau levels are strongly overlapped and so the DoS could be modeled as

$$\nu(\varepsilon) = \nu_0 \left(1 - 2\delta \cos \frac{2\pi\varepsilon}{\hbar\omega_{\rm c}}\right) \tag{6.1}$$

When Landau levels get separated (as B gets stronger), Eq. (6.1) no longer adequately represents the reality. We estimated that $\hbar\omega_{\rm c} \simeq 6.8\hbar/\tau_{\rm q}$ at $\epsilon_{\rm ac} = 1/2$, which suggests that Landau levels are already well-separated at this point. It is conceivable that additional higher-frequency Fourier components that will enter Eq. (6.1) could in principle modify Eq. (5.4) and perhaps give rise to the observed frequency-doubling behavior. To verify this conjecture, we performed numerical computations based on the formalisms outlined in Ref. [71].

For a 2DEG under simultaneous MW irradiation and a dc-current bias, the dissipative current density (which is parallel to the Hall electric field) $j_d = j_1 + j_2$ consists of two parts:

$$j_1 = \frac{2e}{\nu_0} \int \frac{d\varphi d\varphi'}{(2\pi)^2} \int d\varepsilon \nu(\varepsilon)\nu(\varepsilon + W_{\varphi\varphi'}) \Delta X_{\varphi\varphi'} \left(\frac{1}{\tau_{\varphi\varphi'}} - \frac{\mathcal{P}_\omega}{\bar{\tau}_{\varphi\varphi'}}\right) \times$$
$$\times \left[f(\varepsilon) - f(\varepsilon + W_{\varphi\varphi'})\right] \tag{6.2}$$

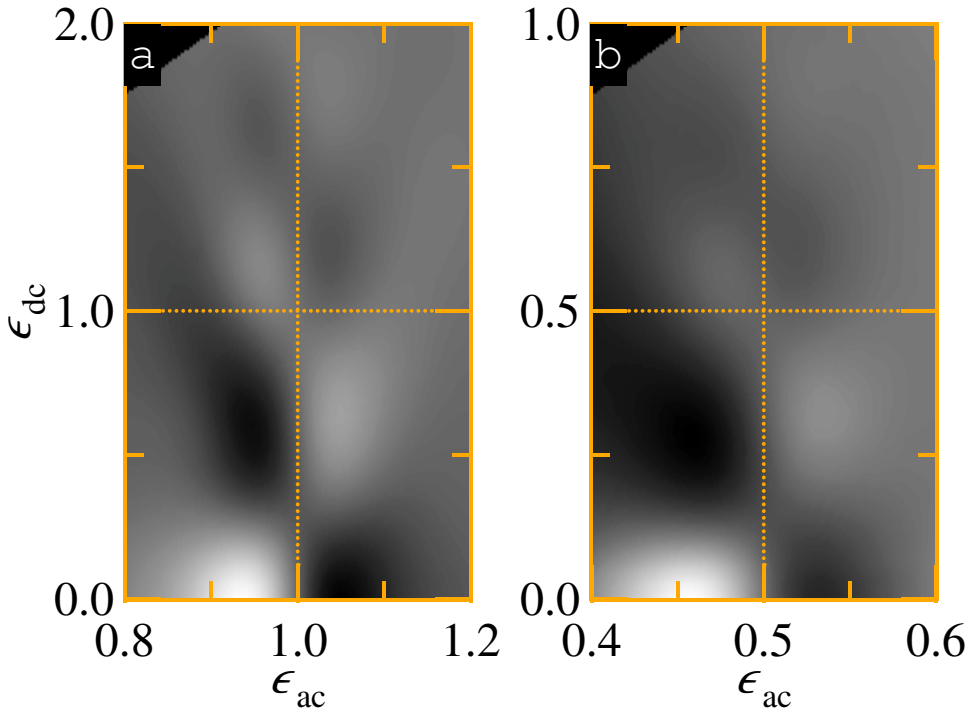

Figure 6.3: Gray-scale maps of r_{xx} in the $(\epsilon_{\rm ac}, \epsilon_{\rm dc})$-plane at around $(\epsilon_{\rm ac}, \epsilon_{\rm dc}) = (1, 1)$ (a) and $(\epsilon_{\rm ac}, \epsilon_{\rm dc}) = (1/2, 1/2)$ (b). Light (dark) regions correspond to higher (lower) values of r_{xx}.

and

$$j_2 = \frac{2e}{\nu_0}\frac{1}{2}\sum_{\pm}\int\frac{d\varphi d\varphi'}{(2\pi)^2}\int d\varepsilon\nu(\varepsilon)\nu(\varepsilon + W_{\varphi\varphi'} \pm \hbar\omega)\Delta X_{\varphi\varphi'}\times$$
$$\times\frac{\mathcal{P}_\omega}{\bar{\tau}_{\varphi\varphi'}}[f(\varepsilon) - f(\varepsilon + W_{\varphi\varphi'} \pm \hbar\omega)] \tag{6.3}$$

$\Delta X_{\varphi\varphi'} = R_c(\sin\varphi' - \sin\varphi)$ is the guiding center displacement, φ (φ') is the angle electron momentum makes with the Hall electric field before (after) a scattering event, $W_{\varphi\varphi'} = eE_H\Delta X_{\varphi\varphi'}$ is the work associated with the Hall electric field in the course of displacement $\Delta X_{\varphi\varphi'}$, $\hbar\omega$ is the energy of a MW quantum, $\mathcal{P}_\omega$ is proportional to MW power as we have mentioned in Chapter 5 and $\tau^{-1}_{\varphi\varphi'}$ is the elastic scattering rate in the absent of electric and magnetic fields as defined in Eq. (3.6). $\bar{\tau}^{-1}_{\varphi\varphi'}$ is associated with momentum relaxation and is related to $\tau^{-1}_{\varphi\varphi'}$ by

$$\frac{1}{\bar{\tau}_{\varphi\varphi'}} = \frac{1-\cos(\varphi'-\varphi)}{\tau_{\varphi\varphi'}}. \tag{6.4}$$

j_1 comes from the processes in which electrons do not actually absorb or emit MW quanta. It includes a term describing the effect due to a pure dc electric field and a term describing "virtual" processes in which momentum relaxation rate is modified due to electrons interacting with MW fields. j_2 arises from "real" processes in which absorption and/or emission of MW quanta by electrons actually takes place. DoS was modeled by a series of Gaussian functions as in Eq. (3.8). Strictly speaking, $f(\varepsilon)$ is a non-equilibrium electron energy distribution. As the lowest-order approximation, however, we simply replaced it with the Fermi-Dirac distribution as we did in Chapter 3. Once the dissipative current density was obtained, differential resistivity was computed using Eq. (3.7).

The numerical results are presented in Fig. 6.4. Following parameters were used in the simulations: $\tau_q = 20\,\text{ps}$; $\tau_{tr} = 435\,\text{ps}$; $\chi = 0.01$; $T = 1.5\,\text{K}$. At experimental MW frequency ($f = 27\,\text{GHz}$), $\epsilon_{ac} = 1/2$ corresponds to $B \simeq 1.2\,\text{kG}$ which gives $\omega_c\tau_q \simeq 6.8$. The simulations at this B do show "frequency doubling" within certain range of MW power (cf. the blue trace in Fig. 6.4(a)), although the oscillations are less pronounced compared to the experimental data (cf. Fig. 6.2(b)). At lower MW power (cf. the gray trace in Fig. 6.4(a)), the resonance peak at $\epsilon_{ac} = 1/2$ does not show up and the oscillations simply take the form of ordinary HIROs. At higher MW power (cf. the red

trace in Fig. 6.4(a)), oscillations appear to become 180° out-of-phase relative to ordinary HIROs.

To see how the degree of separation between Landau levels affects the numerical results, we performed simulations at $B = 5\,\mathrm{kG}$ (cf. Fig. 6.4(b)). Notice that $\epsilon_{\mathrm{ac}} = 1/2$ at this B requires MW frequency $f \simeq 110\,\mathrm{GHz}$. At the intermediate MW power (cf. the blue trace in Fig. 6.4(b)), we obtained fairly pronounced oscillations in r_{xx} with twice the ordinary HIRO frequency. The peak at $\epsilon_{\mathrm{ac}} = 1/2$ grows stronger with increasing MW power. It does not disappear at $\mathcal{P}_\omega$ as low as 0.1.

The numerical simulations at experimental B ($\simeq 1.2\,\mathrm{kG}$) do not show double-frequency oscillations with amplitudes as pronounced as the real data. Perhaps it is because the non-equilibrium electron energy distribution was not taken into account. Non-equilibrium electron energy distribution has the effect of narrowing resonance peaks and therefore could result in more pronounced double-frequency oscillations at lower B. The range of MW power within which frequency doubling can occur might also be expanded after non-equilibrium electron energy distribution is taken into account.

Another plausible explanation to the observed frequency-doubling phenomenon is to assume formation of additional energy bands within Landau-quantization gaps. This idea was originally developed to explain the MIRO-like features at around subharmonics of CR (*i.e* fractional values of ϵ_{ac}) [116]. According to this theory, MW-irradiation can induce "sidebands" above and below an ordinary Landau level at energies equal to $\varepsilon_N \pm \hbar\omega$ (where $\varepsilon_N = \hbar\omega_{\mathrm{c}}(N + 1/2)$). At $\epsilon_{\mathrm{ac}} = 1/2$, sidebands from adjacent Landau levels overlap exactly in the mid-gap. The period of DoS is thus reduced by a factor of 2. This means the increment of Hall electric field that is required for an electron to be scattered into the next higher energy level is also reduced by a factor of 2. As a result, r_{xx} oscillates with ϵ_{dc} at twice the ordinary HIRO frequency.

6.4 Summary

We observed frequency doubling at the second subharmonic of CR. The period (in terms of ϵ_{dc}) of oscillations in r_{xx} at $\epsilon_{\mathrm{ac}} = 1/2$ is only half the corresponding value at $\epsilon_{\mathrm{ac}} = 1$. By performing numerical simulations, we concluded that this is a phenomenon which could be understood within the theory recently developed by Khdoas *et al.*. An

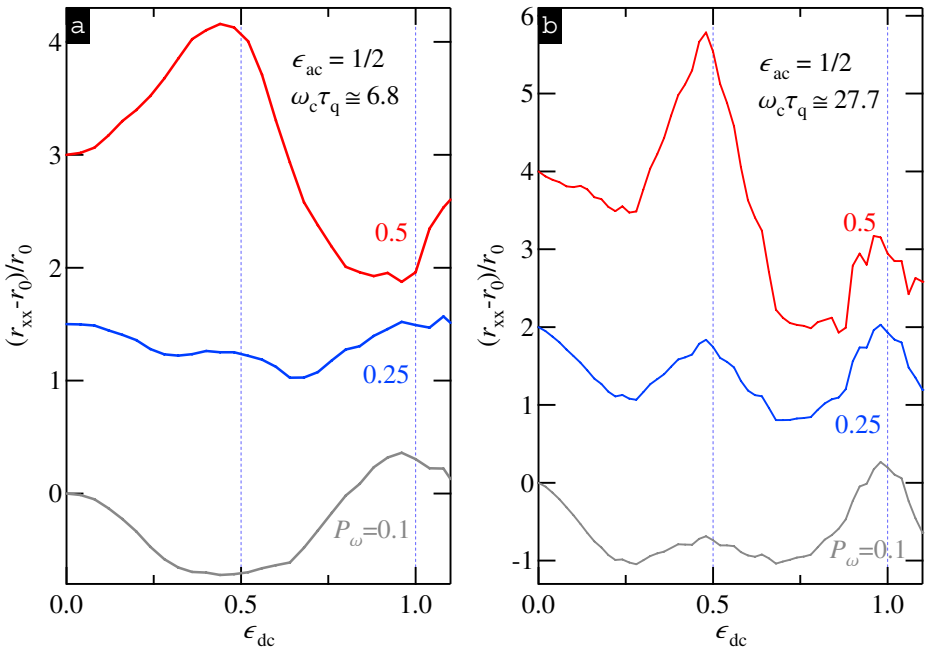

Figure 6.4: Differential resistivity at $\epsilon_{ac} = 1/2$ computed using Khodas *et al.*'s theory [71]. DoS was modeled by a series of Gaussian functions. Three different MW powers were simulated: $\mathcal{P}_\omega = 0.1$ (gray curves); 0.25 (blue curves); 0.5 (red curves). (a) $\omega_c\tau_q \simeq 6.8$ (at $B \simeq 1.2\,\mathrm{kG}$); (b) $\omega_c\tau_q \simeq 27.7$ (at $B \simeq 5\,\mathrm{kG}$). We used $\tau_q \simeq 20\,\mathrm{ps}$. The traces are vertically offset for clarity.

alternative explanation is to assume formation of MW-induced sidebands within the Landau-quantization gaps.

Chapter 7

Nonlinear transport in 2DEG under intense MW irradiation

7.1 Introduction

The possibility that multi-photon processes might be involved in producing the transport nonlinearity in MW-irradiated 2DEG is suggested by a series of experimental observations in which MIRO-like features appear near certain fractional values of ω/ω_c [73][114][3][113][118]. Theoretical work aims at explaining such observations based on the idea of multi-photon-assisted transport has been put forth by Lei *et al.* [115][119] and Dmitriev *et al.* [116]. As we have discussed in Chapter 5, differential resistivity in a 2DEG under simultaneous MW irradiation and a dc-current bias oscillates with $\epsilon_{ac} \pm \epsilon_{dc}$. Such combinations of parameters suggest that the observed nonlinearity in transport originates from single-photon processes [71]. As MW power increases, additional features appear near CR and its harmonics [120]. In this chapter, we will present our experimental results on this subject as well as their physical implications.

7.2 Experimental results

The experiments were performed at constant coolant temperature $T \simeq 1.5\,\mathrm{K}$. The 2DEG was continuously irradiated by MW at frequency $f = 27\,\mathrm{GHz}$. Differential resistivity was measured at various dc-current bias. Data was presented in Fig. 7.1 for $I = 0$ (a)

and $I \neq 0$ (b). Without a dc-current bias, exactly one peak and one trough appear near CR ($\epsilon_{\rm ac} = 1$) and its harmonics (cf. the signal at around $\epsilon_{\rm ac} = 2$). The peak and the trough are roughly positioned symmetrically about integer $\epsilon_{\rm ac}$ (the vertical lines). When a finite dc-current is applied to the 2DEG, multiple peaks and troughs are observed near CR and its harmonics. For instance, the $I = 64\,\mu$A trace shows three peaks (indicated by $\uparrow$) and three troughs (indicated by $\downarrow$) at around CR. We estimated that $2\pi\epsilon_{\rm dc} \gtrsim 10$ and $E_H \gtrsim 0.5\,$V/cm at CR ($B \simeq 0.6\,$kG) for the data presented in Fig. 7.1(b). The signal gets much weaker at the second harmonic but multiple peaks and troughs could still be discerned. As we will discuss in the next section, this new phenomenon manifests the importance of multi-photon-assisted electrical transport in a 2DEG under intense MW irradiation as well as a strong dc-current bias.

7.3 Theoretical predictions

The theoretical differential resistivity was derived by Khodas *et al.* [71][120]. The expression has been given in Eq. (5.4). In Chapter 5, we only stated that $\mathcal{P}_\omega$ is a dimensionless parameter proportional to the power of unpolarized MW. In full details, it is defined as

$$\begin{aligned} \mathcal{P}_\omega &= \mathcal{P}_\omega^+ + \mathcal{P}_\omega^- \\ \mathcal{P}_\omega^\pm &= \frac{\mathcal{P}_\omega^{(0)}}{(\omega \pm \omega_{\rm c})^2\tau_{\rm em}^2 + 1}, \quad \mathcal{P}_\omega^{(0)} = \frac{e^2\mathcal{E}_{\rm ac}^2 v_{\rm F}^2 \tau_{\rm em}^2}{2\epsilon_{\rm eff}\hbar^2\omega^2} \end{aligned} \tag{7.1}$$

$\mathcal{P}_\omega^+$ ($\mathcal{P}_\omega^-$) is the dimensionless power for left (right)-circularly polarized MW, $\mathcal{E}_{\rm ac}$ is the MW electric field, $\tau_{\rm em} = 2\epsilon_0\sqrt{\epsilon_{\rm eff}}m^*c/n_{\rm e}e^2$ is the electromagnetic damping time ($\tau_{\rm em} \simeq 7.2\,$ps in our sample) and $2\sqrt{\epsilon_{\rm eff}} = \sqrt{\epsilon} + 1$ with $\epsilon \simeq 12.8$ (the dielectric constant of GaAs).

Two different methods were suggested by Khodas *et al.* regarding how $\mathcal{P}_\omega^{(0)}$ could be extracted from experimental data. The first method is by using the position of the peak closest to CR. At $\epsilon_{\rm dc} = n + 1/4$ (n is a positive integer), Eq. (5.4) is reduced to

$$\frac{r - r_{\rm D}}{r_{\rm D}} = \frac{(4\delta)^2\tau_{\rm tr}}{\pi\tau_\pi}\left(-\frac{2\sqrt{\mathcal{P}_\omega}}{n + 1/4}\right)\epsilon_{\rm ac}\cos(\pi\epsilon_{\rm ac})J_1(4\sqrt{\mathcal{P}_\omega}\sin\pi\epsilon_{\rm ac}) \tag{7.2}$$

Numerical investigation shows that when $\mathcal{P}_\omega$ is sufficiently large (say, $\mathcal{P}_\omega \gtrsim 1$) the $\epsilon_{\rm ac}$ coordinate of such a peak at this specific $\epsilon_{\rm dc}$ coordinate (*i.e.* $n + 1/4$) can be fairly

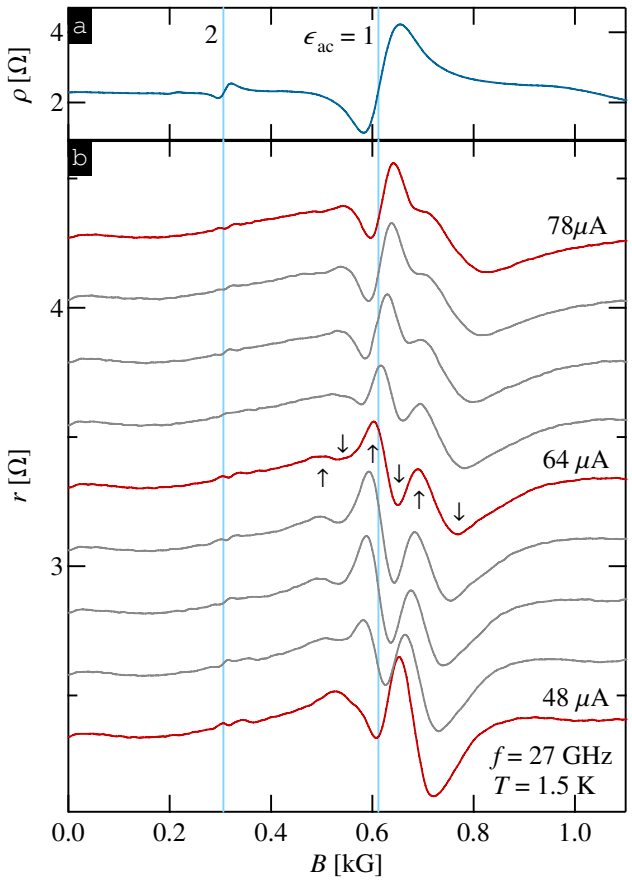

Figure 7.1: Magnetotransport in a high-mobility 2DEG under intense MW irradiation at frequency $f = 27\,\mathrm{GHz}$. (a) Linear-response magnetoresivitity. (b) Differential magnetoresistivity measured at various dc-current bias (from $I = 48\,\mu\mathrm{A}$ to $78\,\mu\mathrm{A}$ in steps of $4\,\mu\mathrm{A}$). The traces have been vertically offset for clarity. The vertical lines mark the B values corresponding to CR (*i.e.* $\epsilon_{\mathrm{ac}} = 1$) and its second harmonic (*i.e.* $\epsilon_{\mathrm{ac}} = 2$). The three upward (downward) arrows next to the $I = 64\,\mu\mathrm{A}$ trace indicate the positions of its three peaks (troughs) at around CR.

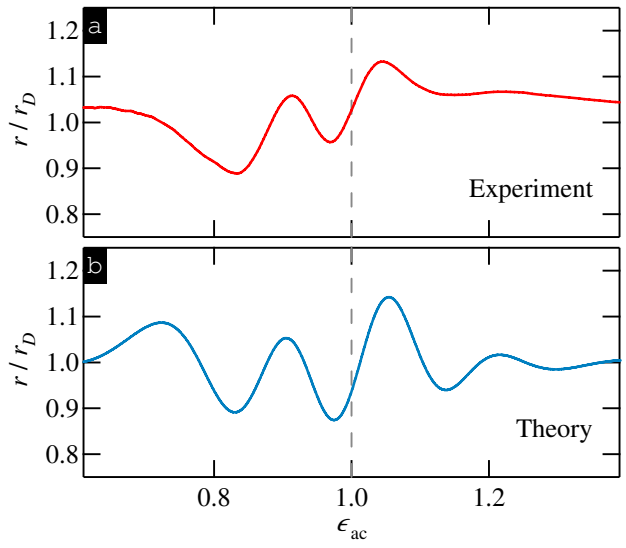

Figure 7.2: Magnetoresistivity at around CR plotted against dimensionless parameter $\epsilon_{\rm ac}$. (a) Experimental data at $I = 54\,\mu$A. (b) Theoretical curve generated using $\mathcal{P}_\omega^{(0)} = 7.7$.

accurately determined by the first (nontrivial) zero of $J_1(x)$. The first nontrivial zero of $J_1(x)$ is at $x \simeq 1.84$, so the $\epsilon_{\rm ac}$ coordinate of such a peak should satisfy the following relation:

$$4\sqrt{\mathcal{P}_\omega}\sin\pi\epsilon_{\rm ac} \simeq 1.84 \tag{7.3}$$

From our data, we found that at $\epsilon_{\rm dc} \simeq 1.25$ such a peak has coordinates $(\epsilon_{\rm ac}, \epsilon_{\rm dc}) \simeq (0.95, 1.25)$. Using this $\epsilon_{\rm ac}$ coordinate and Eq. (7.3) together with Eq. (7.1), we obtained $\mathcal{P}_\omega^{(0)} \simeq 7.7$.

The second method is by directly comparing the theoretical curve with the experimental data. $\mathcal{P}_\omega^{(0)}$ is adjusted until the theoretical predicted features at around CR closely match up the actual observed features. Fig. 7.2(a) shows experimental data measured at $I = 54\,\mu$A and (b) shows the curve generated using Eq. (5.4) at the same dc-current bias. Here we used $\tau_{\rm q} \simeq 15\,$ps and $\tau_{\rm tr}/\tau_\pi \simeq 0.18$ [103]. With $\mathcal{P}_\omega^{(0)} = 7.7$, the predicted positions of the peaks and troughs at around CR reasonably match up the actual ones. The predicted amplitude of these oscillations also agree well with the experimental data (in both cases $(r - r_{\rm D})/r_{\rm D} \simeq 0.1$).

The data taken at various MW power is presented in Fig. 7.3(a) (with the dc-current

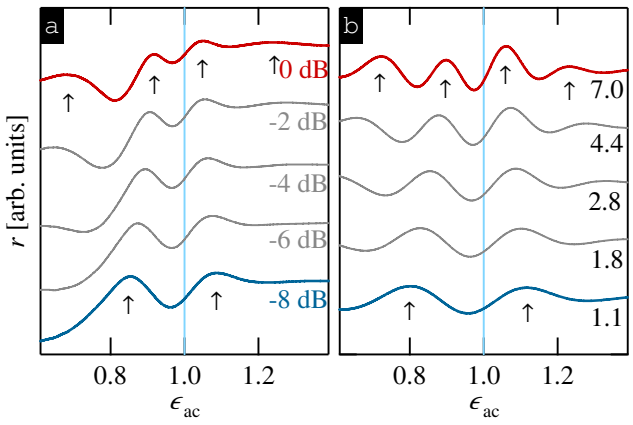

Figure 7.3: MW power dependence of differential magnetoresistivity at $I = 54\,\mu$A. (a) Experimental data. The numbers indicate how much the Gunn oscillator output was attenuated. (b) Theoretical predictions. The numbers indicate the $\mathcal{P}_\omega^{(0)}$ values that were used in generating these curves.

bias fixed at $I = 54\,\mu$A). The numbers mark the attenuation applied to the output of the Gunn oscillator. The "period" of the oscillatory features decreases with increasing MW power. With full MW power, four peaks (↑) appear at around CR. At 8 dB below the full power, only two peaks (↑) remain in the window. The theoretical curves are plotted in Fig. 7.3(b). The numbers indicate the $\mathcal{P}_\omega^{(0)}$ values. The $\mathcal{P}_\omega^{(0)}$ value of each trace relative to the highest power (*i.e.* $\mathcal{P}_\omega^{(0)} = 7.0$) reflects the actual power ratio shown in Fig. 7.3(a). The theory reasonably captures the observed MW power dependence.

Khodas *et al.* pointed out that the phase of the electron wave function would change periodically due to intense MW irradiation. As a result, the electron wave function acquires components which have energies ε, $\varepsilon \pm \hbar\omega$, $\varepsilon \pm 2\hbar\omega$,..., etc. ($\varepsilon$ being the electron eigenenergy in the absence of MW fields). Effectively, Floquet bands of levels separated by $\hbar\omega$ are formed in the electron energy spectrum. Electrons can be scattered between Floquet bands. The scattering probability is proportional to the overlap between the initial and the final Floquet bands. The overlap is given by the following parameter:

$$\alpha_\theta^{(N)} = J_N^2[\sqrt{2\mathcal{P}_\omega(1-\cos\theta)}] \tag{7.4}$$

$J_N(x)$ is the Nth order Bessel function of the first kind. θ is the scattering angle. Eq. (7.4) describes scattering accompanied by absorption/emission of $|N|$ MW quanta.

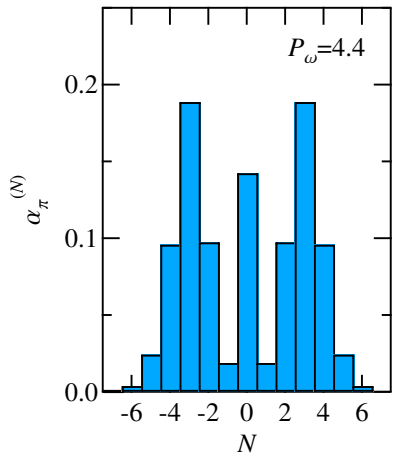

Figure 7.4: $\alpha_\pi^{(N)}$ vs N for $\mathcal{P}_\omega = 4.4$. $\alpha_\pi^{(N)} = J_N^2(2\sqrt{\mathcal{P}_\omega})$ describes the overlap between the initial and the final Floquet bands in which an electron undergoes backscattering accompanied by absorbing or emitting $|N|$ MW quanta.

In strong dc electric fields, the main contribution to the dissipative current density comes from electrons backscattered ($\theta = \pi$) off impurity. Under such condition, Eq. (7.4) becomes $\alpha_\pi^{(N)} = J_N^2(2\sqrt{\mathcal{P}_\omega})$. Fig. 7.4 plots $\alpha_\pi^{(N)}$ vs N for $\mathcal{P}_\omega = 4.4$. $\alpha_\pi^{(N)}$ strongly peaks at $N = 0$ and $|N| = 3$. It decays away rapidly when $|N| > 3$. Mathematically, $J_N(x)$ diminishes quickly as $|N|$ increases beyond x. Therefore, the number of MW quanta that can be absorbed/emitted by an electron is limited by:

$$|N| \leq N_{\rm m} \approx 2\sqrt{\mathcal{P}_\omega} \tag{7.5}$$

$N_{\rm m}$ is the maximum number of MW quanta that can be absorbed/emitted by an electron for a given power $\mathcal{P}_\omega$.

Under the condition that $\mathcal{P}_\omega \gtrsim 1$, Eq. (5.4) asymptotically approaches the following form at around CR:

$$\frac{r - r_{\rm D}}{r_{\rm D}} \propto \sum_{\pm} (\epsilon_{\rm dc} \pm 2\sqrt{\mathcal{P}_\omega}\epsilon_{\rm ac}) \cos[2\pi(2\sqrt{\mathcal{P}_\omega}\epsilon_{\rm ac} \pm \epsilon_{\rm dc}) + \vartheta]$$
$$\text{with } \vartheta = \pi/4 - 4\pi\sqrt{\mathcal{P}_\omega} \tag{7.6}$$

According to Eq. (7.6), processes involving $|N|$ photons give rise to a resonance peak in

differential resistivity when the following conditions are satisfied:

$$|N|\epsilon_{\rm ac} + \epsilon_{\rm dc} \simeq n$$
$$|N|\epsilon_{\rm ac} - \epsilon_{\rm dc} \simeq m - 1/2 \tag{7.7}$$

m, n are positive integers. Eq. (7.7) is apparently the high MW-power version of Eq. (5.3). Close to CR, once the resonance conditions are met for $N_{\rm m}$ MW quanta they will automatically hold for the rest of $|N| < N_{\rm m}$. Thus, their contributions to electrical transport would be constructive.

Under typical experimental conditions, the dominant contribution to r comes from the "+" term in Eq. (7.6). As a result, oscillations in r at around CR is roughly periodic in $2\sqrt{\mathcal{P}_\omega}\epsilon_{\rm ac} + \epsilon_{\rm dc}$. At fixed dc-current bias and MW frequency, the ratio $\eta \equiv \epsilon_{\rm dc}/\epsilon_{\rm ac} \propto I/\omega$ is a constant (it does not depend on magnetic field B). Since $2\sqrt{\mathcal{P}_\omega}\epsilon_{\rm ac} + \epsilon_{\rm dc} = (2\sqrt{\mathcal{P}_\omega} + \eta)\epsilon_{\rm ac}$, r vs $\epsilon_{\rm ac}$ at around CR shows roughly periodic oscillations with the period given by $(2\sqrt{\mathcal{P}_\omega} + \eta)^{-1}$. For the data in Fig. 7.2(a) $\mathcal{P}_\omega \approx \mathcal{P}_\omega^{(0)} \simeq 7.7$ at around CR and $\eta = 1.65$, the theory predicts that $(2\sqrt{\mathcal{P}_\omega} + \eta)^{-1} \simeq 0.14$. This value agrees reasonably well with the observed separation between the resonance peaks in Fig. 7.2(a).

7.4 Summary

We observed multiple resonance peaks and troughs at around CR and its harmonics in differential resistivity of a high-mobility 2DEG under intense MW irradiation and a strong dc-current bias. The positions of these resonance peaks and troughs strongly depend on the MW intensity. Theoretically, the observed features are understood as the manifestation of multi-photon processes in which electrons are backscattered between Floquet bands of levels accompanied by absorption/emission of multiple MW quanta.

Chapter 8

Conclusion

In this thesis, we have presented our studies on nonlinear electrical transport in high-mobility 2DEG at very high Landau levels (with filling factor $\nu > 50$). Under a pure dc-current bias, differential resistivity of a 2DEG shows features similar to those previously observed in MW photoresistance. A dc-current bias can induce dramatic oscillatory structure in differential magnetoresistivity just like MW irradiation can induce giant oscillatory structure in linear-response magnetoresistivity. The minima of these dc-driven oscillations can reach down to zero forming ZdRS just like ZRS can arise from the minima of MIRO. The phenomenological similarity between a dc-driven and a MW-driven 2DEG suggests that the physical mechanisms responsible for the observed transport nonlinearity in both cases are closely related.

The initial motivation of introducing a dc-current bias into a MW-irradiated 2DEG is to search for a hypothetical critical current density above which ZRS is expected to breakdown. Although such investigations have not unambiguously identified this critical current density, unexpected nonlinear transport phenomena in 2DEG were observed due to the coexistence of MW radiation and a dc-current bias. For instance, oscillations in differential resistivity are almost completely suppressed at half-integer $\epsilon_{\rm ac}$ and the effect of MW radiation appears to be nullified at integer $\epsilon_{\rm ac}$. The MIRO-like signal at the second subharmonic of CR evolves in a synchronous fashion with that at CR as the applied dc-current bias is varied. Such synchronization results in differential resistivity at the second subharmonic of CR oscillating with parameter $\epsilon_{\rm dc}$ with twice the frequency as compared to that at CR. Under high intensity MW irradiation as well as a strong

dc-current bias, multiple resonance peaks and troughs appear at around CR and its harmonics. The separation between these resonance peaks is strongly dependent on the MW intensity.

At first sight, the observed nonlinear transport phenomena in 2DEG under simultaneous MW irradiation and a dc-current bias are quite complicated and diverse. They appear to be not particularly connected to each other. It turns out that they can all be understood (at least qualitatively) within the theoretical work recently put forth by Khodas *et al.* [71]. Their analysis is built on a quantum Boltzmann equation derived for a weakly disordered 2DEG. They showed that the observed nonlinearity in electrical transport stems from two coexisting effects: formation of non-equilibrium electron energy distribution and modulation of electron scattering rate due to the presence of dc and ac electric fields.

We compared Khodas *et al.*'s theory with our experimental data both in the regimes of overlapped and separated Landau levels. In the regime of overlapped Landau levels, their analytical results readily explain why r vs $\epsilon_{\rm dc}$ is essentially featureless at half-integer $\epsilon_{\rm ac}$ and why it looks like ordinary HIROs at integer $\epsilon_{\rm ac}$ despite the presence of MW radiation. In essence, they are the consequence of "magical" full/partial cancellation between the contributions coming from "virtual" (in the sense that electrons interacting with MW fields without actually absorbing/emitting MW quanta) and "real" (in the sense that absorption/emission of MW quanta actually takes place) processes. The theory also recreates the observed multiple resonance peaks and troughs at around CR when the 2DEG is subjected to intense MW irradiation and a strong dc electric field. It is understood that these features arise from electrons backscattered between Floquet bands of levels accompanied by absorption/emission of multiple MW quanta.

The observed "frequency-doubling" behavior at the second subharmonic of CR cannot be readily explained by the analytical results which are derived assuming overlapped Landau levels. By modeling the DoS with a series of Gaussian functions and performing numerical simulations, we found that the "frequency-doubling" behavior could also arise naturally from Khodas *et al.*'s theory. The effect of higher order harmonics in the DoS when Landau levels get separated also manifests on nonlinear transport in purely dc-driven 2DEG in which a flat-bottom valley is developed right after an initial sharp drop of differential resistivity at low dc-current bias ($\epsilon_{\rm dc} < 1$).

The resemblance between ZRS and ZdRS was proved to be more than simply cosmetic. Theoretically, both of them could be explained in terms of formation of current domains in responding to the instability associated with local absolute negative resistivity [51][104]. Despite its theoretical ingenuity, the existence of current domains has yet to be proved experimentally.

Bibliography

[1] T. Ihn. *Semiconductor nanostructures*. Oxford University Press, United Kingdom, 2010.

[2] T. Ando, A.B. Fowler, and F. Stern. Electronic properties of two-dimensional systems. *Rev. Mod. Phys.*, **54**:437, 1982.

[3] M.A. Zudov. Period and phase of microwave-induced resistance oscillations and zero-resistance states in two-dimensional electron systems. *Phys. Rev. B*, **69**:41304, 2004.

[4] R.R. Gerhardtz. Cumulant approach to the two-dimensional magneto-conductivity problem. *Surf. Sci.*, **58**:227, 1976.

[5] N. Romero, S. McHugh, M.P. Sarachik, S.A. Vitkalov, and A.A. Bykov. Effect of parallel magnetic field on the zero-differential resistance state. *Phys. Rev. B*, **78**:153311, 2008.

[6] M.E. Raikh and T.V. Shahbazyan. High landau levels in a smooth random potential for two-dimensional electrons. *Phys. Rev. B*, **47**:1522, 1993.

[7] D. Shoenberg. The magnetic properties of bismuth. III. Further measurements on the de Haas-Van Alphen effect. *Proc. Roy. Soc. (London) A*, **170**:341, 1939.

[8] R.B. Dingle. Some magnetic properties of metals. I. General introduction, and properties of large systems of electrons. *Proc. Roy. Soc. (London) A*, **211**:500, 1952.

[9] R.B. Dingle. Some magnetic properties of metals. II. The influence of collisions on the magnetic behavior of large systems. *Proc. Roy. Soc. (London) A*, **211**:517, 1952.

[10] L. Shubnikov and W.J. de Haas. —. *Leiden Comm.*, **207a**:3, 1930.

[11] A.B. Fowler, F.F. Fang, W.E. Howard, and P.J. Stiles. Magneto-oscillatory conductance in silicon surfaces. *Phys. Rev. Lett.*, **16**:901, 1966.

[12] T. Ando and Y. Uemura. Theory of quantum transport in a two-dimensional electron system under magnetic fields. I. Characteristics of level broadening and transport under strong fields. *J. Phys. Soc. Jpn*, **36**:959, 1974.

[13] T. Ando. Theory of quantum transport in a two-dimensional electron system under magnetic fields. IV. Oscillatory conductivity. *J. Phys. Soc. Jpn*, **37**:1233, 1974.

[14] T. Ando, Y. Matsumoto, and Y. Uemura. Theory of Hall effect in a two-dimensional electron system. *J. Phys. Soc. Jpn*, **39**:279, 1975.

[15] A. Isihara and L. Smrčka. Density and magnetic field dependences of the conductivity of two-dimensional electron systems. *J. Phys. C*, **19**:6777, 1986.

[16] P.T. Coleridge, R. Stoner, and R. Fletcher. Low-field transport coefficients in GaAs/$Ga_{1-x}Al_x$As heterostructures. *Phys. Rev. B*, **39**:1120, 1989.

[17] B. Laikhtman and E.L. Altshuler. Quasiclassical theory of Shubnikov-de Haas effect in 2D electron gas. *Ann. Phys.*, **232**:332, 1994.

[18] P.T. Coleridge. Small-angle scattering in two-dimensional gases. *Phys. Rev. B*, **44**:3793, 1991.

[19] P.T. Coleridge, M. Hayne, P. Zawadzki, and A.S. Sachrajda. Effective masses in high-mobility 2D electron gas structures. *Surface Science*, **361**:560, 1996.

[20] K.v. Klitzing, G. Dorda, and M. Pepper. New method for high-accuracy determination of the fine-structure constant based on quantized Hall resistance. *Phys. Rev. Lett.*, **45**:494, 1980.

[21] M.A. Paalanen, D.C. Tsui, and A.C. Gossard. Quantized Hall effect at low temperatures. *Phys. Rev. B*, **25**:5566, 1982.

[22] H.P. Wei, A.M Chang, and D.C. Tsui. Temperature dependence of the quantized Hall effect. *Phys. Rev. B*, **32**:7016, 1985.

[23] R.B. Laughlin. Quantized Hall conductivity in two dimensions. *Phys. Rev. B*, **23**:5632, 1981.

[24] D.J. Thouless. Localization and the two-dimensional Hall effect. *J. Phys. C*, **14**:3475, 1981.

[25] B.I. Halperin. Quantized Hall conductance, current-carrying edge states, and the existence of extended states in a two-dimensional disordered potential. *Phys. Rev. B*, **25**:2185, 1982.

[26] M. Büttiker. Absence of backscattering in the quantum Hall effect in multiprobe conductors. *Phys. Rev. B*, **38**:9375, 1988.

[27] K. Hashimoto, C. Sohrmann, J. Wiebe, T. Inaoka, F. Meier, Y. Hirayama, and R.A. Römer. Quantum Hall transition in real space: From localized to extended states. *Phys. Rev. Lett.*, **101**:256802, 2008.

[28] D.C. Tsui, H.L. Störmer, and A.C. Gossard. Two-dimensional magnetotransport in the extreme quantum limit. *Phys. Rev. Lett.*, **48**:1559, 1982.

[29] R.L. Willett, H.L. Störmer, D.C. Tsui, A.C. Gossard, and J.H. English. Quantitative experimental test for the theoretical gap energies in the fractional quantum Hall effect. *Phys. Rev. B*, **37**:8476, 1988.

[30] R. Willett, J.P. Eisenstein, H.L. Störmer, D.C. Tsui, A.C. Gossard, and J.H. English. Observation of an even-denominator quantum number in the fractional quantum Hall effect. *Phys. Rev. Lett.*, **59**:1776, 1987.

[31] S. Das Sarma and A. Pinczuk (editors). *Perspectives in quantum Hall effects*. John Wiley & Sons, Inc., United States, 1997.

[32] W. Pan, J.-S. Xia, V. Shvarts, D.E. Adams, H.L. Störmer, D.C. Tsui, L.N. Pfeiffer, K.W. Baldwin, and K.W. West. Exact quantization of the even-denominator fractional quantum Hall state at $\nu = 5/2$ Landau level filling factor. *Phys. Rev. Lett.*, **83**:3530, 1999.

[33] J.P. Eisenstein, R. Willett, H.L. Störmer, and D.C. Tsui. Collapse of the even-denominator fractional quantum Hall effect in tilted fields. *Phys. Rev. Lett.*, **61**:997, 1988.

[34] J.P. Eisenstein, R.L. Willett, H.L. Störmer, L.N. Pfeiffer, and K.W. West. Activation energies for the even-denominator fractional quantum Hall effect. *Surface Science*, **229**:31, 1990.

[35] R.B. Laughlin. An incompressible quantum fluid with fractionally charged excitations. *Phys. Rev. Lett.*, **50**:1395, 1983.

[36] F.D.M. Haldane. Fractional quantization of the Hall effect: A hierarchy of incompressible quantum fluid states. *Phys. Rev. Lett.*, **51**:605, 1983.

[37] B.I. Halperin. Statistics of quasiparticles and the hierarchy of fractional quantized Hall states. *Phys. Rev. Lett.*, **52**:1583, 1984.

[38] J.K. Jain. Composite-fermion approach for the fractional quantum Hall effect. *Phys. Rev. Lett.*, **63**:199, 1989.

[39] W. Pan, H.L. Stormer, D.C. Tsui, L.N. Pfeiffer, K.W. Baldwin, and K.W. West. Fractional quantum Hall effect of composite fermions. *Phys. Rev. Lett.*, **90**:16801, 2003.

[40] F.D.M. Haldane and E.H. Rezayi. Spin-singlet wave function for the half-integral quantum Hall effect. *Phys. Rev. Lett.*, **60**:956, 1988.

[41] D. Yoshioka, A.H. MacDonald, and S.M. Girvin. Connection between spin-singlet and hierarchical wave functions in the fractional quantum Hall effect. *Phys. Rev. B*, **38**:3636, 1988.

[42] M. Greiter, X.-G. Wen, and F. Wilczek. Paired Hall state at half filling. *Phys. Rev. Lett.*, **66**:3205, 1991.

[43] M. Greiter and F. Wilczek. Exact solution and the adiabatic heuristic for quantum Hall state. *Nucl. Phys. B*, **370**:577, 1992.

[44] E. Vasiliadou, G. Müller, D. Heitmann, D. Weiss, K.v. Klitzing, H. Nickel, W. Schlapp, and R. Lösch. Collective response in the microwave photoconductivity of hall bar structures. *Phys. Rev. B*, **48**:17145, 1993.

[45] P.D. Ye, L.W. Engel, D.C. Tsui, J.A. Simmons, J.R. Wendt, G.A. Vawter, and J.L. Reno. Giant microwave photoresistance of two-dimensional electron gas. *Appl. Phys. Lett.*, **79**:2193, 2001.

[46] M.A. Zudov, R.R. Du, J.A. Simmons, and J.L.Reno. Shubnikov-de Haas-like oscillations in millimeterwave photoconductivity in a high-mobility two-dimensional electron gas. *Phys. Rev. B*, **64**:201311, 2001.

[47] R.G. Mani, J.H. Smet, K. von Klitzing, V. Narayanamurti, W.B. Johnson, and V. Umansky. Demonstration of a 1/4-cycle phase shift in the radiation-induced oscillatory magnetoresistance in GaAs/AlGaAs devices. *Phys. Rev. Lett.*, **92**:146801, 2004.

[48] R.G. Mani, J.H. Smet, K. v. Klitzing, V. Narayanamurti, W.B. Johnson, and V. Umansky. Zero-resistance states induced by electromagnetic-wave excitation in GaAs/AlGaAs heterostructures. *Nature*, **420**:646, 2002.

[49] M.A. Zudov, R.R. Du, L.N. Pfeiffer, and K.W. West. Evidence for a new dissipationless effect in 2D electronic transport. *Phys. Rev. Lett.*, **90**:46807, 2003.

[50] R.L. Willett, L.N. Pfeiffer, and K.W. West. Evidence for current-flow anomalies in the irradiated 2D electron system at small magnetic fields. *Phys. Rev. Lett.*, **93**:26804, 2004.

[51] A.V. Andreev, I.L. Aleiner, and A.J. Millis. Dynamical symmetry breaking as the origin of the zero-dc-resistance state in an ac-driven system. *Phys. Rev. Lett.*, **91**:056803, 2003.

[52] S.A. Studenikin, M. Potemski, P.T. Coleridge, A.S. Sachrajda, and Z.R. Wasilewski. Microwave radiation induced magneto-oscillations in the longitudinal

and transverse resistance of a two-dimensional electron gas. *Solid State Commun.*, **129**:341, 2004.

[53] C.L. Yang, M.A. Zudov, T.A. Knuuttila, and R.R. Du. Observation of microwave-induced zero-conductance state in corbino rings of a two-dimensional electron system. *Phys. Rev. Lett.*, **91**:096803, 2003.

[54] R.G. Mani. Radiation-induced oscillatory magnetoresistance in a tilted magnetic field in GaAs/Al_xGa_{1-x}As devices. *Phys. Rev. B*, **72**:75327, 2005.

[55] C.L. Yang, R.R. Du, L.N. Pfeiffer, and K.W. West. Influence of a parallel magnetic field on the microwave photoconductivity in a high-mobility two-dimensional electron system. *Phys. Rev. B*, **74**:045315, 2006.

[56] C. Joas. *Quantum Hall systems in high Landau levels.* Freie Universität Berlin, 2006.

[57] J.H. Smet, B. Gorshunov, C. Jiang, L. Pfeiffer, K. West, V. Umanksy, M. Dressel, R. Meisels, F. Kuchar, and K. v. Klitzing. Circular-polarization-dependence study of the microwave photoconductivity in a two-dimensional electron system. *Phys. Rev. Lett.*, **95**:116804, 2005.

[58] A.A. Koulakov and M.E. Raikh. Classical model for the negative dc conductivity of ac-driven two-dimensional electrons near the cyclotron resonance. *Phys. Rev. B*, **68**:115324, 2003.

[59] M.G. Vavilov and I.L. Aleiner. Magnetotransport in a two-dimensional electron gas at large filling factors. *Phys. Rev. B*, **69**:35303, 2004.

[60] I.A. Dmitriev, M.G. Vavilov, I.L.Aleiner, A.D. Mirlin, and D.G. Polyakov. Theory of microwave-induced oscillations in the magnetoconductivity of a two-dimensional electron gas. *Phys. Rev. B*, **71**:115316, 2005.

[61] M.A. Zudov, R.R. Du, L.N. Pfeiffer, and K.W. West. Bichromatic microwave photoresistance of a two-dimensional electron system. *Phys. Rev. Lett.*, **96**:236804, 2006.

[62] J. Shi and X.C. Xie. Radiation-induced zero-resistance state and the photon-assisted transport. *Phys. Rev. Lett.*, **91**:086801, 2003.

[63] V.I. Ryzhii. Photoconductivity characteristics in thin films subjected to crossed electric and magnetic fields. *Fiz. Tverd. Tela (Leningrad)*, **11**:2577, 1969.

[64] V.I. Ryzhii, R.A. Suris, and B.S. Shchamkhalova. Photoconductivity of a two-dimensional electron gas in a strong magnetic field. *Fiz. Tekh. Poluprovodn. (S.-Peterburg)*, **20**:2078, 1986.

[65] A.C. Durst, S. Sachdev, N. Read, and S.M. Girvin. Radiation-induced magnetoresistance oscillations in a 2D electron gas. *Phys. Rev. Lett.*, **91**:086803, 2003.

[66] X.L. Lei and S.Y. Liu. Radiation-induced magnetoresistance oscillation in a two-dimensional electron gas in Faraday geometry. *Phys. Rev. Lett.*, **91**:226805, 2003.

[67] V. Ryzhii and R. Suris. Nonlinear effects in microwave photoconductivity of two-dimensional electron system. *J. Phys.: Condens. Matter*, **15**:6855, 2003.

[68] V. Ryzhii and V. Vyurkov. Absolute negative conductivity in two-dimensional electron systems associated with acoustic scattering stimulated by microwave radiation. *Phys. Rev. B*, **68**:165406, 2003.

[69] V. Ryzhii. Microwave photoconductivity in two-dimensional electron systems due to photon-assisted interaction of electrons with leaky interface phonons. *Phys. Rev. B*, **68**:193402, 2003.

[70] V. Shikin. Photoconductivity of 2D electron systems in magnetic field. *JETP Letters*, **77**:236, 2003.

[71] M. Khodas and M.G. Vavilov. Effect of microwave radiation on the nonlinear resistivity of a two-dimensional electron gas at large filling factors. *Phys. Rev. B*, **78**:245319, 2008.

[72] I. A. Dmitriev, M. Khodas, A. D. Mirlin, D. G. Polyakov, and M. G. Vavilov. Mechanisms of the microwave photoconductivity in two-dimensional electron systems with mixed disorder. *Phys. Rev. B*, 80:165327, 2009.

[73] S.I. Dorozhkin. Giant magnetoresistance oscillations caused by cyclotron resonance harmonics. *JETP Lett.*, **77**:577, 2003.

[74] I.A. Dmitriev, A.D. Mirlin, and D.G. Polyakov. Cyclotron-resonance harmonics in the ac response of a 2D electron gas with smooth disorder. *Phys. Rev. Lett.*, **91**:226802, 2003.

[75] I.A. Dmitriev, M.G. Vavilov, I.L. Aleiner, A.D. Mirlin, and D.G. Polyakov. Oscillatory ac conductivity and photoconductivity of a two-dimensional electron gas: quasiclassical transport beyond the Boltzmann equation. *Phys. Rev. B*, **70**:165305, 2004.

[76] A.L. Zakharov. —. *Sov. Phys. JETP*, **11**:478, 1960.

[77] F.S. Bergeret, B. Huckestein, and A.F. Volkov. Current-voltage characteristics and the zero-resistance state in a two-dimensional electron gas. *Phys. Rev. B*, **67**:241303, 2003.

[78] V. Ryzhii and A. Satou. Electric-field breakdown of absolute negative conductivity and supersonic streams in two-dimensional elelctron systems with zero resistance/conductance states. *J. Phys. Soc. Jpn.*, **72**:2718, 2003.

[79] A.F. Volkov and V.V. Pavlovskii. Residual resistance in a two-dimensional electron system: A phenomenological approach. *Phys. Rev. B*, **69**:125305, 2004.

[80] R.G. Mani. Novel zero-resistance states induced by photoexcitation in the high mobility GaAs/AlGaAs two-dimensional electron system. *Physica E*, **25**:189, 2004.

[81] S.I. Dorozhkin, J.H. Smet, V. Umansky, and K. von Klitzing. Microwave photoresponse in the two-dimensional electron system caused by intra-Landau-level transitions. *Phys. Rev. B*, **71**:201306, 2005.

[82] A.E. Kovalev, S.A. Zvyagin, C.R. Bowers, J.L. Reno, and J.A. Simmons. Observation of a node in the quantum oscillations induced by microwave radiation. *Solid State Commun.*, **130**:379, 2004.

[83] K. Barnham and D. Vvedensky. *Low-dimensional semiconductor structures*. Cambridge University Press, United Kingdom, 2001.

[84] U.K. Mishra and J. Singh. *Semiconductor device physics and design*. Springer, Netherlands, 2008.

[85] S.M. Sze. *Physics of semiconductor devices*. A Wiley-Interscience publication, New York, 2nd edition, 1981.

[86] A. Piotrowska, A. Guivarch, and G. Pelous. Ohmic contacts to III-V compound semiconductors: a review of fabrication techniques. *Solid-State Electron.*, **26**:179, 1983.

[87] M. Ogawa. Alloying behavior of Ni/Au-Ge films on GaAs. *J. Appl. Phys.*, **51**:406, 1980.

[88] M.N. Yoder. Ohmic contacts in GaAs. *Solid-State Electron.*, **23**:117, 1980.

[89] K.C. Lee. Bonding wires to quantized Hall resistors. *IEEE Trans. Instrum. Meas.*, **44**:249, 1995.

[90] W. Zhang. *Nonlinear magnetotransport in Gallium Arsenide and Aluminum Gallium Arsenide based two dimensional electron systems*. University of Minnesota, 2008.

[91] M. Mola, S. Hill, P. Goy, and M. Gross. Instrumentation for millimeter-wave magnetoelectrodynamic investigations of low-dimensional conductors and superconductors. *Rev. Sci. Instrum.*, **71**:186, 2000.

[92] D.M. Pozar. *Microwave engineering*. John Wiley & Sons, Inc., United States of America, 3rd edition, 2005.

[93] W.M. Haynes and D.R. Lide. *CRC handbook of chemistry and physics*. CRC Press., United States of America, 90th edition, 2009–2010.

[94] J.D. Jackson. *Classical electrodynamics*. Wiley, New York, 3rd edition, 1998.

[95] H.H. Sample and L.G. Rubin. Instrumentation and methods for low temperature measurements in high magnetic fields. *Cryogenics*, **17**:597, 1977.

[96] *Temperature measurement and control catalog*. Lake Shore Cryotronics, Inc., United States, 2004.

[97] C.L. Yang, J. Zhang, R.R. Du, J.A. Simmons, and J.L. Reno. Zener tunneling between Landau orbits in a high-mobility two-dimensional electron gas. *Phys. Rev. Lett.*, **89**:076801, 2002.

[98] X.L. Lei. Current-induced magnetoresistance oscillations in two-dimensional electron systems. *Appl. Phys. Lett.*, **90**:132119, 2007.

[99] A.A. Bykov, J. Zhang, S. Vitkalov, A.K. Kalagin, and A.K. Bakarov. Effect of dc and ac excitations on the longitudinal resistance of a two-dimensional electron gas in highly doped GaAs quantum wells. *Phys. Rev. B*, **72**:245307, 2005.

[100] J. Zhang, S. Vitkalov, A.A. Bykov, A.K. Kalagin, and A.K. Bakarov. Effect of a dc electric field on the longitudinal resistance of two-dimensional electrons in a magnetic field. *Phys. Rev. B*, **75**:81305, 2007.

[101] W. Zhang, H.-S. Chiang, M.A. Zudov, L.N. Pfeiffer, and K.W. West. Magneto-transport in a two-dimensional electron system in dc electric fields. *Phys. Rev. B*, **75**:41304, 2007.

[102] M.G. Vavilov, I.L. Aleiner, and L.I. Glazman. Nonlinear resistivity of a two-dimensional electron gas in a magnetic field. *Phys. Rev. B*, **76**:115331, 2007.

[103] A.T. Hatke, M.A. Zudov, L.N. Pfeiffer, and K.W. West. Role of electron-electron interactions in nonlinear transport in two-dimensional electron systems. *Phys. Rev. B*, **79**:161308, 2009.

[104] A.A. Bykov, J. Zhang, S. Vitkalov, A.K. Kalagin, and A.K. Bakarov. Zero-differential resistance state of two-dimensional electron systems in strong magnetic fields. *Phys. Rev. Lett.*, **99**:116801, 2007.

[105] N.R. Kalmanovitz, A.A. Bykov, S. Vitkalov, and A.I. Toropov. Warming in systems with a discrete spectrum: Spectral difussion of two-dimensional electrons in a magnetic field. *Phys. Rev. B*, **78**:085306, 2008.

[106] W. Zhang, M.A. Zudov, L.N. Pfeiffer, and K.W. West. Resistance oscillations in two-dimensional electron systems induced by both ac and dc fields. *Phys. Rev. Lett.*, **98**:106804, 2007.

[107] W. Zhang, M.A. Zudov, L.N. Pfeiffer, and K.W. West. Resonant phonon scattering in quantum Hall systems driven by dc electric fields. *Phys. Rev. Lett.*, **100**:036805, 2008.

[108] A.T. Hatke, H.-S. Chiang, M.A. Zudov, L.N. Pfeiffer, and K.W. West. Zero differential resistance in two-dimensional electron systems at large filling factors. *Phys. Rev. B*, **82**:041304, 2010.

[109] A. Dmitriev, M. Dyakonov, and R. Jullien. Classical mechanism for negative magnetoresistance in two dimensions. *Phys. Rev. B*, **64**:233321, 2001.

[110] A. Auerbach, I. Finkler, B.I. Halperin, and A. Yacoby. Steady states of a microwave-irradiated quantum-Hall gas. *Phys. Rev. Lett.*, **94**:196801, 2005.

[111] I.G. Finkler and B.I. Halperin. Microwave-induced zero-resistance states are not necessarily static. *Phys. Rev. B*, **79**:085315, 2009.

[112] A.T. Hatke, H.-S. Chiang, M.A. Zudov, L.N. Pfeiffer, and K.W. West. Nonlinear magnetotransport in microwave-illuminated two-dimensional electron systems. *Phys. Rev. B*, **77**:201304, 2008.

[113] M.A. Zudov, R.R. Du, L.N. Pfeiffer, and K.W. West. Multiphoton processes in microwave photoresistance of two-dimensional electron systems. *Phys. Rev. B*, **75**:41303, 2006.

[114] S.I. Dorozhkin, J.H. Smet, K. v. Klitzing, L.N. Pfeiffer, and K.W. West. Microwave induced magnetoresistance oscillations at the subharmonics of the cyclotron resonance. *JETP Lett.*, **89**:543, 2007.

[115] X.L. Lei and S.Y. Liu. Magnetoresistance oscillations in two-dimensional electron systems under monochromatic and bichromatic radiations. *Appl. Phys. Lett.*, **89**:182117, 2006.

[116] I.A. Dmitriev, A.D. Mirlin, and D.G. Polyakov. Theory of fractional microwave-induced resistance oscillations. *Phys. Rev. Lett.*, **99**:206805, 2007.

[117] I.V. Pechenezhskii, S.I. Dorozhkin, and I.A. Dmitriev. Fractional features in radiation-induced oscillations of the magnetoresistance of two-dimensional electron systems. *JETP Lett.*, **85**:86, 2007.

[118] A.T. Hatke, H.-S. Chiang, M.A. Zudov, L.N. Pfeiffer, and K.W. West. Microwave photoresistance in dc-driven 2d systems at cyclotron resonance subharmonics. *Phys. Rev. Lett.*, **101**:246811, 2008.

[119] X.L. Lei. Nonlinear theory of fractional microwave-induced magnetoresistance oscillations in a dc-driven two-dimensional electron system. *Phys. Rev. B*, **79**:115308, 2009.

[120] M. Khodas, H.-S. Chiang, A.T. Hatke, M.A. Zudov, M.G. Vavilov, L.N. Pfeiffer, and K.W. West. Nonlinear magnetoresistance oscillations in intensely irradiated two-dimensional electron systems induced by multiphoton processes. *Phys. Rev. Lett.*, **104**:206801, 2010.